

**Magnetic Resonance Imaging
in
Radiotherapy Treatment Planning**

CIP-GEGEVENS KONINKLIJKE BIBLIOTHEEK, DEN HAAG

Moerland, Marinus A.

Magnetic Resonance Imaging in Radiotherapy
Treatment Planning / Marinus A. Moerland. -
Utrecht: Universiteit Utrecht, Faculteit Geneeskunde
Proefschrift Universiteit Utrecht. - Met lit. opg. -
Met samenvatting in het Nederlands.
ISBN 90-393-1446-2

Druk: Addix, Wijk bij Duurstede

Omslag: R. van Suijdam

Parts of chapter 4 were printed by Pergamon Press (New York) and The British Institute of Radiology (London), parts of chapter 6 were printed by The Institute of Physics Publishing Ltd. (Bristol), and parts of chapter 7 were printed by Elsevier Science Ireland Ltd. (Shannon).

Magnetic Resonance Imaging in Radiotherapy Treatment Planning

Het gebruik van MRI
bij de radiotherapieplanning
(met een samenvatting in het Nederlands)

Proefschrift
ter verkrijging van de graad van doctor
aan de Universiteit Utrecht
op gezag van de Rector Magnificus, Prof. dr J.A. van Ginkel
ingevolge het besluit van het College van Dekanen
in het openbaar te verdedigen
op dinsdag 5 november 1996 des middags te 2.30 uur

door
Marinus Adriaan Moerland
geboren op 17 juli 1957, te Stavenisse

promotor: Prof. dr J.J. Battermann
co-promotoren: Dr C.J.G. Bakker
Dr ir J.J.W. Lagendijk

Het in dit proefschrift beschreven onderzoek werd uitgevoerd op de afdeling Radiotherapie van het Academisch Ziekenhuis Utrecht in nauwe samenwerking met de afdeling Radiodiagnostiek en werd mogelijk gemaakt met de financiële steun van de Nederlandse Kankerbestrijding (Koningin Wilhelmina Fonds).

*aan mijn ouders
voor Rianne, Maaike, Joline en Merijn*

Typesetting: The text of this thesis was produced in L^AT_EX. Illustrations were drawn in **xfig** and **xmgr** and were included as PostScript files. Medical images and calculated images were also converted to PostScript files. The L^AT_EX file with all the images has been compiled on a *Silicon Graphics* workstation. The output was rendered at 2400 dpi on film.

Contents

List of abbreviations and symbols	11
1 General introduction	15
1.1 Introduction	16
1.2 MR image distortions	17
1.3 Integration of MRI into RTP	18
1.4 MRI organ motion studies for RTP	19
1.5 MRI-based brachytherapy evaluation	20
1.6 Outline of the thesis	21
2 Magnetic resonance imaging	23
2.1 Nuclear magnetic resonance (NMR)	24
2.2 Spatial encoding in magnetic resonance imaging (MRI)	24
2.3 The \mathbf{k} -space	26
2.4 Sources of image distortions in MRI	27
2.4.1 Machine-related magnetic field errors	27
2.4.2 Object-related magnetic field inhomogeneity	28
2.5 Two-dimensional Fourier transform (2DFT) imaging	30
2.5.1 Slice selection in the presence of magnetic field inhomogeneity and gradient non-linearity	32
2.5.2 In-plane image distortions in spin echo (SE) imaging	32
2.5.3 In-plane image distortions in gradient echo (GE) imaging	33
2.5.4 In-plane image distortions in echo planar imaging (EPI)	34
3 Measurement and correction of geometric distortions in MRI caused by machine imperfections	39
3.1 Introduction	40
3.2 Theoretical	40
3.3 Methods and materials	41
3.3.1 Phantoms	41
3.3.2 Measurement and correction	42
3.3.3 Software tools	45
3.4 Results	45
3.4.1 Field error measurements	45
3.4.2 Distortion correction	46
3.5 Discussion	50
3.6 Conclusions	52

4	Analysis of geometric distortions in MRI caused by patient related magnetic field inhomogeneity	53
4.1	Introduction	54
4.2	Measurements of object-related image distortions around the head and in the localization frame	54
4.2.1	Materials	54
4.2.2	Imaging experiments	55
4.2.3	Image processing	56
4.2.4	Results	56
4.3	Numerical analysis of the magnetic field for arbitrary susceptibility distributions: application to the head	59
4.3.1	Theory	59
4.3.2	Numerical solution	59
4.3.3	Implementation	60
4.3.4	Materials	60
4.3.5	Results	61
4.4	Discussion	64
4.5	Conclusions	66
5	MR pulse sequence parameters affecting the severity of geometry and intensity distortions	69
5.1	Introduction	70
5.2	Methods and materials	70
5.3	Results and discussion	71
5.4	Conclusions	77
6	Investigation of geometric distortions in 1.5 T magnetic resonance images for use in radiotherapy treatment planning of patients with brain tumours	79
6.1	Introduction	80
6.2	Methods and materials	82
6.2.1	Experiments	82
6.2.2	Analysis	83
6.2.3	Correction	85
6.3	Results and discussion	85
6.3.1	Experiments	85
6.3.2	Analysis	85
6.3.3	Correction method	88
6.4	Conclusions	90
7	The influence of respiration induced motion of the kidneys on the accuracy of radiotherapy treatment planning, a magnetic resonance imaging study	91
7.1	Introduction	92
7.2	Methods and materials	92
7.3	Results	94
7.4	Discussion	96

8 Evaluation of permanent I-125 prostate implants using radiography and magnetic resonance imaging	99
8.1 Introduction	100
8.2 Methods and materials	101
8.2.1 Pre-implant dose calculation	101
8.2.2 Reconstruction of the seed distribution in relation to the prostate . .	101
8.2.3 Implant evaluation by dose volume histogram computation	103
8.2.4 The validity of the ellipsoidal target volume approximation	104
8.2.5 Estimation of post-implant prostate swelling	104
8.3 Results and discussion	104
8.3.1 Implant evaluation	104
8.3.2 The validity of the ellipsoidal target volume approximation	105
8.3.3 Post-implant prostate swelling	105
8.3.4 Accuracy of seed placement	105
8.3.5 Reflections on adjustment of implantation technique and dose prescrip- tion	106
8.4 Conclusions	108
Summary and Conclusion	111
Samenvatting en conclusie	117
References	123
List of publications	133
Dankwoord	137
Curriculum Vitae	139

List of abbreviations and symbols

Abbreviations

AAPM	American Association of Physicists in Medicine
AP	antero-posterior
CT	Computer Tomography
DRE	Digital Rectal Examination
EPI	Echo Planar Imaging
FFE	Fast Field Echo
FOV	Field of view
GE	Gradient Echo
GRASE	Gradient and Spin Echo
ICRU	International Commission on Radiation Units and Measurements
IKMN	Integraal Kankercentrum Midden Nederland
IR	Inversion Recovery
IVU	Intra Venous Urography
I-125	Iodine
MPD	Matched Peripheral Dose
MR	Magnetic Resonance
MRI	Magnetic Resonance Imaging
MRS	Magnetic Resonance Spectroscopy
MSE	Modified Spin Echo
MSP	Magnetic Scalar Potential
MTC	Magnetization Transfer Contrast
NEX	Number of excitations (signal averages)
NKB	Nederlandse Kanker Bestrijding
NMR	Nuclear Magnetic Resonance
NSA	Number of Signal Averages
NTCP	Normal Tissue Complication Probability
PA	postero-anterior
ppm	parts per million
REST	Regional Saturation Technique
RF	Radio Frequency
RTP	Radiotherapy Treatment Planning
SE	Spin Echo
SPIR	Spectral Presaturation with Inversion Recovery
TFE	Turbo Field Echo
TRUS	Transrectal ultrasound
TSE	Turbo Spin Echo
VOI	Volume Of Interest
wfs	water fat shift
2D, 3D	Two, Three dimensional

Symbols

a, b, c	Orthogonal dimensions of volume [m]
$A(x, y, z)$	Distribution of the transverse magnetization
$A'(u, v)$	Inverse 2D Fourier transform of the acquisition matrix $S(n, m)$
\mathbf{B}	Induced magnetic field [T]
\mathbf{B}_{G_x}	Magnetic field due to x -gradient [T]
$\Delta\mathbf{B}_{G_x}, \Delta\mathbf{B}_{G_y}, \Delta\mathbf{B}_{G_z}$	Magnetic field error due to x, y, z -gradient non-linearity [T]
\mathbf{B}_0	Static magnetic field [T]
$\Delta\mathbf{B}_0$	Static magnetic field error [T]
\mathbf{B}_i	Internal magnetic field [T]
$B(i)$	Dimensionless coefficient with index i
$D(i)$	Dimensionless coefficient with index i
D	Diameter of a cylinder [m]
f_0	Resonance frequency [Hz]
Δf_0	Offset in resonance frequency [Hz]
G_x	Magnetic field gradient in the x -direction (read-out) [T/m]
G_{xc}	Amplitude of the read-out compensation gradient [T/m]
G_y	Magnetic field gradient in the y -direction (phase-encoding) [T/m]
ΔG_y	Step-size of the phase-encoding gradient [T/m]
G_z	Magnetic field gradient in the z -direction (slice selection) [T/m]
\mathbf{H}	Magnetic field [A/m]
\mathbf{k} -space	Spatial frequency domain
k_x, k_y, k_z	Components of k -space [rad/m]
l	Distance [m]
m	m -th phase-encoding step
\mathbf{M}	Magnetization [A/m]
\mathbf{M}_0	Equilibrium magnetization [A/m]
n	n -th time sample of the MR signal
N_p	Number of phase encoding steps
N_s	Number of time samples
$S(n, m)$	Acquisition matrix
t	Time [s]
Δt	Time sampling interval [s]
TE	Echo time [s]
TR	Repetition time [s]
T_1	Longitudinal magnetic relaxation time (spin-lattice) [s]
T_2	Transversal magnetic relaxation time (spin-spin) [s]
T_2^* -effect	Effect causing intra-voxel phase dispersion [s]

T_{xc}, T_{yc}	Duration of the read-out, phase-encoding gradient [s]
T_x, T_y	Duration of the read-out, phase-encoding gradient [s]
ΔT_y	Echo spacing in echo planar imaging [s]
V	Volume [m ³]
x, y, z	Position coordinates [m]
x_1, y_1, z_1	Distorted position coordinates [m]
α	Excitation angle [rad]
γ	Proton gyromagnetic ratio: $2\pi \cdot 42.57602 \cdot 10^6$ [rad/(T · s)]
μ	Magnetic permeability
μ_0	Magnetic permeability in vacuum $4\pi \cdot 10^{-7}$ [H/m]
τ	Iteration coordinate
Φ	Spatially dependent phase evolution [rad]
Φ^*	Disturbed spatially dependent phase evolution [rad]
Φ_M	Magnetic Scalar Potential [Wb/m]
χ	Magnetic susceptibility
ω	Frequency [rad/s]
$\Delta\omega$	Bandwidth [rad/s]

Chapter 1

General introduction

1.1 Introduction

From its inception in the early 1970's up to the present, magnetic resonance imaging (MRI) has evolved into a sophisticated technique, which has aroused considerable interest in various subfields of medicine, including radiotherapy. MRI is capable of imaging in any plane and does not use ionizing radiation by virtue of which MRI lends itself admirably to the purpose of prolonged time course studies. MRI is capable of excellent spatial resolution and it presents information over large areas of the body. The MRI signal depends on multiple parameters resulting in excellent contrast resolution of the soft tissues. By choosing the appropriate experimental conditions, image contrast can be made to reflect any number of the following physical parameters: proton density, the relaxation times T_1 and T_2 , chemical shift, flow, magnetic susceptibility, diffusion and perfusion, that vary as a function of tissue anatomy, physiology and biochemistry. Within the realm of radiotherapy, MRI offers prospects with regards to identification of tissues and tissue abnormalities (tumour, oedema, necrosis, fibrosis, cysts), determination of tumour extent in relation to surrounding tissues and organs, and assessment of response to treatment.

The goal of radiotherapy is to administer a high dose to the tumour while sparing healthy surrounding tissues as much as possible. Since tight margins around the target are applied, accurate information on tumour extent is of great value in radiotherapy treatment planning (RTP). Also information on motion of the tumour and surrounding organs, e.g. caused by respiration, is of importance for defining the margins and can be acquired by fast MR imaging techniques. However, the introduction of MRI into RTP is seriously hampered by geometry and intensity distortions, which are known to be present in MRI. These distortions are caused by non-idealities of the equipment (non-uniformity of the static magnetic field and non-linearities of the gradient magnetic fields of the MRI scanner) and by magnetic field perturbations induced by the object to be imaged, in this case the human body. These magnetic field inhomogeneities and gradient field non-linearities lead to image distortions, the severity of which depends on the type of pulse sequence and its parameters.

To investigate the capabilities of MRI in radiotherapy treatment planning and to explore systematically the nature and severity of the image distortions and how they can be reduced or, if necessary, corrected in order to integrate MRI into RTP in a reliable manner, the project **MRI in radiotherapy planning** (*IKMN 90-04*) was started at the Department of Radiotherapy. This project was supported by the *The Dutch Cancer Society (Nederlandse Kanker Bestrijding, NKB)* and carried out in close cooperation with the Department of Radiology. The problems associated with the integration of MRI into RTP were approached in two ways. Firstly, a computer model was developed for calculating image distortions induced by the object. Theoretical analysis and simulations led to insight in the nature and severity of the object-related MR image distortions, which has been reported in the literature (Bakker et al. 1993; Bhagwandien et al. 1992a; Bhagwandien et al. 1994) and in a Ph.D. thesis (Bhagwandien 1994). Secondly, the problems were approached experimentally. Image distortions and the efficacy of correction methods were evaluated in phantom, volunteer, and patient studies. Furthermore, the potential of MRI in organ motion studies was investigated and it was explored whether the image artifacts induced by I-125 seeds could be used to evaluate permanent prostate implants in brachytherapy. This thesis presents the experimental work done within the project **MRI in radiotherapy planning**.

1.2 MR image distortions

In the literature dealing with MR image distortions, there is a consensus that machine dependent MR image distortions are significant in applications which require mm accuracy (Galvin et al. 1984; Henkelman et al. 1984; Bakker et al. 1992). Several measurement and correction methods were applied. In a clinical environment, phantom based methods were most appropriate since they need no pulse sequence modifications (Bakker et al. 1992; Cho et al. 1988; Kawanaka and Takagi 1986; Maudsley et al. 1984; O'Donnell and Edelstein 1985; Sekihara et al. 1984; Willcott III et al. 1987). Our institute participated in the EEC Concerted Action on Tissue Characterization by magnetic resonance spectroscopy (MRS) and MRI which i.a. resulted in the development of phantoms for measurement of geometric distortions and slice warp (Podo and Orr 1992). In a multi-centre trial, machine dependent geometric distortions up to 5 mm and on one scanner up to 13 mm were observed (Lerski et al. 1988). The phantoms, used in the EEC Concerted Action studies, were Perspex disc-shaped phantoms, containing doped water and a grid of Perspex rods. Bhagwandien et al. 1994 showed, by numerical calculation of the magnetic field, that cylindrical phantoms with small length/diameter ratios result in perturbation of the magnetic field, and thus disc-shaped phantoms are less suited to measure static and gradient field errors. We developed a grid phantom, which contains tubes with a large length/diameter ratio, and related analysis software for the measurement of inhomogeneity of the static field \mathbf{B}_0 and non-linearity of the gradients G_x , G_y and G_z on our 0.5 and 1.5 tesla MRI scanners. Once the machine dependent errors are quantified, the MR images can be corrected by inverse pixel transformations (Bakker et al. 1992; Michiels et al. 1994; Schad et al. 1987a). The applicability of correction schemes in clinical practice depends on the field error stability in time and on the influence of pulse sequence parameters on the machine dependent image distortions, e.g. the pattern of distortions could change with gradient strengths and directions, single/multiple slice acquisitions, type of pulse sequence (spin echo, gradient echo, echo planar imaging). Schad et al. 1987a attributed image distortions to the occurrence of eddy currents, the influence of which theoretically depends on the amplitude of the gradients and the frequency of switching the gradients.

The problem of object related image distortions was addressed by Lüdeke et al. 1985. They demonstrated magnetic field distortions in and around cylindrical and spherical objects. In our group, a numerical method was developed for calculation of the magnetic field for arbitrary susceptibility distributions (Bhagwandien et al. 1992a; Bhagwandien et al. 1994). As already mentioned above, this method was used for analysis of distortions in images of cylindrical phantoms, but also for analysis of image distortions caused by magnetic field perturbations by the patient itself (Bhagwandien et al. 1992b; Bhagwandien 1994). Chang and Fitzpatrick 1992 presented a method to correct for the patient related distortions. The technique required the acquisition of two images with altered gradients, from which the correct image could be calculated. The efficacy of the technique was proven for phantom experiments. We adopted this method for the correction of patient images. Gross correction of contours seemed feasible, but anatomical detail was not preserved (Bakker et al. 1992). Sumanaweera et al. 1993 and Sumanaweera et al. 1994 presented a method for the correction of patient related distortions, which required measurement of the magnetic field map for each patient. Cho et al. 1988 and Cho and Ro 1992 proposed inhomogeneity correction methods including chemical shift and susceptibility artifacts. These methods required modifications of the pulse sequences and were therefore not readily available in a clinical environment. We studied distortions of external markers by computer simulation

(Bhagwandien et al. 1992b; Bhagwandien 1994), in volunteer studies and in clinical studies on brain tumours (Bakker et al. 1992; Moerland et al. 1995). Volunteers and patients were imaged in radiotherapy position with the head fixed by a cast in a home built localization frame. Systematic variation of the read-out gradient direction revealed susceptibility induced shifts in the direction of the read-out gradient. External markers attached to the head cast or embedded in the localization frame showed significant susceptibility induced distortions. Magnetic field perturbations decreased with increase of distance from the head, but also markers at a few cm's distance from the head in the localization frame showed significant shifts, which was explained by the fact that also the Perspex frame perturbs the magnetic field. Our analysis showed that the accuracy of an external landmark depends heavily on its position. In continuation of our analysis studies we implemented a new method for correction of susceptibility induced image distortions (Bhagwandien 1994). Compared to the method proposed by Chang and Fitzpatrick 1992, which is based on a set of two distorted MR images, our method has the advantage that besides the distorted image no extra image is required. The main steps in this method are the conversion of the MR image into a magnetic susceptibility distribution by segmenting the image into air and water equivalent tissue, the calculation of the magnetic field and the calculation of the corrected MR image by applying a reversed read-out gradient. With this method marker shifts were reduced and distorted internal and external structures were rectified. A disadvantage of the method is that field calculation and image calculation are at present very time consuming. An other approach to deal with susceptibility induced image distortions is based on the observation that image distortions caused by field inhomogeneity are proportional to the static magnetic field strength and inversely proportional to gradient strength, so that these distortions can be reduced by optimization of the pulse sequence parameters.

1.3 Integration of MRI into RTP

The lack of confidence in the spatial accuracy of MRI and the limited time available for imaging of patients for radiotherapy treatment planning have prohibited its wide-spread introduction into RTP, but the excellent tumour imaging capability of MRI has incidentally tempted people to use MRI in (mostly CT-assisted) radiotherapy treatment planning (Heesters et al. 1993; Just et al. 1991; Mayr et al. 1993; Pötter et al. 1992; Schad et al. 1992; Schad et al. 1994; Shuman et al. 1985; TenHaken et al. 1992; Toonkel et al. 1988; Yanke et al. 1991). The definition of irradiation fields based on CT and MR images required a reference coordinate system, usually realized with markers attached to the patients skin or in a localization frame. These markers were mostly radiopaque tubes or catheters for CT scanning and tubes filled with e.g. a copper sulfate solution for MR scanning. The use of markers is conceptually straightforward and does not require complex image correlation techniques, provided that both data sets are geometrically accurate and acquired with the patient in a fixed radiotherapy position. As mentioned above, MR image distortions stem from machine imperfections and magnetic properties of the object itself (susceptibility artifact). Several authors have proposed correction methods for object related image distortions, but in our view the optimization of pulse sequence parameters to reduce object related distortions seems most feasible for clinical practice. Good quality MR images with minimal susceptibility induced distortions were obtained on a 0.5 T MRI scanner using 3 mT/m gradients (Michiels et al. 1994). The remaining distortions to be corrected were the machine dependent distortions caused by non-linearity of the gradients. Especially

when using a localization frame, machine dependent distortions of markers are relatively large, since the markers are located towards the edges of the magnet bore, where magnetic field homogeneity is worst. Also in MR body imaging, for which larger fields of view are necessary, the distortions will be larger compared to distortions in head imaging. Fraass et al. 1987 concluded that a full 3D unwarping algorithm was mandatory to achieve geometrical consistency and also Schad et al. 1987a reduced in-plane distortions (from 5 mm to 1-2 mm) and corrected tilt of the image planes by adjustment of the gradient shimming currents. Apart from marker based image registration (Van den Elsen and Viergever 1994; Sumanaweera et al. 1994), a variety of techniques is available to register image sets from different modalities based on features of the objects to be imaged (Van den Elsen et al. 1993; Maurer and Fitzpatrick 1993). Object features which have been used successfully for registration include internal landmarks (Hill et al. 1991; Evans et al. 1989; Boesecke et al. 1990), surfaces (Pelizzari et al. 1989; Jiang et al. 1992; Collignon et al. 1994), and geometric features (Van den Elsen et al. 1992; Van Herk and Kooy 1994). Kooy et al. 1994 and Van Herk and Kooy 1994 used chamfer matching of internal anatomy in the MR and CT images and achieved proper alignment of the skull and internal structures, whereas the external fiducial markers proved to be grossly misaligned. In our Department of Image Sciences, several image registration techniques were developed, including techniques based on internal image features (Van den Elsen 1993). Hemler et al. 1995 compared different multi-modality registration techniques and determined the sensitivity of each registration method to distortion in magnetic resonance head images. They found that MR distortion correction significantly improved frame-based registration, but the correlation and surface-based registration of high resolution (1 mm) CT and MR data sets were insensitive to MR distortions. Maurer et al. 1994 found that correction of geometrical distortion in MR head images significantly reduced the registration error of both point-based and surface-based registration. The above mentioned studies of marker based and object feature based image registration led to the conclusion that corrections for machine dependent image distortions and guidelines to minimize susceptibility-induced distortions are necessary for integration of MRI into RTP to be reliable, especially when applying larger fields of view as in head imaging in a localization frame or as in body imaging.

1.4 MRI organ motion studies for RTP

The goal of radiotherapy is to supply a specified dose to the target volume while minimizing the dose to normal tissues. Imaging techniques like 3D-CT and 3D-MRI are being evaluated as to their potential for radiotherapy treatment planning (Fraass et al. 1987; Glatstein et al. 1985; Schad et al. 1987b; TenHaken et al. 1992; Heesters et al. 1993). The application of these imaging techniques allows optimization of treatment plans to cover the target volumes as close as possible, often called conformation therapy (Vijayakumar and Chen 1995). Patient movement is a major challenge to conformation therapy, e.g. motion due to respiration. The consequence of respiration is that the treatment volume has to be increased, unless target motion is effectively eliminated by respiration gated radiotherapy (Kubo and Hill 1996; Ohara et al. 1989). In view of the tendency to employ conformation therapy based on treatment planning techniques using static CT and/or MRI, instead of dynamic fluoroscopy, knowledge about organ motion is becoming more and more important. There has been a surge of respiration gated studies among MRI users, since image quality may be degraded by the respiration motion (Ehman et al. 1984; Runge et al. 1984; Korin et al. 1992; Ritchie

et al. 1994). Respiration motion studies for RTP are scarce. Willett et al. 1987 studied the effect of the respiratory cycle on mediastinal and lung dimensions in Hodgkin's disease using chest radiography and CT scans both during quiet breathing and at maximum inspiration. The volumes of mediastinum, irradiated and protected lung, if antero-posterior (AP) and postero-anterior (PA) mantle fields were used, were determined from CT scans and three-dimensional treatment planning and compared at quiet breathing and deep inspiration. On average, 8% more lung was protected at deep inspiration than at quiet breathing, which suggests that radiotherapy gated to respiration may be advantageous. TenHaken et al. 1994 studied the effects of patient breathing on CT-based 3D planning for lung irradiation using a spiral CT scanner. They concluded that static CT significantly misrepresented the shape and the volume of critical structures, which made calculation of normal tissue complication probabilities (NTCP) unreliable (tens of % change in NTCP for lung at an irradiation dose of 70 Gy). Van Tienhoven et al. 1991 studied the accuracy in tangential breast treatment setup using portal imaging and found that respiration did not have a significant influence on treatment volume. Ross et al. 1990 analysed the movement of intrathoracic neoplasms using ultrafast computerized tomography. They detected geographic misses in 3 out of 20 patients when treatment portals were setup with conventional simulation techniques. These studies illustrate the implications of respiration for radiotherapy. Fast MRI scan techniques, sometimes called MR fluoroscopy or real-time MRI (Riederer et al. 1988; Holsinger et al. 1990), may be employed to study the respiration motion of the target volume in an individual patient, but also to expand the general insight in respiration induced organ motion by searching for correlations between organ motion and e.g. sex, age, body length, body weight or pathology.

1.5 MRI-based brachytherapy evaluation

As in external beam therapy, modern imaging techniques like CT and MRI are being evaluated on their potential for brachytherapy planning and evaluation, in particular for interstitial brain implants. Most techniques use CT in conjunction with a stereotaxic frame for accurate placement of catheters or radioactive seeds (e.g. Lulu et al. 1990; Weaver et al. 1990; Warszawski et al. 1992; Schupak et al. 1995). At our department, in collaboration with the Daniel den Hoed Kliniek, Rotterdam and the Academisch Medisch Centrum, Amsterdam, a new MRI based treatment planning system for the treatment of brain tumours with interstitial hyperthermia is being developed (Kotte et al. 1996a; De Bree et al. 1996; Lagendijk et al. 1995; Van der Koijk et al. 1996). This system uses vascular information to optimize implants. An MRI compatible template technique is being developed to guide the insertion of the catheters (Kotte et al. 1996b). Aydin et al. 1993 presented a method of MRI-guided brachytherapy for cancer of the oesophagus. Performing MRI in sagittal, coronal, and transversal planes with the catheter in situ allowed precise brachytherapy planning, since MRI showed the extent of the tumour in relation to the catheter, after which the tumour could be covered with the necessary dose. The ability of MRI to differentiate between different soft tissues was also helpful in brachytherapy planning and evaluation of cervix patients. Schea et al. 1990 and Schoeppel et al. 1990 performed MRI scans to patients being treated for cervix cancer with a plastic MR compatible applicator in situ. MRI-based brachytherapy planning showed the relationship of the dose to the anatomy, where the cervix lighted up on the T_2 -weighted MR images, and could be differentiated from normal tissue, bladder and rectum. The dosimetric study by Schoeppel et al. 1990 showed poor correlation

between minimum irradiation dose to the cervix and the dose prescribed to point A, which is 2 cm cranial from the portio and 2 cm lateral from the intra-uterine applicator. Maximum doses in the critical organs bladder and rectum estimated from conventional orthogonal simulator films also did not correlate with CT-calculated doses. Roy et al. 1993 presented a CT-based evaluation method for permanent prostate implants and reported that the minimum dose to the prostate proved to be 2 to 3 times smaller than the prescribed dose. The above mentioned studies indicate that the potential of MRI for brachytherapy has not been fully explored yet and that integration of MRI into brachytherapy planning and evaluation may improve the quality of brachytherapy.

1.6 Outline of the thesis

The aim of this thesis is to investigate the capabilities of MRI in radiotherapy treatment planning and to explore the MR image distortions and how distortions can be reduced or, if necessary, corrected in order to integrate MRI into RTP in a reliable manner.

In chapter 1, we introduced the potentials and problems with regard to the use of MRI for radiotherapy treatment planning and presented a review of the pertinent literature.

Chapter 2 briefly reviews the basic principles of nuclear magnetic resonance (NMR), spatial encoding in MRI, and the sources of geometry and intensity distortions in MRI.

Chapter 3 describes the measurement, analysis, and correction of machine dependent geometric distortions in MRI with special attention for phantom design and field error stability in time, and for different pulse sequence parameters.

Chapter 4 describes the analysis of the patient related magnetic field perturbations and resulting image distortions in case of MRI of the head and the pelvic region.

Chapter 5 describes qualitatively the influence of the type of pulse sequence and its parameters on geometry and intensity distortions.

Chapter 6 describes the investigation of geometric distortions in 1.5 T MR images for use in radiotherapy treatment planning of patients with brain tumours.

Chapter 7 illustrates the use of fast MRI scan techniques for organ motion studies, in this case respiration induced kidney motion and its influence on the dose delivered to the kidney, if shielded by a block during irradiation of the abdomen.

Chapter 8 describes a technique, which utilizes the MR intensity distortions due to object induced magnetic field inhomogeneity. The MR signal loss caused by I-125 seeds was used to develop a method for MRI-based evaluation of permanent prostate implants.

Chapter 2

Magnetic resonance imaging

2.1 Nuclear magnetic resonance (NMR)

This review aims to present very briefly the basic principles of nuclear magnetic resonance (NMR) according to the classical model, which is a more simple and pictorial model compared to the quantum mechanical model (Abragam 1961; Farrar and Becker 1971; Elster 1994). Some nuclei, e.g. hydrogen, have a net magnetic dipole moment making their magnetic properties similar to those of tiny bar magnets. They produce a magnetic field themselves, and they experience a torque or couple when placed in a magnetic field, analogous to a spinning top in the earth's gravitational field. As a result, they precess around the axis of the magnetic field at a rate given by the Larmor relationship:

$$\omega = \gamma \mathbf{B}_0 \quad (2.1)$$

where ω is the precessional or Larmor frequency [rad s^{-1}], γ is the gyromagnetic ratio and \mathbf{B}_0 is the static magnetic field [T]. γ is a nuclear constant, characteristic of every isotope ($\gamma_{\text{H-1}} = 2\pi \cdot 42.57602 \cdot 10^6 \text{ rad}/(\text{T s})$). The nucleus that lends itself best to magnetic resonance imaging is the proton, because of its large abundance in the human body and its favourable magnetic moment. Without an externally applied magnetic field, the magnetic dipoles are randomly orientated, and the net magnetization of a sample of tissue is zero. However, when placed in a strong externally applied magnetic field, a given volume of tissue possesses a net equilibrium magnetization \mathbf{M}_0 , which points in the direction of the externally applied magnetic field. This direction is called the longitudinal direction. Tissue magnetization can be measured by rotating the longitudinal magnetization into the plane perpendicular to the direction of \mathbf{B}_0 (the transverse plane). The magnetization can be rotated out of the longitudinal direction into the transverse plane by irradiating tissue with radio frequency (RF) electromagnetic waves at just the right frequency (the Larmor frequency, equation 2.1) and with the magnetic field component perpendicular to the external magnetic field. A 90° RF pulse is a burst of radio waves at the Larmor frequency and of the right strength and duration to rotate the longitudinal magnetization by 90° into the transverse plane where it can be measured. However, the need to perform spatial encoding in magnetic resonance imaging (section 2.2) requires a time gap between the 90° RF pulse and signal measurement. The MR signal is measured during the rephasing (echo) of the transverse magnetization. Rephasing of the magnetization is accomplished by applying a 180° rephasing pulse in spin echo (SE) imaging or by a gradient reversal in gradient echo (GE) imaging.

2.2 Spatial encoding in magnetic resonance imaging (MRI)

The most common method of data acquisition and image reconstruction in MR imaging is two-dimensional Fourier transform (2DFT) imaging. In 2DFT, a particular plane of tissue is excited and data are acquired from that entire plane during signal measurement. The plane or slice is selected during tissue excitation by sending a narrow frequency range of RF pulses into the patient while applying a magnetic gradient along the slice-select direction (figure 2.1a). This process is called selective excitation, e.g. the pulse sequence of figure 2.6 excites a slice in the z -direction. The location of the slice is determined by the concurrence between the radio wave frequencies sent into the patient and the resonant frequencies in the patient due to the applied static magnetic field and gradient. The width of the selected slice is determined by the strength of the slice selection gradient and the range of frequencies

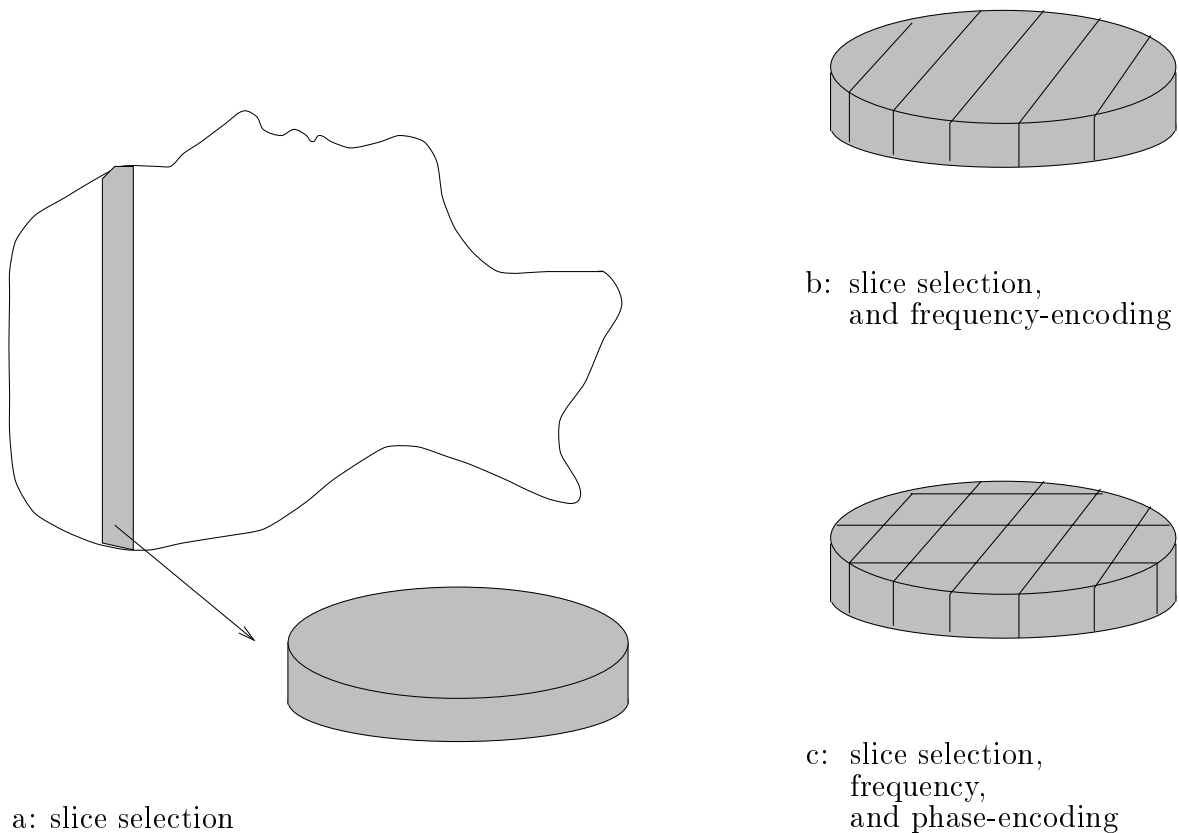


Figure 2.1: Spatial encoding in MRI: a) selective excitation is achieved by sending a narrow frequency range of RF pulses into the patient while applying a magnetic gradient, b) the frequency-encoding gradient divides the selected slice in bands, and c) the phase-encoding gradient divides the bands in voxels. See also the pulse sequence diagram in figure 2.6.

(the bandwidth) of the RF pulse. A thinner slice results from either a steeper gradient or a narrower frequency bandwidth of the RF pulse.

Resolution within the selected slice is achieved by applying gradient magnetic fields along the in-plane directions before and during signal measurement. If, for example, the in-plane directions are the x - and y -directions and the read-out (or frequency-encoding) gradient is applied along the x -direction during signal measurement (as in figure 2.6), the resonant frequency is altered as a function of x -location, spreading the signal from the plane into a range of signals at slightly different resonant frequencies corresponding to different x -locations. As a result, the plane is divided into a series of bands, each band resonating at slightly different frequency (figure 2.1b). The number of frequency bands is equal to the number of measurements of the time dependent signal (usually 256), determining the resolution in the frequency-encoding direction.

However, with just encoding in the x -direction, the signals from different voxels in each frequency band cannot be resolved. To resolve the signal from each voxel, a number of different acquisitions (usually 256) must be acquired. Each is acquired with the same read-out gradient strength, so that the plane is separated into the same frequency bands on each repetition of the sequence. After the magnetization has been rotated into the transverse plane but before measurement of the signal of each sequence repetition, a gradient in the other in-plane direction (in this example the y -direction) is applied to encode the signals from voxels at different y -locations by the amount of relative precession or phase shift (see e.g. figure 2.6). Hence, this gradient is called a phase-encoding gradient. The amount of phase

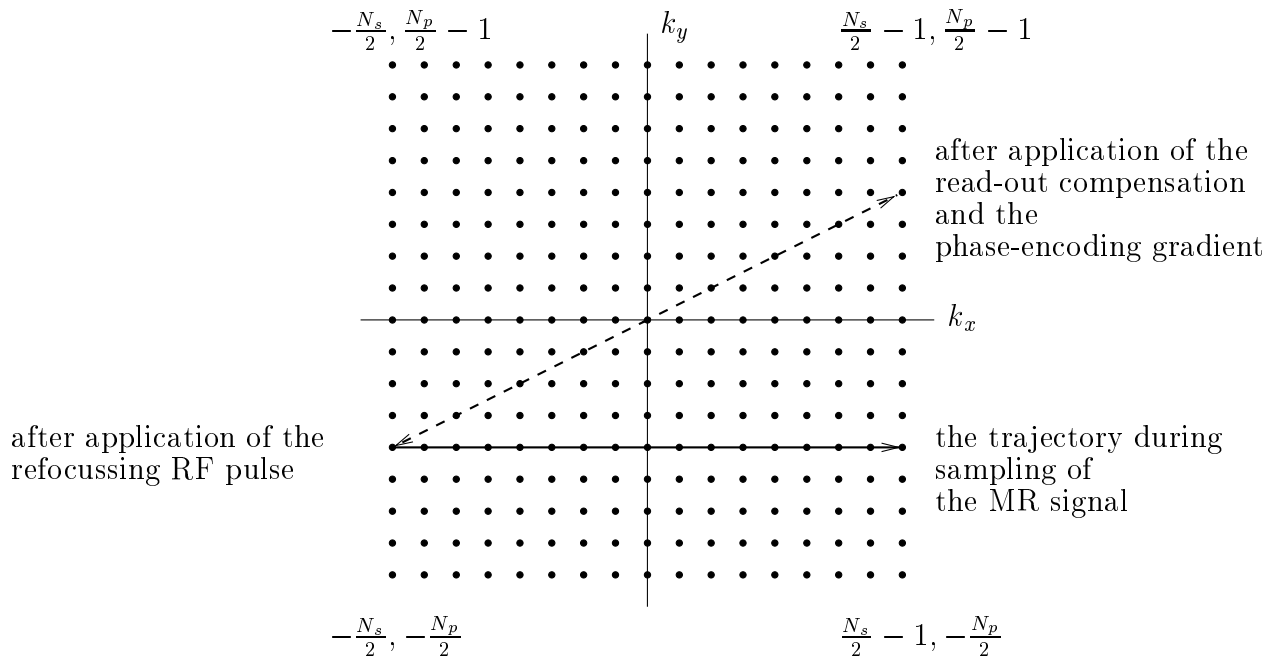


Figure 2.2: Trajectories in \mathbf{k} -space corresponding to the spin echo pulse sequence of figure 2.6. With N_s samples of each MR signal and N_p acquisitions or phase-encoding steps, the \mathbf{k} -space consists of $N_s \times N_p$ samples.

shift is determined by the strength and the duration of the phase-encoding gradient applied and by the location of tissue along the phase-encoding direction (in this example the y -axis). By measuring a number of acquisitions (usually 256), each with a unique phase-encoding gradient strength, individual voxels (usually 256) can be resolved along the phase-encoding direction within each frequency band (figure 2.1c). A two-dimensional Fourier transform is the mathematical method used to decode the signal strength from each voxel from the set of multiple acquisitions.

2.3 The \mathbf{k} -space

For a better understanding of some MR image artifacts, in particular those concerning reduced sampling (see chapter 5), it may be instructive to have a closer look at the signal matrix S . The signal matrix S of the excited slice consists of all acquired MR signals or profiles, the raw data sampling space. This data matrix is often called the \mathbf{k} -space, the spatial frequency domain. The acquisition of the profiles can be thought of as traversing this \mathbf{k} -space. The pattern of trajectories in \mathbf{k} -space depends on the type of pulse sequence applied. In two-dimensional Fourier transform imaging, the spatial frequencies k_x and k_y [rad/m] for a standard spin echo pulse sequence (schematically drawn in figure 2.6) are given by:

$$k_x = \gamma G_x n \Delta t, \quad (2.2)$$

$$k_y = -\gamma m \Delta G_y T_y, \quad (2.3)$$

where γ denotes the gyromagnetic ratio for protons [rad/(T s)], G_x the amplitude of the read-out gradient [T/m], Δt the sampling interval [s], ΔG_y the step-size [T/m] and T_y the duration [s] of the phase-encoding gradient. With $n \in [-\frac{N_s}{2}, \frac{N_s}{2} - 1]$ and $m \in [-\frac{N_p}{2}, \frac{N_p}{2} - 1]$, the \mathbf{k} -space consists of $N_s \times N_p$ samples. The trajectories in \mathbf{k} -space corresponding to the spin echo pulse sequence of figure 2.6 are schematically drawn in figure 2.2. The spatial frequencies k_x and k_y , due to the read-out compensation gradient and the phase-encoding gradient, are inverted by the the 180° RF refocussing pulse in the SE sequence (trajectories denoted by dashed lines in figure 2.2). The echo of the MR signal is sampled while applying the read-out gradient (trajectory denoted by the solid line in figure 2.2). The central part of the \mathbf{k} -space contains low spatial frequencies, relating to global object shape and contrast, the periphery of the \mathbf{k} -space contains high spatial frequencies relating to object detail.

2.4 Sources of image distortions in MRI

Slice selection and spatial encoding in MRI is achieved by superposing magnetic gradient fields on the static magnetic field. The image of the object is reconstructed from the acquired data assuming perfect static magnetic field homogeneity and linear gradients. In reality, magnetic field inhomogeneity and non-linearity of the gradients are sources of magnetic field errors resulting in geometry distortions. In the following, the different sources of magnetic field errors in MRI are briefly discussed.

2.4.1 Machine-related magnetic field errors

Gradient non-linearity

The magnetic field gradients in the x , y and z directions are produced by three sets of coils. The coils are designed to produce weak magnetic fields, that change linearly with position, e.g. applying a gradient in the x -direction ideally results in:

$$\mathbf{B}_{G_x}(x) = xG_x, \quad (2.4)$$

where x refers to the position, G_x is the amplitude of the gradient [T/m], and $\mathbf{B}_{G_x}(x)$ is the magnetic field [T] due to the gradient. However, in reality, non-perfect winding of the coils and eddy currents, generated by the changing gradients in conducting parts of the scanner, cause non-linear gradients. Figure 2.3 depicts how, in the one-dimensional case, non-linearity of a gradient results in geometry distortions:

$$x_1 = x + \frac{\Delta \mathbf{B}_{G_x}(x)}{G_x}, \quad (2.5)$$

where x_1 refers to the distorted position, and $\Delta \mathbf{B}_{G_x}(x)$ to the magnetic field error due to the non-linearity of the gradient. Non-linearity of the gradients results in slice distortion and in-plane distortions in the frequency- and phase-encoding directions (see section 2.5).

Magnetic field inhomogeneity

Magnetic fields are produced by resistive magnets, permanent magnets and superconducting magnets. In most commercial MRI scanners with higher magnetic fields strengths, superconducting magnets are used. The static magnetic field is produced by a current running

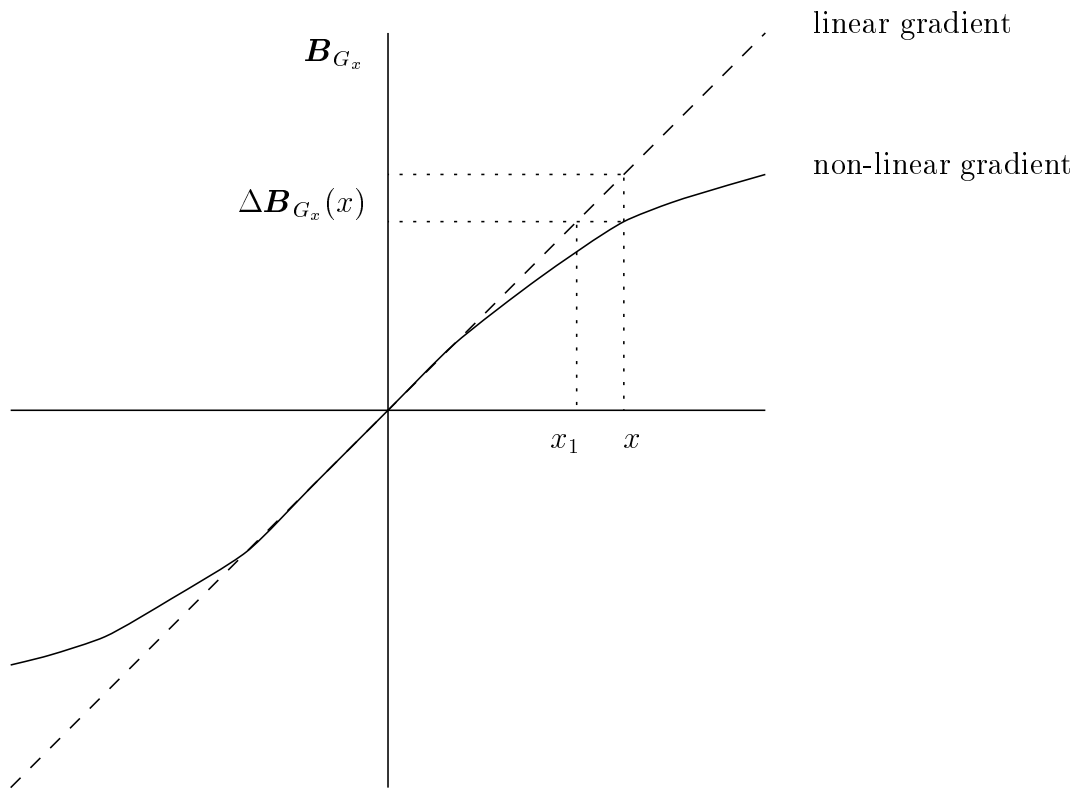


Figure 2.3: Gradient non-linearity results in geometric distortion. MR signal from spins at position x is depicted at position x_1 in the MR image.

through coil windings immersed in liquid helium. A typical coil arrangement and corresponding magnetic field lines are schematically drawn in figure 2.4 for a four coil solenoid. Perfect magnetic field homogeneity can not be achieved, because of 1) the divergence of the magnetic field lines at the end of the coil, 2) the impossibility of perfectly winding the superconducting wire on the coil, 3) slight variations of current densities in the wire, and 4) the disturbance of the magnetic field by metal in the environment of the scanner. Magnetic field inhomogeneity results in slice distortion and in-plane distortions in the direction of the frequency-encoding gradient (see section 2.5).

2.4.2 Object-related magnetic field inhomogeneity

Magnetic susceptibility

Magnetic susceptibility is the property which relates the magnetization of an object to the applied magnetic field. When an object is placed in a magnetic field, electromagnetic interactions between the object and the magnetic field result in magnetic field perturbations. The lines of the magnetic field are dispersed within a diamagnetic object ($\chi < 0$) and thus the effective field within the object is reduced. The lines of the magnetic field are concentrated within a paramagnetic object ($\chi > 0$) and thus the effective field within the object is enhanced. Figure 2.5 shows schematically how the the applied magnetic field is perturbed by an object with a negative susceptibility value, e.g. human tissue ($\chi_{muscle} \approx -9 \times 10^{-6}$).

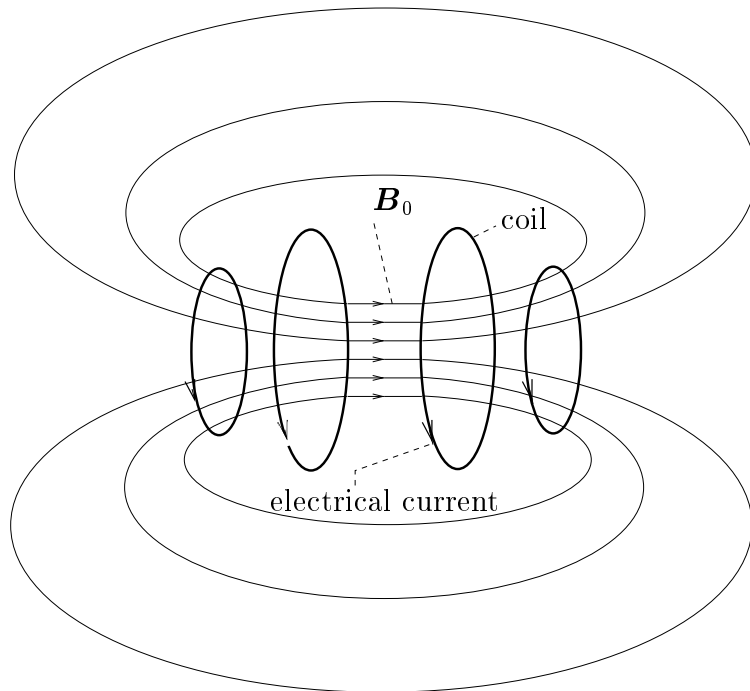


Figure 2.4: Divergence of the magnetic field lines at the end of a four coil solenoid is one of the sources of magnetic field inhomogeneity.

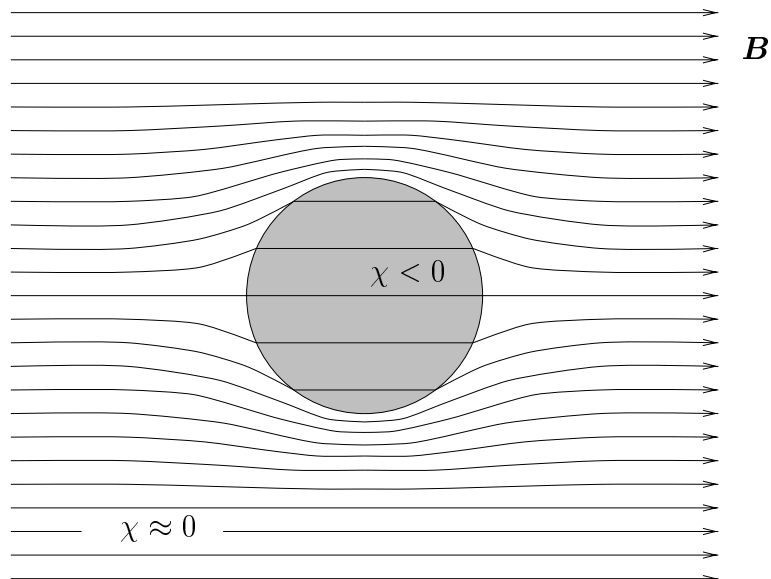


Figure 2.5: Magnetic field inhomogeneity due to susceptibility differences. The magnetic field lines diverge within a diamagnetic object ($\chi < 0$) in air ($\chi \approx 0$).

Chemical shift

After excitation, a nucleus emits energy at a frequency proportional to the magnetic field strength felt at the nucleus itself. Since the magnetic shielding of a nucleus by the electron clouds that surround it depends upon the chemical structure of a molecule and the location of the nucleus within the molecule, the resonant frequency depends on the molecular environment of the nucleus. This small variation in resonant frequency based on the shielding of the nucleus, is given the term chemical shift. Protons in fat experience a magnetic field, which is 3.2 parts per million (ppm) weaker than the magnetic field experienced by protons in water (Dixon 1984). In 2-dimensional Fourier transform (2DFT) imaging, the read-out gradient relates the frequency of a proton to its location along the read-out gradient axis. The consequence for MRI is, that the fat-containing tissues will be shifted with respect to the other tissues.

2.5 Two-dimensional Fourier transform (2DFT) imaging

In an ideal 2DFT imaging experiment with relaxation effects ignored, the n -th time sample of the signal after the m -th phase-encoding step is given by:

$$S(n, m) = \int_{-\infty}^{\infty} \int_{-\infty}^{\infty} \int_{-\infty}^{\infty} A(x, y, z) e^{i\Phi(x, y, z, n, m)} dx dy dz, \quad (2.6)$$

where, $A(x, y, z)$ represents the distribution of transverse magnetization immediately after application of a selective excitation pulse while $\Phi(x, y, z, n, m)$ describes the spatially dependent phase evolution of the excited spin population. A complex image $A'(u, v)$ is obtained by a discrete 2D inverse Fourier transformation of the 2D acquisition matrix $S(n, m)$

$$A'(u, v) = \sum_{n=-\frac{N_s}{2}}^{\frac{N_s}{2}-1} \sum_{m=-\frac{N_p}{2}}^{\frac{N_p}{2}-1} S(n, m) e^{-i\Phi(u, v, n, m)}, \quad (2.7)$$

where N_s represents the number of time samples and N_p the number of phase-encoding steps. When imaging conditions are ideal (linear gradients, data sampling according to Nyquist ($\gamma G_x \text{FOV} T_x \leq 2\pi$ along the frequency-encoding direction and $\gamma \Delta G_y \text{FOV} T_y \leq 2\pi$ along the phase-encoding direction), etc.), the modulus of the reconstructed image constitutes a faithful 2D representation of the imaged slice. FOV is the field of view [m], T_x is the duration of the read-out gradient [s], T_y is the duration of the phase-encoding gradient [s], G_x is the read-out gradient [T/m], ΔG_y is the step-size of the phase-encoding gradient and γ is the proton gyromagnetic ratio ($2\pi \cdot 42.57602 \cdot 10^6$ [rad/(T s)]).

The signal matrix S for a particular object depends on the type of pulse sequence that is applied for data acquisition. For the commonly employed 2D spin echo sequence (schematically drawn in figure 2.6), with slice selection along z , phase encoding along y , and frequency-encoding along x , a slice with thickness Δz at position z is excited by applying an RF (radio frequency) pulse with bandwidth $\Delta\omega = \gamma\Delta z G_z$ at offset frequency $\omega(z) = \gamma z G_z$. In spin echo imaging, the 180° RF pulse inverts the dephasing of the magnetization due to the read-out compensation gradient and the phase-encoding gradient, so that, with a properly

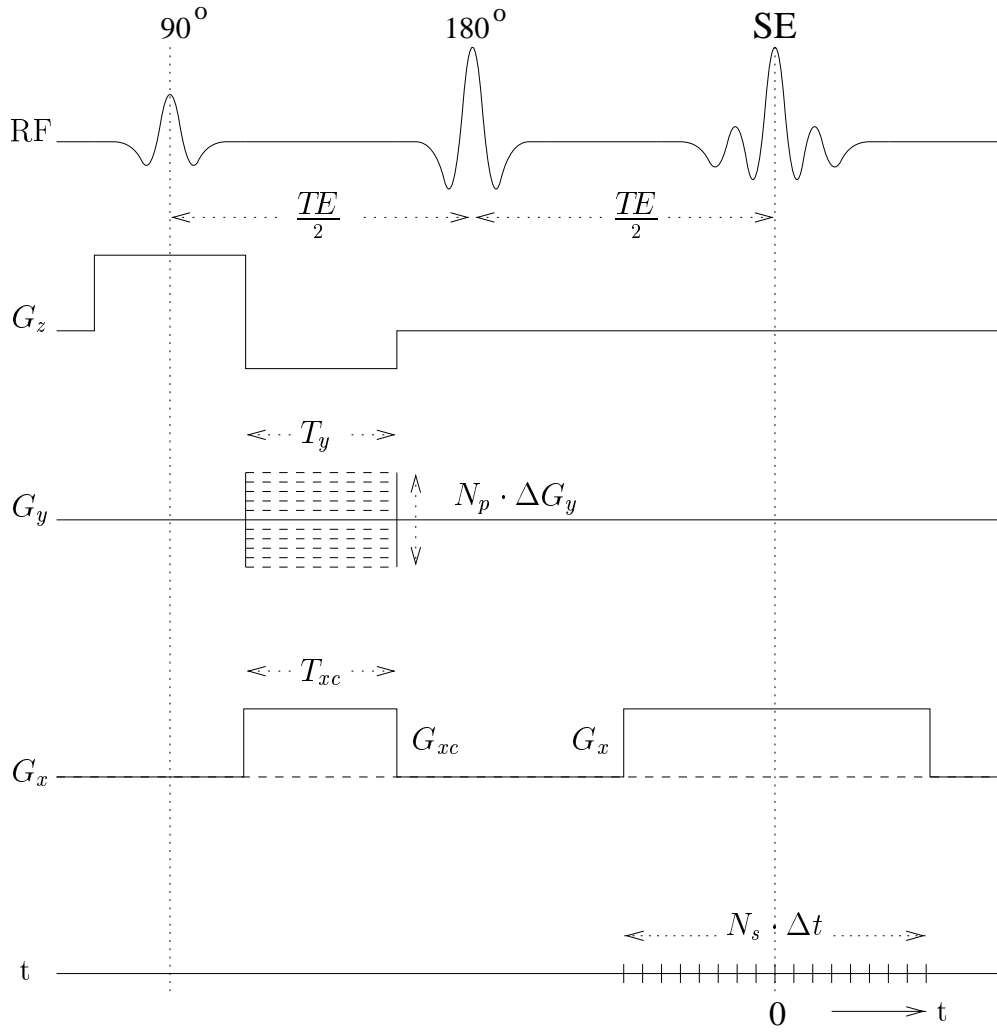


Figure 2.6: Definition of the generic spin echo single slice 2DFT pulse and gradient sequences.

balanced slice selection gradient, the phase evolution during the acquisition period is given by:

$$\Phi(x, y, z, n, m) = -\gamma x G_{xc} T_{xc} + \gamma x G_x \left(n + \frac{N_s}{2}\right) \Delta t - \gamma y m \Delta G_y T_y. \quad (2.8)$$

Here γ denotes the gyromagnetic ratio for protons [rad/(T s)], Δt the sampling interval [s], G_{xc} the amplitude [T/m] and T_{xc} the duration [s] of the read-out compensation gradient, G_x the amplitude of the read-out gradient [T/m], ΔG_y the step-size [T/m] and T_y the duration [s] of the phase-encoding gradient. Further t is chosen equal to 0 at the centre of the acquisition window (figure 2.6).

With a properly balanced read-out gradient, i.e. $-G_{xc} T_{xc} + G_x \Delta t \frac{N_s}{2} = 0$, and in the absence of field inhomogeneities, the echo will be centred in the acquisition window ($t = 0$) and equation 2.8 simplifies to:

$$\Phi(x, y, z, n, m) = \gamma x G_x n \Delta t - \gamma y m \Delta G_y T_y. \quad (2.9)$$

Here is $n \in [-\frac{N_s}{2}, \frac{N_s}{2} - 1]$ and $m \in [-\frac{N_p}{2}, \frac{N_p}{2} - 1]$.

2.5.1 Slice selection in the presence of magnetic field inhomogeneity and gradient non-linearity

In the presence of field inhomogeneities and gradient non-linearity, the applied excitation pulse, intended to excite a slice Δz at z_0 in 2DFT, effectively excites all points z_1 which satisfy the excitation condition:

$$\gamma z G_z = \gamma z_1 G_z + \gamma \Delta \mathbf{B}_0(x, y, z_1) + \gamma \Delta \mathbf{B}_{G_z}(x, y, z_1), \quad (2.10)$$

where $z \in [(z_0 - \frac{\Delta z}{2}), (z_0 + \frac{\Delta z}{2})]$ and $[\gamma G_z(z_0 - \frac{\Delta z}{2}), \gamma G_z(z_0 + \frac{\Delta z}{2})]$ encompasses the band of excitation frequencies. The inhomogeneity of the static field $\Delta \mathbf{B}_0$ and the non-linearity of the slice selection gradient $\Delta \mathbf{B}_{G_z}$ thus cause a distortion of the slice given by:

$$z_1 = z - \frac{\Delta \mathbf{B}_0(x, y, z_1)}{G_z} - \frac{\Delta \mathbf{B}_{G_z}(x, y, z_1)}{G_z}, \quad (2.11)$$

where z refers to the nominal position and z_1 to the actual position. Note the transcendental character of this equation and the negative sign of $\Delta \mathbf{B}_0$ and $\Delta \mathbf{B}_{G_z}$ which is sometimes overlooked in literature (Ericsson et al. 1988; Posse and Aue 1990; Ogawa and Lee 1990).

2.5.2 In-plane image distortions in spin echo (SE) imaging

In addition to slice selection effects, the presence of static field inhomogeneities and non-linearity of the frequency-encoding gradient and the phase-encoding gradient disturbs the phase evolution of the excited spin population. In spin echo imaging, the echo of the MR signal is recalled by a 180° RF pulse which rephases the magnetization. At the centre of the echo ($n = 0$ in equation 2.12), dephasing due to $\Delta \mathbf{B}_0(x, y, z_1)$ and $\Delta \mathbf{B}_{G_x}(x, y, z_1)$ is eliminated, but the dephasing develops as time increases in either direction away from the centre of the echo signal ($n < 0$ or $n > 0$ in equation 2.12):

$$\begin{aligned} \Phi^*(x, y, z_1, n, m) &= \Phi(x, y, z_1) + \gamma \Delta \mathbf{B}_0(x, y, z_1) n \Delta t + \gamma \Delta \mathbf{B}_{G_x}(x, y, z_1) n \Delta t \\ &\quad - \gamma m \Delta \mathbf{B}_{G_y}(x, y, z_1) T_y. \end{aligned} \quad (2.12)$$

Here Φ denotes the undisturbed phase evolution (equation 2.9), $\Delta \mathbf{B}_0(x, y, z_1)$ incorporates the object-induced and system-related imperfections of the static field \mathbf{B}_0 , $\Delta \mathbf{B}_{G_x}(x, y, z_1)$ and $\Delta \mathbf{B}_{G_y}(x, y, z_1)$ are the non-linearity in the frequency- and phase-encoding gradients, and Φ^* describes the perturbed phase evolution. Interpretation of the effect of the disturbances follows from rewriting equation 2.12 into the following format:

$$\Phi^*(x, y, z_1, n, m) = \Phi(x_1, y_1, z_1, n, m). \quad (2.13)$$

From this equation it follows that, with $G_y = m \Delta G_y$:

$$\begin{aligned} x_1 &= x + \frac{\Delta \mathbf{B}_0(x, y, z_1)}{G_x} + \frac{\Delta \mathbf{B}_{G_x}(x, y, z_1)}{G_x}, \\ y_1 &= y + \frac{\Delta \mathbf{B}_{G_y}(x, y, z_1)}{G_y}, \end{aligned} \quad (2.14)$$

where x and y refer to the nominal position and x_1 and y_1 to the distorted position. The derivation of the above formulae relies on the assumption that $\Delta \mathbf{B}_{G_y}(x, y, z)/G_y = c(x, y, z)$, that is, the relative error in the y -gradient is independent of the strength of the y -gradient. If

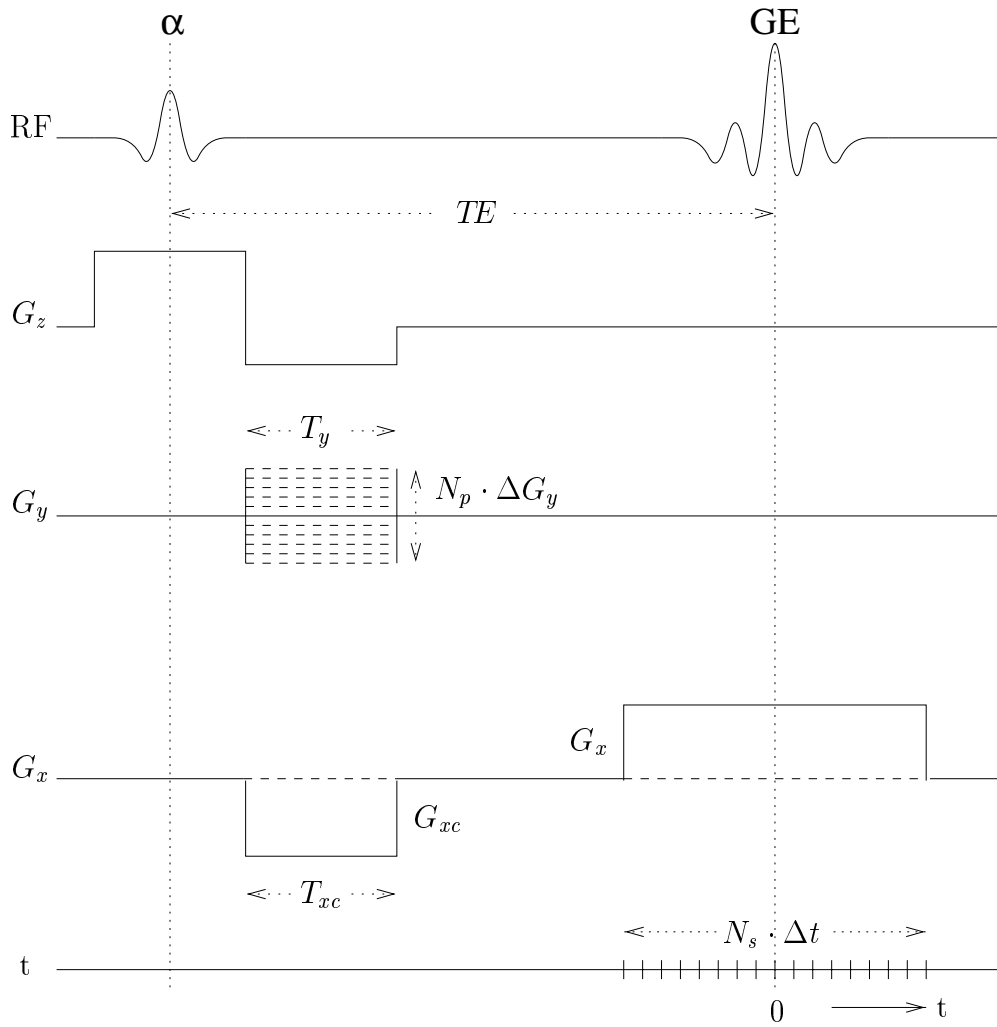


Figure 2.7: Definition of the generic gradient echo single slice 2DFT pulse and gradient sequences.

this were not the case, different phase-encoding steps would be corrupted by different errors which would make the analysis far more complicated. In SE imaging, geometric distortions and concurrent intensity distortions in the frequency-encoding direction are caused by static field inhomogeneity and non-linearity of the frequency-encoding gradient, and in the phase-encoding direction, distortions are solely caused by non-linearity of the phase-encoding gradient (equation 2.14).

2.5.3 In-plane image distortions in gradient echo (GE) imaging

For a gradient echo sequence, schematically drawn in figure 2.7, slice distortion is given by equation 2.11 as in spin echo imaging. The echo signal of the transverse magnetization is produced by gradient reversal and the phase evolution during the acquisition period is given by:

$$\Phi(x, y, z_1, n, m) = \gamma x G_{xc} T_{xc} + \gamma x G_x \left(n + \frac{N_s}{2} \right) \Delta t + \gamma y m \Delta G_y T_y. \quad (2.15)$$

Note that in a GE sequence, the read-out compensation gradient has a negative amplitude, whereas this gradient has a positive amplitude in a SE sequence. With a properly balanced read-out gradient, i.e. $G_{xc} T_{xc} + G_x \Delta t \frac{N_s}{2} = 0$, and in the absence of field inhomogeneities,

the echo will be centred in the acquisition window ($t = 0$) and equation 2.15 simplifies to:

$$\Phi(x, y, z_1, n, m) = \gamma x G_x n \Delta t + \gamma y m \Delta G_y T_y. \quad (2.16)$$

Gradient non-linearity $\Delta \mathbf{B}_{G_x}$ and $\Delta \mathbf{B}_{G_y}$ results in geometry distortions in the same way as in spin echo imaging, but the influence of magnetic field inhomogeneity is different in one aspect. Magnetic field inhomogeneity results in geometry distortions in the direction of the frequency-encoding gradient, as in spin echo imaging, but also in dephasing. In gradient echo imaging, the echo signal of the transverse magnetization is produced by gradient reversal which does not eliminate the dephasing effects of magnetic field inhomogeneity. At the centre of the echo ($n = 0$ in equation 2.17), dephasing is given by $\gamma TE \Delta \mathbf{B}_0(x, y, z_1)$. Dephasing begins at the excitation pulse and progresses with time throughout the sampling period:

$$\Phi^*(x, y, z_1, n, m) = \Phi(x, y, z_1) + \gamma \Delta \mathbf{B}_0(x, y, z_1) n \Delta t + \gamma TE \Delta \mathbf{B}_0(x, y, z_1). \quad (2.17)$$

Here Φ denotes the undisturbed phase evolution (equation 2.16), $\Delta \mathbf{B}_0(x, y, z_1)$ incorporates the object-induced and system-related imperfections of the static field \mathbf{B}_0 , TE is the echo time and Φ^* describes the perturbed phase evolution. Interpretation of the effect of the disturbances follows from rewriting equation 2.17 into the following format:

$$\Phi^*(x, y, z_1, n, m) = \Phi(x_1, y_1, z_1, n, m) + \Delta \Phi(x, y, z_1). \quad (2.18)$$

From this equation it follows that:

$$\begin{aligned} x_1 &= x + \frac{\Delta \mathbf{B}_0(x, y, z_1)}{G_x} \\ \Delta \Phi(x, y, z_1) &= \gamma TE \Delta \mathbf{B}_0(x, y, z_1). \end{aligned} \quad (2.19)$$

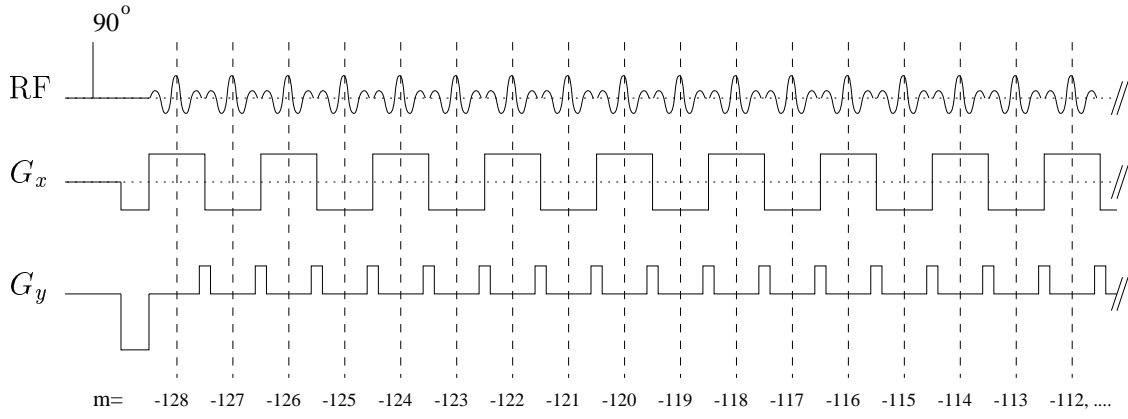
Magnetic field inhomogeneity results in geometry distortions in the frequency-encoding direction and in signal loss due to dephasing (Gore 1988), which increases with echo time.

2.5.4 In-plane image distortions in echo planar imaging (EPI)

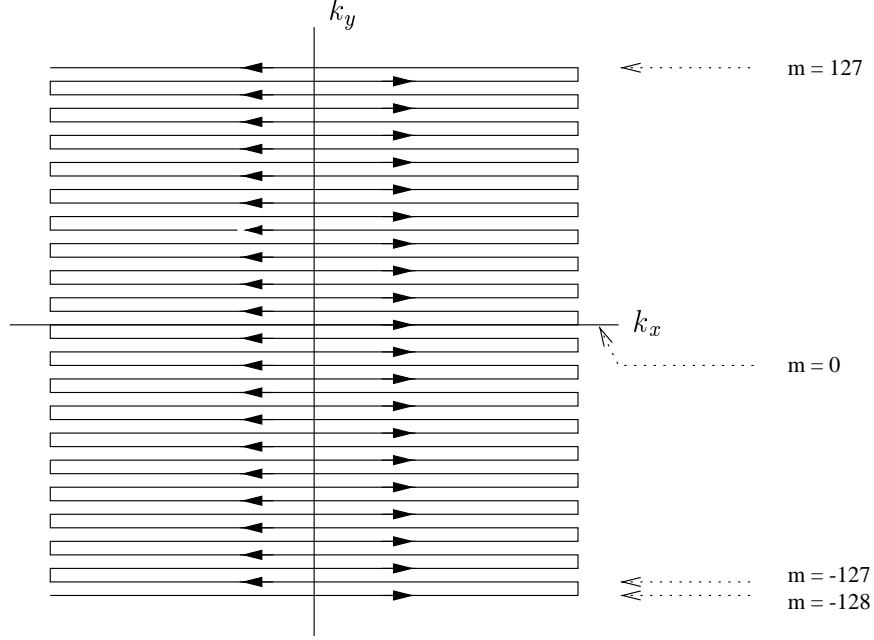
Echo planar imaging is a fast imaging method which acquires a number of profiles after a single excitation. The spatial information is encoded by an oscillating frequency-encoding gradient in combination with a small and constant phase-encoding gradient, thus, as in GE imaging, the echos of the MR signal are produced by gradient reversals (Mansfield 1977). In a variant of EPI, the constant phase-encoding gradient is replaced by a series of short phase-encoding gradient pulses (figure 2.8a). The corresponding trajectories are depicted in figure 2.8b. A more detailed diagram of an EPI sequence, with gradient amplitudes and timings denoted, is given in figure 2.9, for which the phase evolution is given by:

$$\begin{aligned} \Phi(x, y, z_1, n, m) &= (-1)^{|m|} \gamma x G_{xc} T_{xc} + (-1)^{|m|} \gamma x G_x \left(n + \frac{N_s}{2} \right) \Delta t \\ &\quad + \gamma y G_{yc} T_{yc} + \gamma y G_y T_y \left(m + \frac{N_p}{2} \right). \end{aligned} \quad (2.20)$$

Here G_{yc} denotes the amplitude [T/m] and T_{yc} the duration [s] of the phase-encoding compensation gradient, G_y the amplitude [T/m] and T_y the duration [s] of the phase-encoding



a



b

Figure 2.8: a) Diagram of an echo planar imaging pulse sequence with an oscillating frequency-encoding gradient and a series of short phase-encoding gradient pulses after a single excitation. b) Diagram of the corresponding trajectories in \mathbf{k} -space.

gradient. Further t is chosen equal to 0 at the centre of the acquisition window of the central echo (figure 2.9). With properly balanced frequency and phase-encoding gradients, i.e. $G_{xc}T_{xc} + G_x\Delta t\frac{N_s}{2} = 0$ and $G_{yc}T_{yc} + G_yT_y\frac{N_p}{2} = 0$, and in the absence of field inhomogeneities, equation 2.20 simplifies to:

$$\Phi(x, y, z_1, n, m) = (-1)^{|m|}\gamma x G_x n \Delta t + \gamma y G_y T_y m. \quad (2.21)$$

Gradient non-linearity $\Delta\mathbf{B}_{G_x}$ and $\Delta\mathbf{B}_{G_y}$ results in geometry distortions in the same way as in spin echo imaging. The presence of field inhomogeneities disturbs the phase evolution of the excited spin population as follows:

$$\begin{aligned} \Phi^*(x, y, z_1, n, m) = & \Phi(x, y, z_1, n, m) + \gamma\Delta\mathbf{B}_0(x, y, z_1)n\Delta t \\ & + \gamma\Delta\mathbf{B}_0(x, y, z_1)m\Delta T_y + \gamma TE\Delta\mathbf{B}_0(x, y, z_1). \end{aligned} \quad (2.22)$$

Here Φ denotes the undisturbed phase evolution (equation 2.21), $\Delta\mathbf{B}_0(x, y, z_1)$ incorporates the object-induced and system-related imperfections of the static field \mathbf{B}_0 , ΔT_y is the echo

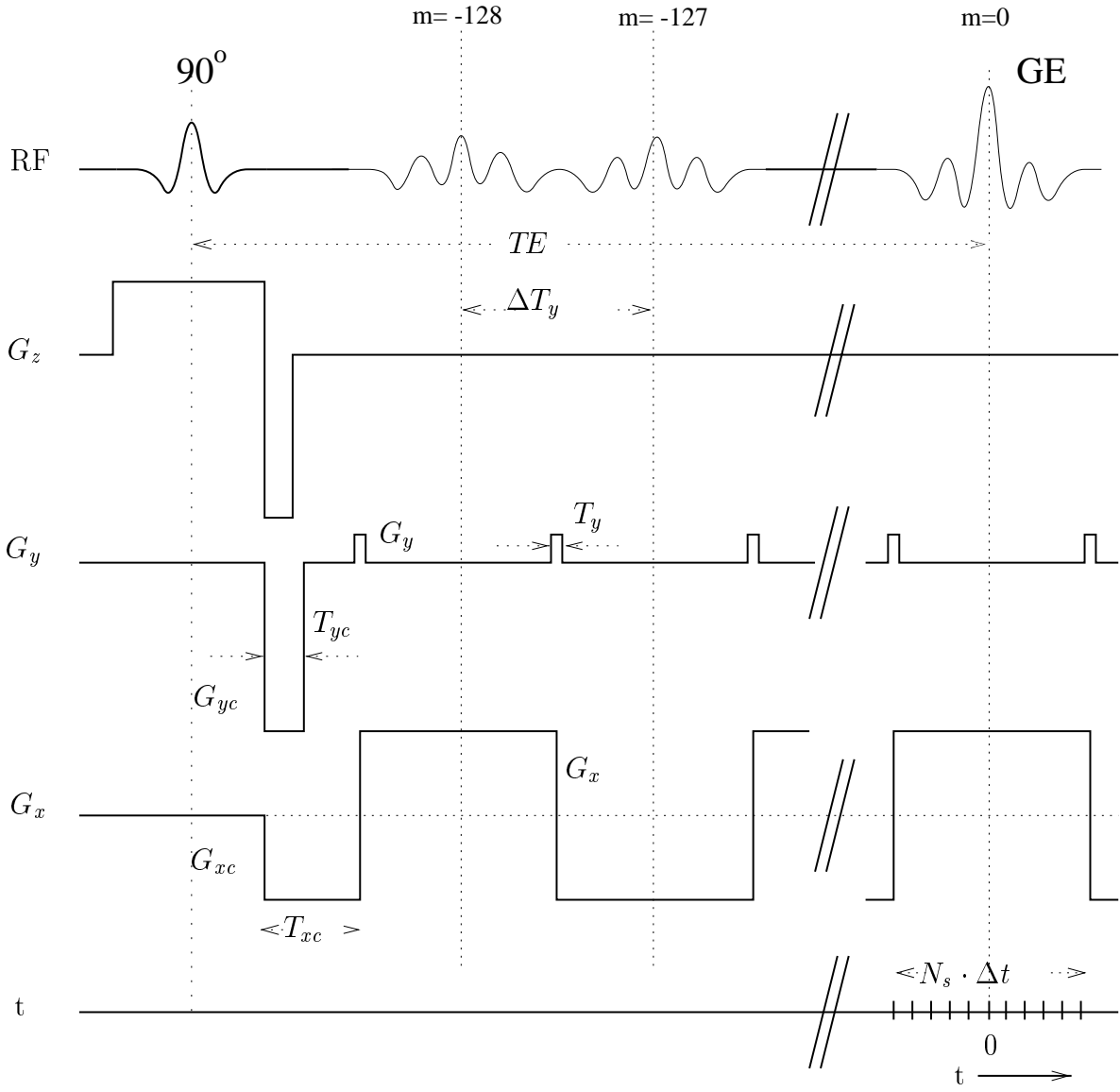


Figure 2.9: Definition of the generic echo planar imaging single slice 2DFT pulse and gradient sequences.

spacing, TE is the echo time and Φ^* describes the perturbed phase evolution. Interpretation of the effect of the disturbances follows from rewriting equation 2.22 into the following format:

$$\Phi^*(x, y, z_1, n, m) = \Phi(x_1, y_1, z_1, n, m) + \Delta\Phi(x, y, z_1). \quad (2.23)$$

From this equation it follows that:

$$\begin{aligned} x_1 &= x + (-1)^{|m|} \frac{\Delta\mathbf{B}_0(x, y, z_1)}{G_x} \\ y_1 &= y + \frac{\Delta\mathbf{B}_0(x, y, z_1)}{G_y} \frac{\Delta T_y}{T_y} \\ \Delta\Phi(x, y, z_1) &= \gamma TE \Delta\mathbf{B}_0(x, y, z_1). \end{aligned} \quad (2.24)$$

Geometric distortions occur in both the frequency and the phase-encoding direction. However, distortions in the phase-encoding direction dominate distortions in the frequency-encoding direction, since $\frac{T_y}{\Delta T_y} G_y \ll G_x$. As in gradient echo imaging, magnetic field inhomogeneity also results in signal loss due to dephasing, which increases with echo time.

Equations 2.24 were derived for a single shot EPI sequence, that is, all 256 profiles were acquired after a single excitation. Distortions are reduced in multiple shot EPI sequences (see chapter 5).

Chapter 3

Measurement and correction of
geometric distortions in MRI caused
by machine imperfections

3.1 Introduction

Some applications in medicine put strong demands on the spatial accuracy of the imaging techniques being employed. Experience shows that magnetic resonance imaging (MRI) does not generally satisfy these requirements for stereotaxy (Schad et al. 1987a), stereotactic radiotherapy (Ehricke and Schad 1992; Kooy et al. 1994; Schad et al. 1994), stereotactic neurosurgery (Michiels et al. 1994) and radiotherapy treatment planning of brain tumours (Schad et al. 1987b) and thoracic and abdominal tumours (Fraass et al. 1987). Spatial accuracy in MRI is limited by the inhomogeneity of the static magnetic field \mathbf{B}_0 and the nonlinearity of the imaging gradients G_x , G_y and G_z . The nonlinearity of the gradients is often considered a matter of system and sequence design (Bakker et al. 1992; O'Donnell and Edelstein 1985; Kawanaka and Takagi 1986) and the inhomogeneity of the static field is known to stem from the system (Bakker et al. 1992; Kawanaka and Takagi 1986; Sekihara et al. 1984) and from the magnetic properties of the object itself (Lüdeke et al. 1985; Edmonds and Wormald 1988; Ericsson et al. 1988; Chu et al. 1990; Posse and Aue 1990; Bhagwandien et al. 1992a). As has been recognized in previous studies (Lüdeke et al. 1985), the geometric distortion of MR images is affected by the strength, direction and polarity of the imaging gradients. Varying the gradients and using phantoms of known geometry thus, in principle, allows the system dependent field and gradient errors to be estimated and corrected for (Kawanaka and Takagi 1986; Bakker et al. 1992; Michiels et al. 1994; Schad et al. 1987a). However, the applicability of correction schemes in clinical practice depends on the stability of the field errors in time and under different imaging conditions. Schad et al. 1987a attributed image distortions to the occurrence of eddy currents, the severity of which depends theoretically on the amplitude of the pulsed gradients and the frequency of switching the gradients. Different imaging conditions, such as single or multiple slice acquisition, spin echo, gradient echo or echo planar imaging, result in different schemes of gradient switching and thus may result in different patterns of image distortions. This chapter describes the measurement and analysis of machine dependent image distortions with respect to the above mentioned aspects and evaluates the feasibility of correction methods in clinical practice.

3.2 Theoretical

In MR imaging, the frequency spectrum of the recorded signal is assumed to encode its spatial origin. The frequency spectrum is determined by the local magnetic fields the nuclei experience. When the local magnetic fields deviate from their expected values, for example, by having erroneous components in the static field \mathbf{B}_0 or the gradients G_x , G_y and G_z , the imaging process yields a distorted image (see figure 3.1 for the definition of the coordinate system).

In 2DFT SE imaging, with slice selection along z , phase encoding along y and frequency encoding along x , the distortion can be modeled by (see section 2.5):

$$z_1 = z - \frac{\Delta \mathbf{B}_{G_z}(x, y, z_1)}{G_z} - \frac{\Delta \mathbf{B}_0(x, y, z_1)}{G_z} \quad (3.1)$$

$$y_1 = y + \frac{\Delta \mathbf{B}_{G_y}(x, y, z_1)}{G_y} \quad (3.2)$$

$$x_1 = x + \frac{\Delta \mathbf{B}_{G_x}(x, y, z_1)}{G_x} + \frac{\Delta \mathbf{B}_0(x, y, z_1)}{G_x}. \quad (3.3)$$

Here (x, y, z) and (x_1, y_1, z_1) refer to the true and distorted positions, respectively. $\Delta\mathbf{B}_0$ denotes the deviation from the static field \mathbf{B}_0 , and $\Delta\mathbf{B}_{G_x}$, $\Delta\mathbf{B}_{G_y}$ and $\Delta\mathbf{B}_{G_z}$ designate the absolute errors (in tesla) in the gradient fields.

With respect to these expressions, several observations should be made. First, the derivation of the above formulae relies on the assumption that $\Delta\mathbf{B}_{G_y}(x, y, z)/G_y = c(x, y, z)$, that is, the relative error in the y -gradient is independent of the strength of the y -gradient. If this were not the case, different phase-encoding steps would be corrupted by different errors which would make the analysis far more complicated. Second, it should be realized that the interpretation of $\Delta\mathbf{B}_0$ in equations 3.1 through 3.3 is not a priori clear. Obviously, $\Delta\mathbf{B}_0$ reflects the inhomogeneity of the static field \mathbf{B}_0 . \mathbf{B}_0 itself, however, is merely a nominal value, which is operationally defined by the measured resonance frequency, f_0 . The procedure by which f_0 is measured will therefore critically affect the resultant images. An offset Δf_0 , for instance, will introduce a shift of the selected slice and a translation of the image in the read out direction. This might produce significant errors when deriving absolute positions from MR images (Bakker et al. 1992).

Several steps are involved in measuring and correcting system dependent geometric distortions in MR images of a particular object. The system dependent $\Delta\mathbf{B}_0$ and $\Delta\mathbf{B}_G$ distributions have to be derived by applying the experiments with different gradient directions to an object of known geometry which is known to leave \mathbf{B}_0 and the gradients undisturbed. Three-dimensional maps of $\Delta\mathbf{B}_0$ and $\Delta\mathbf{B}_G$ can be inferred from such experiments by interpolation techniques. Once the system dependent $\Delta\mathbf{B}_0$ and $\Delta\mathbf{B}_G$ maps are available, pointwise rectification of system induced geometric distortion in MR images of arbitrary objects can be performed by table lookup. This procedure only restores geometric errors and does not take care of any concomitant intensity distortions.

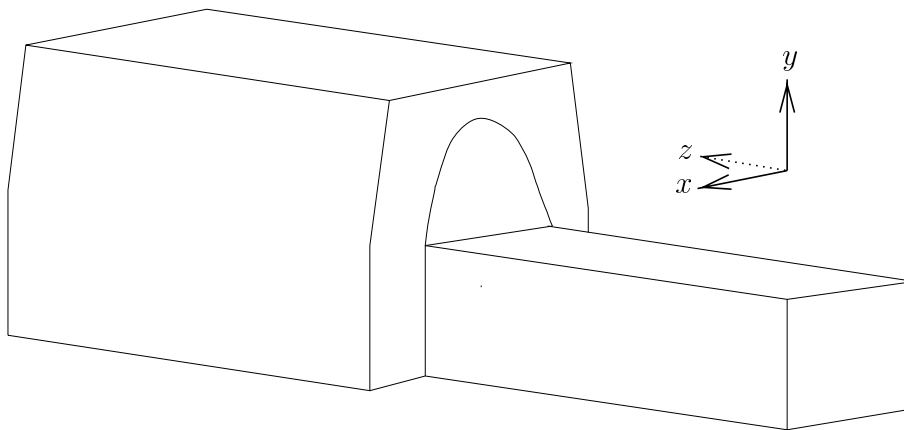


Figure 3.1: The coordinate system used for the experiments and calculations. The static magnetic field \mathbf{B}_0 is along the z -axis (caudo-cranial). The x -axis is in the left-right direction and the y -axis in the postero-anterior direction.

3.3 Methods and materials

3.3.1 Phantoms

Any object with a susceptibility different from air perturbs the magnetic field (Bakker et al. 1992; Bakker et al. 1993). This complicates the development of a phantom, which ideally should be a magnetic field probe that does not perturb the magnetic field. Bhagwandien

1994 showed by means of numerical analysis that field perturbation by a cylinder results in magnetic field offset and inhomogeneity along the length axis inside the cylinder. These phenomena are most pronounced towards the ends of the cylinder and for cylinders with small ratios of length and diameter. From the experiments by Dickinson 1951 and simulation studies by Bhagwandien 1994, it was concluded that the magnetic field perturbation extends over a distance l at the end of a cylinder given by $l/D < 2$, where D is the diameter of the cylinder. A grid phantom was developed, which consists of tubes with an outer diameter of 4 mm, an inner diameter of 3 mm and a length of 336 mm and thus the effective length usable for measurements is 320 mm. The tubes were placed in a 9x9 grid and mounted in 4 Perspex plates (figure 3.2). The spacing between the centres of the tubes is 42 mm. We left out the 4 tubes in the corners, so that the phantom fits exactly in the 1.5 T Philips Gyroscan S15. The phantom was designed for measurements on this scanner, but the phantom also fits in the 0.5 T Philips Gyroscan T5 and the 1.5 T Philips Gyroscan ACS-NT with wider bores. The phantom allows measurements within a 336x336x320 mm³ volume (with exception of the corners), which is usually large enough to cover fields of view applied when imaging for Radiotherapy Treatment Planning (RTP). The tubes are filled with CuSO₄ doped water, which makes the tube sections very well visible on the MR images. Our phantom can be regarded as a set of parallel long cylinders in air. Perturbation effects only occur at the ends of the tubes and in the Perspex plates.

The efficacy of correction methods was tested on a localization frame, in the following called the Leksell frame, which is a modification of the original design by Leksell 1951. The frame is an MRI compatible home built localization frame, which provides a reference coordinate system for MRI based irradiation beam positioning (figure 3.3). The plastic patient head cast and the frame are both attached to a base plate, so that patient and frame can be positioned reproducibly. The five Perspex plates of the frame and the base form a box, open at the caudal end, with outer dimensions width x height x length = 30 cm x 27 cm x 27 cm. This setup fits closely in the body coil of the Gyroscan S15 and provides enough space for a patient to be positioned with the head on a headrest, which is also used during radiotherapy. Plastic tubes with an inner diameter of 2 mm, filled with doped water (770 mg CuSO₄.5H₂O l⁻¹), were set in a Z shape in grooves milled in the Perspex plates. These tubes are well visible on MR images and serve as a reference coordinate system.

3.3.2 Measurement and correction

Imaging experiments were performed with 1.5 T whole body NMR systems (Gyroscan S15 and ACS-NT, Philips Medical Systems, Best, The Netherlands). The Gyroscan S15 was equipped with 3 mT/m gradients. The Gyroscan ACS-NT was equipped with 15 mT/m gradients and active shielding technology to reduce the influence of eddy currents, which may be induced by switching the gradients. In the imaging experiments, generally 5 mm slices were chosen resulting in a slice selection gradient of 3 mT/m. The directions of the read-out and the phase-encoding gradient were freely selectable. The strength of the read-out gradient was varied between 0.5 and 3.0 mT/m. Although nowadays MRI scanners like the Gyroscan ACS-NT are equipped with 15 mT/m gradients, in clinical practice the read-out gradient is usually operated up to about 3 mT/m in order to have sufficient signal to noise ratio.

The phantom was used as a 3D array of independent and identical field detectors, suitable for studying the system-dependent non-linearity of the gradients and the inhomogeneity of the static field. Equations 3.1 through 3.3 indicate that $\Delta\mathbf{B}_0(x, y, z)$, $\Delta\mathbf{B}_{G_x}(x, y, z)$ and

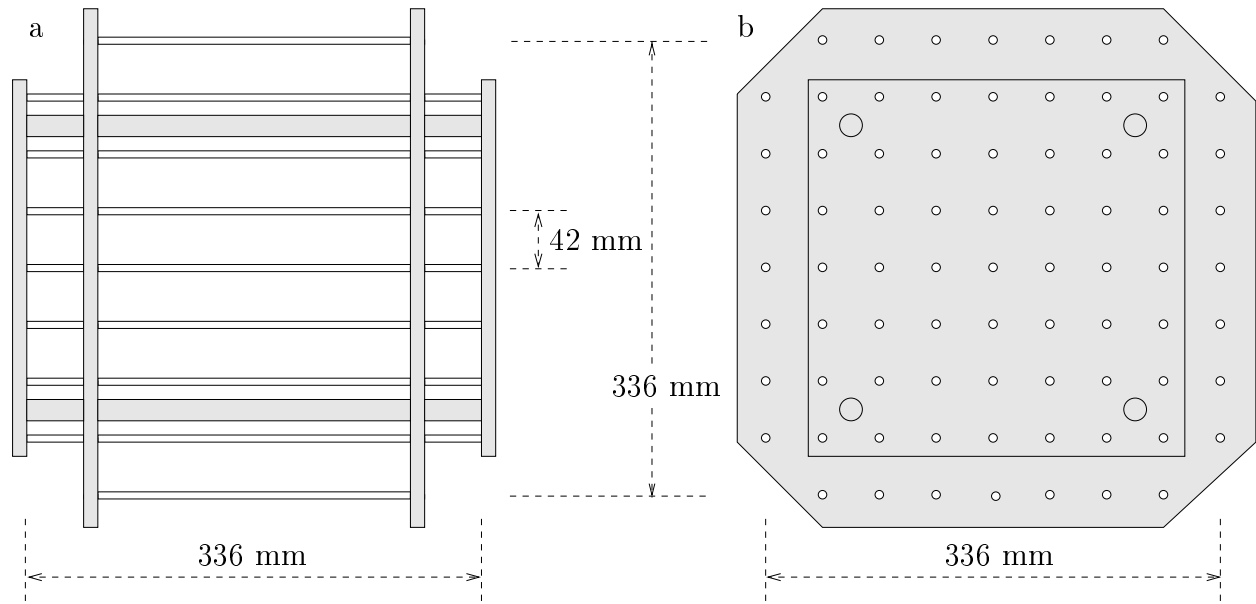


Figure 3.2: a) Lateral and b) front view on the phantom. The Perspex parts of the phantom are shaded.

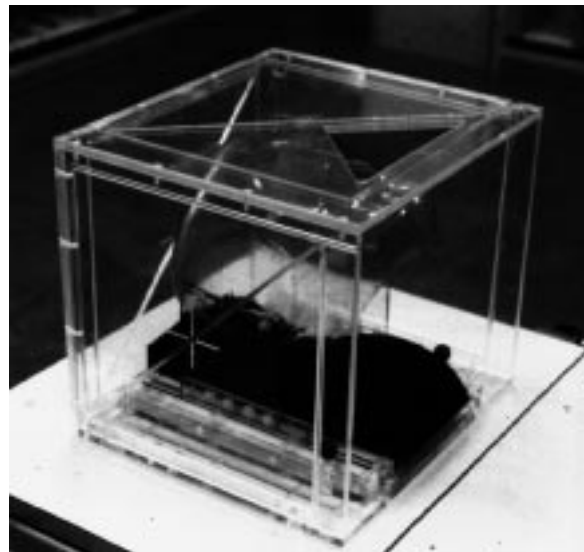


Figure 3.3: The localization frame with headcast and headrest.

$\Delta\mathbf{B}_{G_y}(x, y, z)$ can be determined from two otherwise identical transversal images acquired with interchanged directions of the phase encoding and frequency encoding gradients. With phase encoding along y and frequency encoding along x in experiment 1 and phase encoding along x and frequency encoding along y in experiment 2, the distortions for these experiments are given by:

$$y_1 = y + \frac{\Delta\mathbf{B}_{G_y}(x, y, z)}{G_y} \quad (3.4)$$

$$x_1 = x + \frac{\Delta\mathbf{B}_{G_x}(x, y, z)}{G_x} + \frac{\Delta\mathbf{B}_0(x, y, z)}{G_x} \quad (3.5)$$

$$y_2 = y + \frac{\Delta\mathbf{B}_{G_y}(x, y, z)}{G_y} + \frac{\Delta\mathbf{B}_0(x, y, z)}{G_y} \quad (3.6)$$

$$x_2 = x + \frac{\Delta\mathbf{B}_{G_x}(x, y, z)}{G_x}. \quad (3.7)$$

If the object geometry (x, y, z) is known, the errors $\Delta\mathbf{B}_{G_x}(x, y, z)$ and $\Delta\mathbf{B}_{G_y}(x, y, z)$ directly follow from equations 3.4 and 3.7:

$$\Delta\mathbf{B}_{G_y}(x, y, z) = G_y(y_1 - y) \quad (3.8)$$

$$\Delta\mathbf{B}_{G_x}(x, y, z) = G_x(x_2 - x), \quad (3.9)$$

where G_x and G_y are the phase-encoding gradients in the respective experiments. The static field error $\Delta\mathbf{B}_0(x, y, z)$ is derived by substitution of the gradient errors in equation 3.5 or 3.6:

$$\Delta\mathbf{B}_0(x, y, z) = G_x(x_1 - x_2) \quad (3.10)$$

or

$$\Delta\mathbf{B}_0(x, y, z) = G_y(y_2 - y_1), \quad (3.11)$$

where G_x and G_y are the frequency encoding gradients in the respective experiments. The gradient error $\Delta\mathbf{B}_{G_z}(x, y, z)$ can be determined in a similar way from pairs of coronal or sagittal images.

During experiments, caution was exercised with respect to the setting of the resonance frequency, f_0 . Under normal operating conditions, f_0 is determined prior to each individual scan for a 5 mm slice through the object at the level of the central slice of a multi-slice package. Since f_0 provides the link between the image matrix and the laboratory frame, it was kept constant for each series of related measurements.

System dependent $\Delta\mathbf{B}_0(x, y, z)$, $\Delta\mathbf{B}_{G_x}(x, y, z)$, $\Delta\mathbf{B}_{G_y}(x, y, z)$ and $\Delta\mathbf{B}_{G_z}(x, y, z)$ were determined from transversal, coronal and sagittal multiple slice imaging experiments on the phantom with for each acquisition the phantom positioned such that the tubes were perpendicular to the image plane. Static field and gradient field errors were determined at the phantom tube positions, from which 3D error maps were inferred by bicubic interpolation. Once the system dependent field errors are available, pointwise rectification of system induced geometric distortion in MR images of arbitrary objects can be performed by table look up. This procedure was tested in 2D on the phantom images and images of the home built Leksell frame.

3.3.3 Software tools

The following software tools were developed for the calculation of the field errors from the phantom images and for the correction of image distortions. The module TUBEPOS detects tube positions in the phantom images, using the regularity of the phantom geometry. The displacement of grid points relative to their known positions was always evaluated for the centres of gravity of the tubes. The centre of a tube section is calculated using an intensity-weighted filter of which the size is on the order of the diameter of the tube. The module CALCDB calculates the static and gradient field errors at the positions of the tubes and interpolates these 9x9 2D error maps to 256x256 2D error maps. The module CORIMAGE uses these images to calculate an inverse pixel transformation for correction of distorted MR images up to a field of view of 336 mm.

3.4 Results

3.4.1 Field error measurements

Figure 3.4 shows a superposition of a set of 11 transversal spin echo images of the phantom acquired on the Gyroscan S15 at z -coordinates between $z = -105$ mm and $z = 105$ mm with a step size of 21 mm. The grid indicates the real tube positions. Geometric distortions increase with increasing distance from the magnet isocentre. These distortions originate from static field inhomogeneity and non-linearity of the imaging gradients. Figure 3.5 shows the contributions $\Delta\mathbf{B}_0$, $\Delta\mathbf{B}_{G_y}$ and $\Delta\mathbf{B}_{G_z}$ in the central sagittal plane of the Gyroscan S15. Static field inhomogeneity depended on the pulse sequence parameters. In a single slice spin echo experiment with a weak read-out gradient (1.21 mT/m), static field errors ranged from -3 to 1 ppm within a field of view of 336 mm (figure 3.5 a). In a multiple slice experiment with a strong read-out gradient (2.94 mT/m), static field errors ranged from -7 to 4 ppm (figure 3.5 g). Gradient errors were stable under these variations of the imaging experiment and ranged from -4 to 4 mm. Similar measurements were performed on the newer generation Gyroscan ACS-NT. Static field errors ranged from -3 to 6 ppm (see figures 3.6 a and d), gradient G_y errors ranged from -5 to 5 mm (see figures 3.6 b and e) and gradient G_z errors ranged from -1 to 1 mm (see figures 3.6 c and f). Static field errors and gradient errors were stable under variation of the imaging experiments. Static field and gradient G_y errors on the ACS-NT scanner were as large or larger than the errors on the S15 scanner, indicating that increase of maximum gradient strength and implementation of active shielding technology do not imply improvement of static field homogeneity and gradient linearity. However, the active shielding technology does result in stability of static field inhomogeneity under different imaging conditions. Single or multiple slice imaging and variation of the read-out gradient strength did not influence the results of the field error measurements, which indicates that the more frequent gradient switching in multiple slice studies does not deteriorate field homogeneity. Obviously, the active shielding technology applied in the ACS-NT scanner indeed reduces the influence of eddy currents.

As discussed above, figure 3.5 shows the contributions $\Delta\mathbf{B}_0$, $\Delta\mathbf{B}_{G_y}$ and $\Delta\mathbf{B}_{G_z}$ in the central sagittal plane of the Gyroscan S15. The field errors were also measured in off centre planes by performing transversal, coronal and sagittal multiple slice experiments with for each acquisition the phantom positioned such that the tubes were perpendicular to the image plane. Table 3.1 shows the observed minimum and maximum errors of the static magnetic field and the gradient fields of the Gyroscan S15 for different volumes of interest. This table

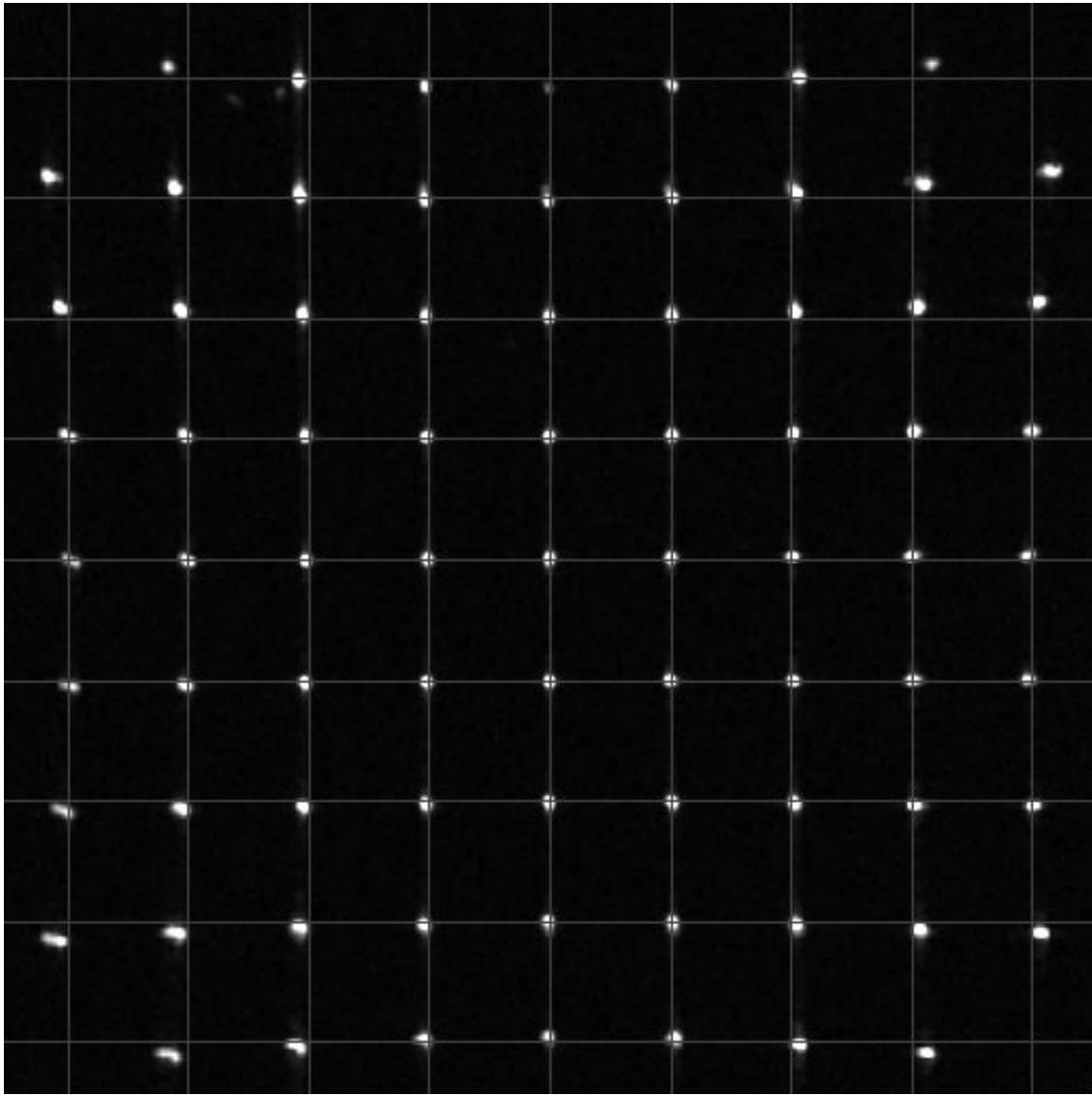


Figure 3.4: Superposition of a set of transversal spin echo phantom images. The grid indicates the real tube positions. The read out gradient $G_x=2.94$ mT/m, FOV=380 mm, off centre=20 mm anterior, $TR=851$ ms, $TE=30$ ms, slice thickness=5.0 mm, slice gap=16 mm.

shows that field errors increase with increasing distance from the magnet isocentre.

Static field and gradient non-linearity on the Gyroscan S15 have been followed between November 1991 and April 1993 using a phantom with tubes in a grid with 5 mm spacing. The figures 3.7 a and b show field errors in the central coronal plane at positions $(-15,15)$, $(15,15)$, $(-15,-15)$ and $(15,-15)$ with coordinates (x, z) in cm with respect to the position of the central tube in the phantom. The field errors proved to be stable within the experimental errors of ± 1 ppm for static field inhomogeneity and ± 1 mm for the gradient fields. A change in field errors was observed after yearly maintenance when shim settings were adjusted.

3.4.2 Distortion correction

The correction scheme consisting of acquisition of phantom images, detection of tube positions, calculation of the static field and gradient field error maps and finally the distortion correction was tested in studies on the phantom and the Leksell frame. Two sets of multiple

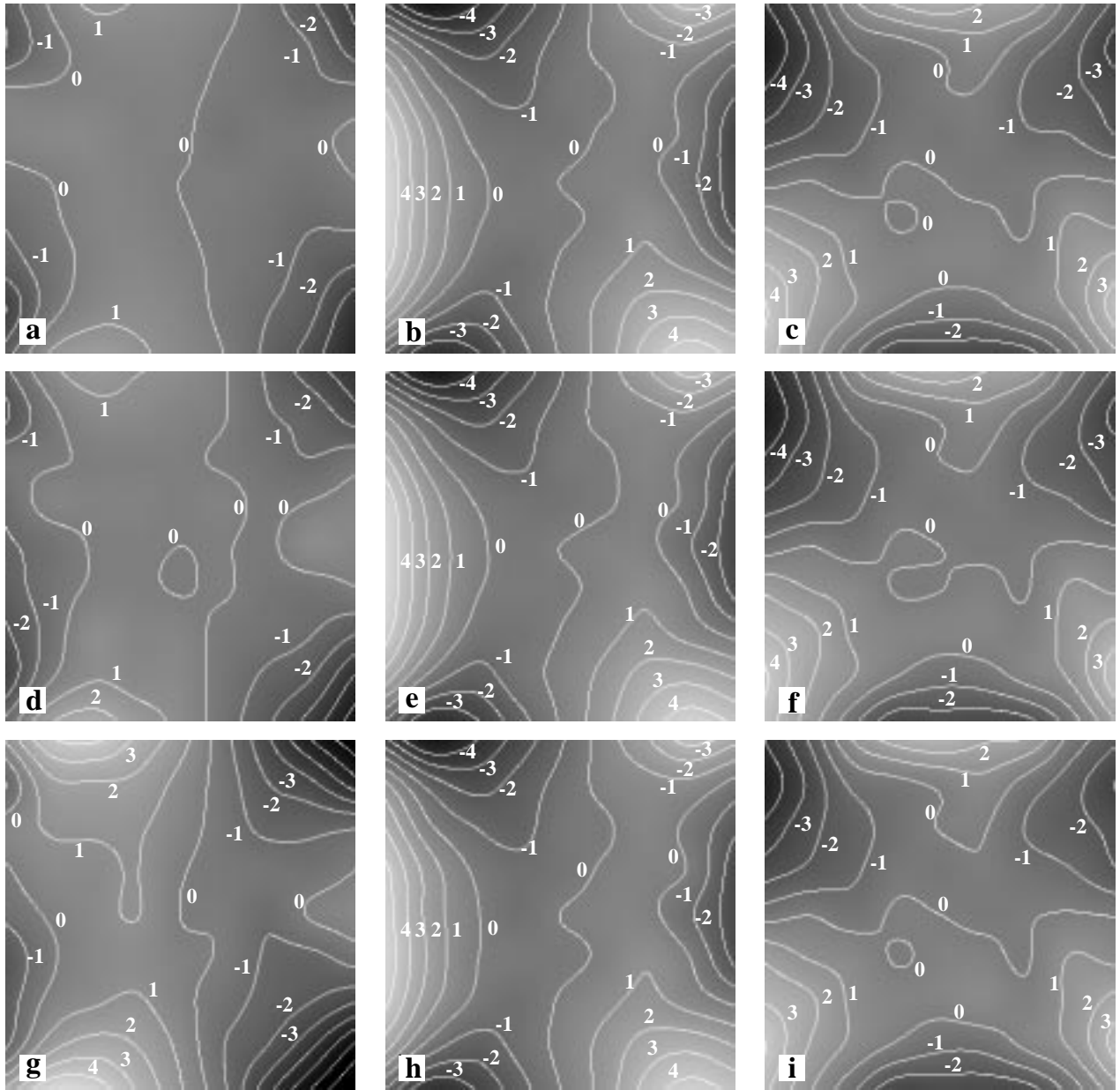


Figure 3.5: ΔB_0 (a,d,g), $\Delta B_{G_y}/G_y$ (b,e,h) and $\Delta B_{G_z}/G_z$ (c,f,i) in the central sagittal plane of the Gyroscan S15. The step size of the ΔB_0 contours is 1 ppm, the step size of the $\Delta B_{G_y}/G_y$ and the $\Delta B_{G_z}/G_z$ contours is 1 mm.

a,b,c) Single slice experiment, read-out gradient 1.21 mT/m

d,e,f) Single slice experiment, read-out gradient 2.94 mT/m

g,h,i) Multiple slice experiment, read-out gradient 2.94 mT/m.

Table 3.1: Static field inhomogeneity and non-linearity of the gradients of the Philips Gyroscan S15. The table gives negative and positive maximum values of the errors within a cubic volume.

volume (mm ³)	ΔB_0 (ppm)		$\Delta B_{G_x}/G_x$ (mm)		$\Delta B_{G_y}/G_y$ (mm)		$\Delta B_{G_z}/G_z$ (mm)	
168 ³	-5.3	3.5	-3.4	3.2	-2.6	2.2	-1.1	3.4
252 ³	-7.3	6.9	-6.0	6.3	-4.9	4.9	-2.5	4.9
336 ³	-11.1	9.4	-8.8	9.3	-7.2	9.7	-4.8	7.1

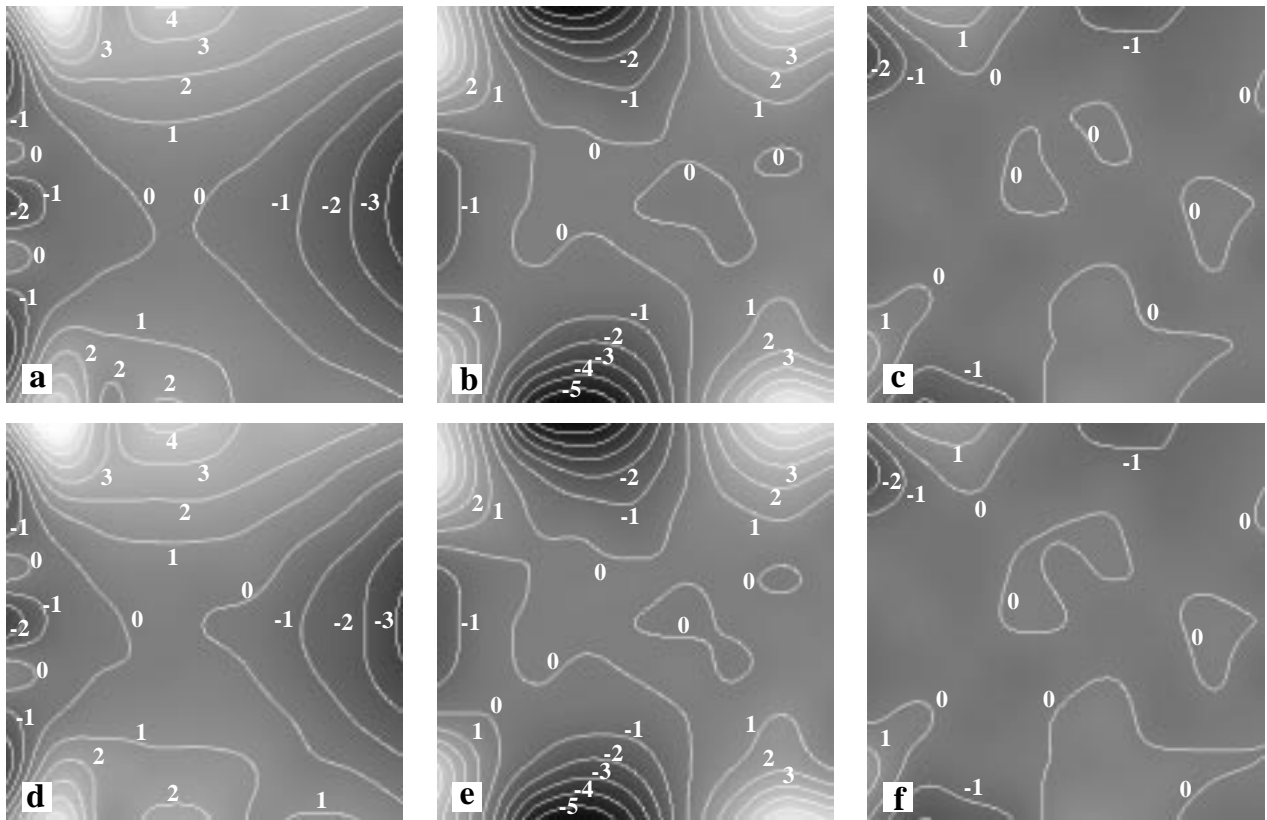
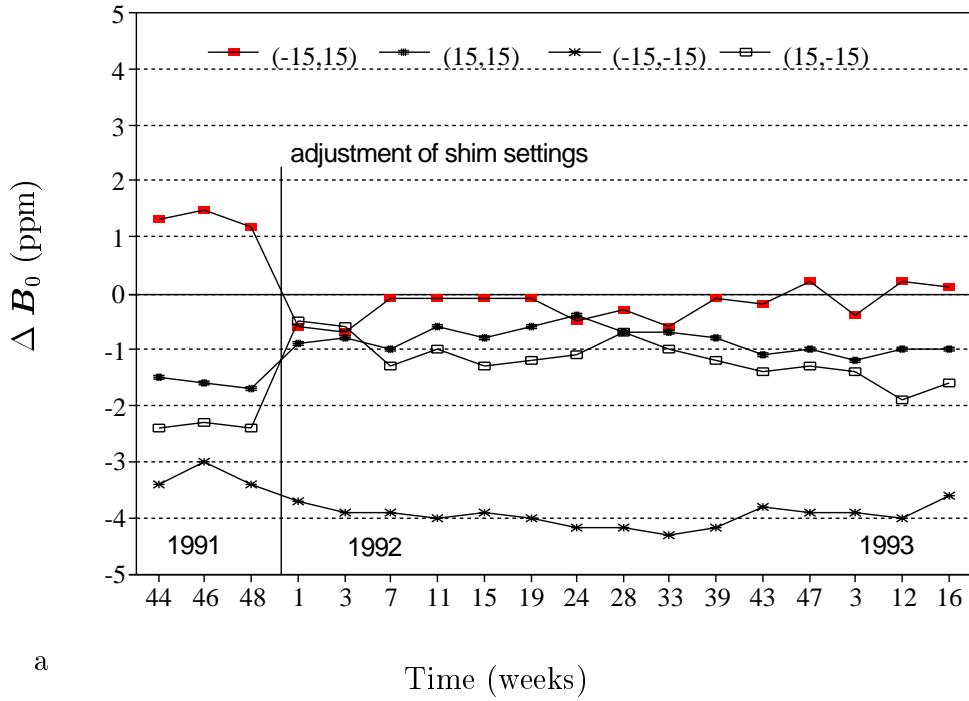


Figure 3.6: ΔB_0 (a and d), $\Delta B_{G_y}/G_y$ (b and e) and $\Delta B_{G_z}/G_z$ (c and f) in the central sagittal plane of the Gyroscan ACS-NT. The step size of the ΔB_0 contours is 1 ppm, the step size of the $\Delta B_{G_y}/G_y$ and the $\Delta B_{G_z}/G_z$ contours is 1 mm.

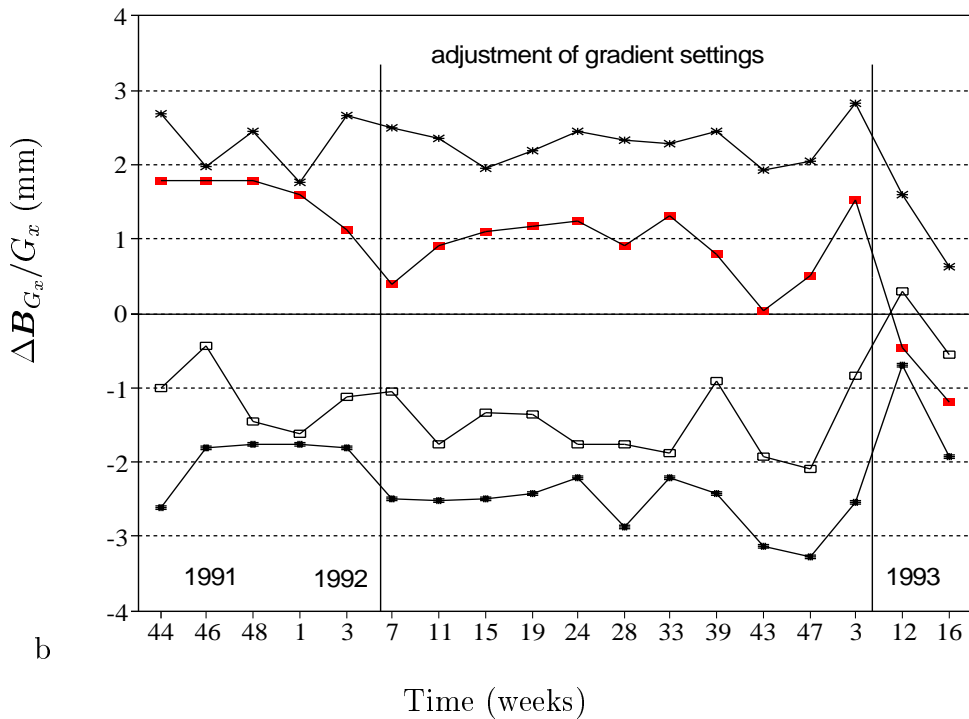
a,b,c) Single slice experiment, read-out gradient 1.15 mT/m
d,e,f) Multiple slice experiment, read-out gradient 3.47 mT/m.

slice transversal spin echo phantom images with interchanged directions of the read-out and phase-encoding gradients were acquired on the Gyroscan S15. 2D field error maps were determined in 11 transversal planes at z -coordinates between $z = -105$ mm and $z = 105$ mm with a step size of 21 mm. The field error maps were used for correction of one set of images. Figure 3.8 shows the distribution of the 2D distortions at the grid points of the 11 transversal planes before and after correction of the images. Application of the correction scheme reduced the distortions from maximally 13 mm to maximally 2 mm within a VOI of $336 \times 336 \times 210$ mm³ and from maximally 9 mm to maximally 1 mm within a VOI of $252 \times 252 \times 210$ mm³. The residual errors were on the order of the pixel resolution.

The efficacy of the correction scheme with respect to the correction of images of arbitrary objects was tested in a study on the Leksell frame. 2D field error maps were determined from phantom images in 9 sagittal planes at x -coordinates between $x = -84$ mm and $x = 84$ mm with a step size of 21 mm. The field error maps were used to correct a set of multiple slice images of the Leksell frame, which were acquired with a pulse sequence identical to the pulse sequence used in phantom imaging. The maximum slice and read-out gradients were chosen (3 mT/m at the Gyroscan S15) to minimize the susceptibility effects in the Perspex plates of the frame (chapter 4). Figure 3.9a gives a perspective view of the Z-shaped tubes in the posterior, cranial and anterior plate reconstructed from the sagittal MR images in relation to the real geometry of the frame. The distortions were largest for the tubes in the anterior plate. This plate was 40 mm closer to the borders of the magnet bore (the images were



a



b

Figure 3.7: Long term behaviour of static field (a) and gradient errors (b) in the central coronal plane at positions (-15,15), (15,15), (-15,-15) and (15,-15). The coordinates (x, z) are in cm.

Figure 3.8: Histogram of distortions at grid points for the Gyroscan S15 in multiple slice transversal images before and after correction for different volumes of interest. The distortions were reduced to about 1 mm in the corrected images, which was smaller than the pixel resolution of the images (1.48 mm).

acquired with 20 mm anterior offset). Figure 3.9b gives a perspective view of the frame after correction of the images in relation to the real geometry. Application of the 2D correction scheme reduced distortions from 6.4 mm to smaller than 1.5 mm.

3.5 Discussion

Several strategies may be adopted to correct for MR image distortions depending on the nature of the distortions. Ehricke and Schad 1992 found that distortion depends very much on the condition of the scanner, namely the state of shimming and eddy currents compensation. Their experiments showed that for a given scanner condition and acquisition protocol, the spatial distortion pattern is very stable. Therefore correction polynomials, which were calculated on the basis of a phantom study, can be used to correct patient data. Michiels et al. 1994 also found that the distortion pattern depends on the acquisition protocol, thus it is mandatory that the phantom image is measured by the same sequence and at the same

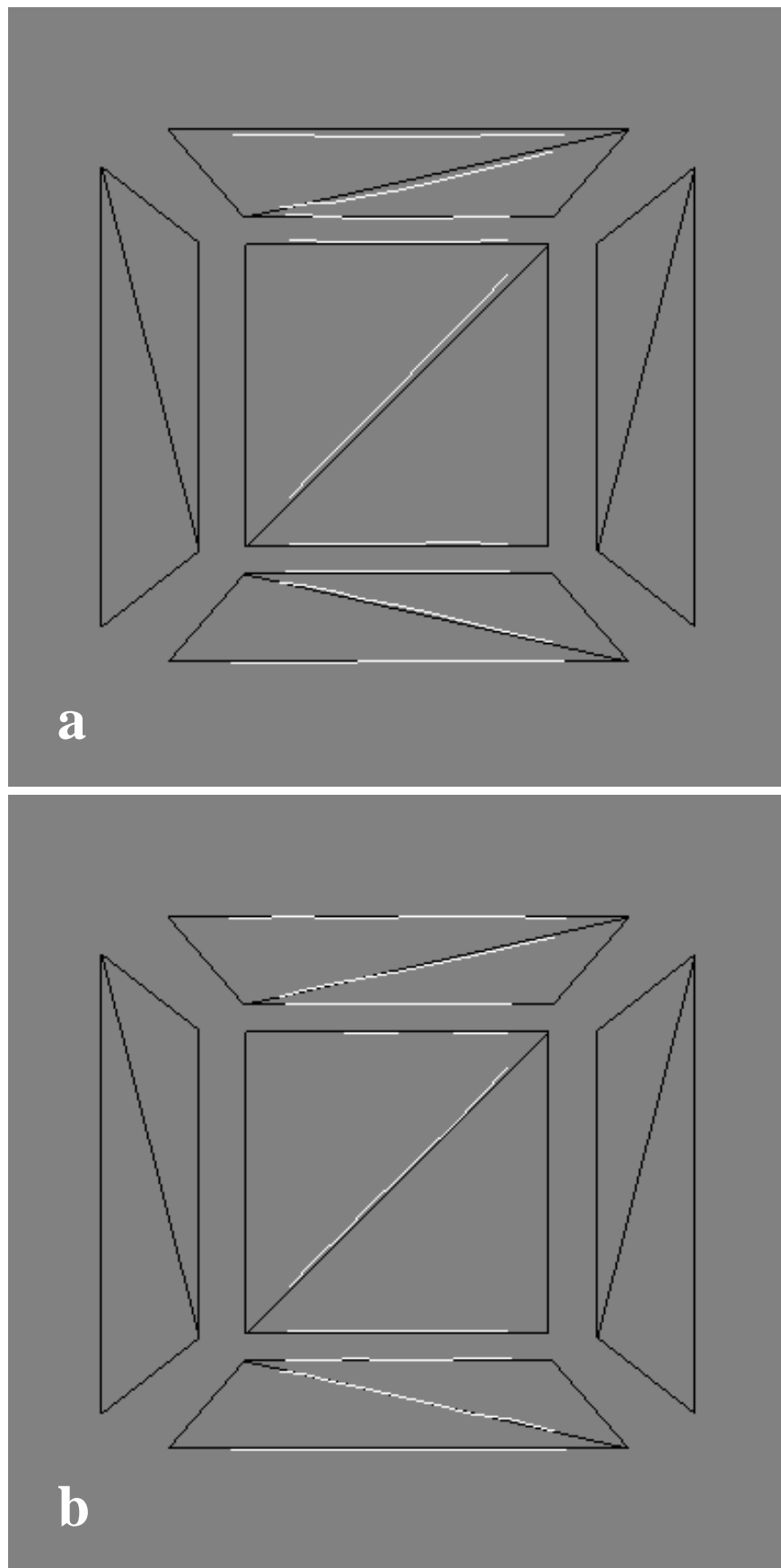


Figure 3.9: Perspective view of the Z-shaped tubes in the Leksellframe reconstructed from a) uncorrected and b) corrected MR images compared to the real geometry (black).

position as the patient image for the correction procedure to be valid. This approach may be very labour intensive and therefore not practical because of the variety of pulse sequences which are nowadays available. From our own studies we could conclude that on the new generation Philips NMR scanner (Gyrosan ACS-NT), the implementation of active shielding technology reduced the influence of eddy currents, which resulted in stability of static field inhomogeneity and non-linearity of the gradients. The static and gradient field errors were independent of pulse sequence parameters like single or multiple slice acquisition and gradient strengths and directions. Under these conditions we advocate a more general approach based on 3D static and gradient field error maps. These error maps can be used for correction of patient images, which may have been acquired with a pulse sequence, which is not necessarily identical to the pulse sequence applied for phantom imaging. The required frequency of the field error measurements depends on the long term behaviour of static field and gradient field errors. On the Gyrosan S15 we found that measurements once a year and whenever gradient settings had been adjusted, seemed sufficient. Thus far, we evaluated only correction of distortions in the image plane. In principle, the 3D static and gradient field error maps also allow pointwise rectification of distortion in the slice direction. A problem might be that in 2DFT MR the slices are not typically contiguous and hence undersampled in the slice direction (Sumanaweera et al. 1993). In 3DFT MR, the resolution in the slice direction is comparable to in-plane resolution in which case the 3D correction can be thought of as an extension of the 2D correction methods. Also distortions in oblique slices might be corrected, since the errors in oblique gradients are expected to be the vectorial sum of the errors in the orthogonal components of the oblique gradient.

3.6 Conclusions

Reviewing the results presented in the previous sections, the following conclusions with regard to the assessment and correction of machine dependent distortions in MR imaging can be drawn. Inhomogeneity of the static field and non-linearity of the gradients should be established by phantom experiments. A grid phantom of equally spaced tubes appears to be very suitable for this purpose. Interchanging the directions of the read out and the phase encoding gradients enabled decomposition of the image distortions into contributions from static field inhomogeneity and the non-linearity of the three gradients. A 3D map of static field inhomogeneity and non-linearity of the gradients is thus obtained from sagittal, coronal, and transversal multiple slice images with for each acquisition the phantom positioned such that the tubes are perpendicular to the image plane. Time series of measurements on the Gyrosan S15 showed field error stability within the experimental errors of ± 1 ppm for static field inhomogeneity and ± 1 mm for the gradient fields. Measurements on the Gyrosan ACS-NT, equipped with active shielding technology, showed field error stability under different imaging conditions. These observations imply that the measured error maps can be used for correction of patient images which may have been acquired with a pulse sequence that is not necessarily identical to the pulse sequence applied for phantom imaging. The correction procedure reduced distortions up to 13 mm within a VOI with dimensions $336 \times 336 \times 210$ mm³ to smaller than 2 mm. In a study on the Leksell frame distortions up to 6.4 mm were reduced to smaller than 1.5 mm. We conclude that MR image corrections are necessary in applications which require mm accuracy and that correction methods, based on 3D maps of static field inhomogeneity and gradient non-linearity, are feasible in clinical practice.

Chapter 4

Analysis of geometric distortions in MRI caused by patient related magnetic field inhomogeneity

This chapter includes parts of the following publications:

R. Bhagwandien, R. van Ee, R. Beersma, C.J.G. Bakker, M.A. Moerland, and J.J.W. Lagendijk. Numerical analysis of the magnetic field for arbitrary magnetic susceptibility distributions in 2D. *Magnetic Resonance Imaging*, 10: 299-313, 1992.

M.A. Moerland, R. Beersma, R. Bhagwandien, H.K. Wijrdeman, and C.J.G. Bakker. Analysis of object-related spatial distortions of external landmarks in 1.5 T MR head images. *The British Journal of Radiology*, accepted.

4.1 Introduction

Magnetic resonance imaging is known to be subject to distortions. In chapter 3 we analyzed the machine related image distortions and concluded that these distortions can be corrected by table lookup methods. However, due to object-induced distortions of the static magnetic field \mathbf{B}_0 , this approach will not generally produce the required accuracy when imaging arbitrary objects. This is clearly demonstrated by figure 4.1. By imaging external marker tubes in the presence (figure 4.1a) and in the absence (figure 4.1b) of the head, the object-induced distortions are directly visualized by a composite representation (figure 4.1c) of both images. These distortions are caused by the inhomogeneous susceptibility distribution (Lüdeke et al. 1985), in this case mainly by the difference in susceptibility between the head and the surrounding air. Susceptibility is the property which relates the magnetization of an object to the applied magnetic field. The presence of a patient in a MRI scanner leads to static magnetic field inhomogeneity, since the magnetic field is perturbed as the consequence of the difference in susceptibility between the patient and the surrounding air. The severity of the field perturbations outside the body depends on the susceptibility difference with air, the shape of the body and the orientation of the body with respect to the applied magnetic field (Cox et al. 1986; Young et al. 1987; Yamada et al. 1990; Yamada et al. 1992; Mosher and Smith 1991; Bhagwandien et al. 1994). For better understanding of the object-induced image distortions we developed a numerical technique for calculating the magnetic field for arbitrary magnetic susceptibility distributions. This calculation method was validated against analytical solutions for a cylinder and a coaxial cylinder (Bhagwandien et al. 1992a). In this chapter our numerical technique will be briefly reviewed and applied to a clinical setup, namely to calculate the magnetic field around the head fixed by a cast in a home-built localization frame. MR image distortions around the head may be significant, since some applications regarding this site require mm accuracy, e.g. stereotaxy (Schad et al. 1987a), stereotactic radiotherapy (Ehricke and Schad 1992; Kooy et al. 1994; Schad et al. 1994), stereotactic neurosurgery (Michiels et al. 1994) and radiotherapy treatment planning of brain tumours (Schad et al. 1987b). Furthermore, distortions as a result of magnetic field perturbations by external devices such as localization frames have not been fully explored yet. The aim of the work presented in this chapter is to measure the object-related image distortions around the head and in the localization frame and to analyze these distortions by means of numerical calculation of the magnetic field changes induced by the head and the frame.

4.2 Measurements of object-related image distortions around the head and in the localization frame

4.2.1 Materials

We studied the geometric distortions in and around the head fixed by a cast in a home-built localization frame. The head cast and the localization frame were both attached to the base plate, so that the object (patient or volunteer) could be positioned reproducibly (see figure 4.2). The five Perspex plates of the frame and the base form a box, open at the caudal end, with outer dimensions width * height * length = 30 cm * 27 cm * 27 cm. This set-up fits closely in the body coil of the MRI scanner and provides enough space for a person to be positioned with the head on a headrest, which is also used during radiotherapy. Plastic tubes

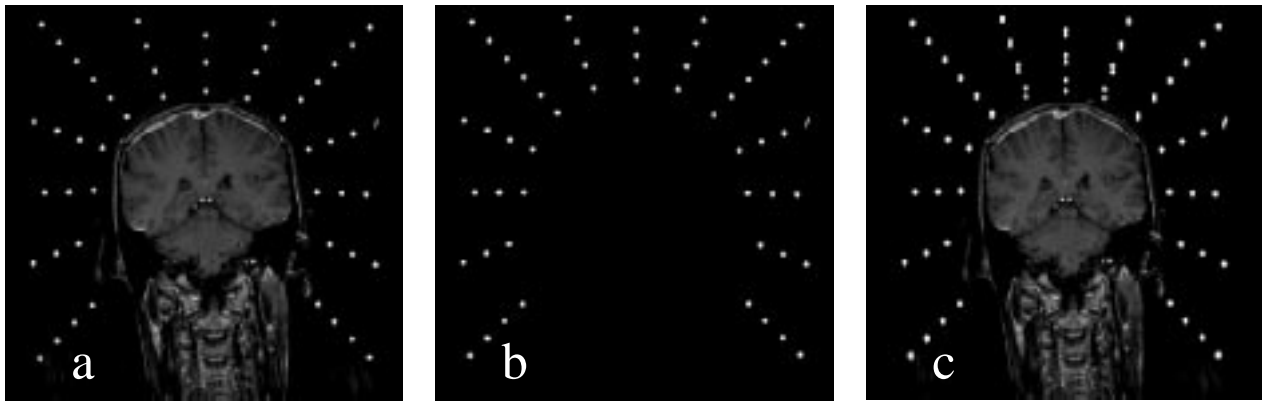


Figure 4.1: Coronal spin echo images ($TR = 500$ ms, $TE = 50$ ms) of a set of external markers in the presence (a) and the absence (b) of the disturbing influence of an object, namely, the human head. The images a and b were acquired with read-out gradient along the z -axis (read-out gradient $G_z = 1.02$ mT/m, $B_0 = 1.5$ T, FOV = 320 mm, acquisition matrix = $256 * 256$), the image c represents the composite of the images a and b.

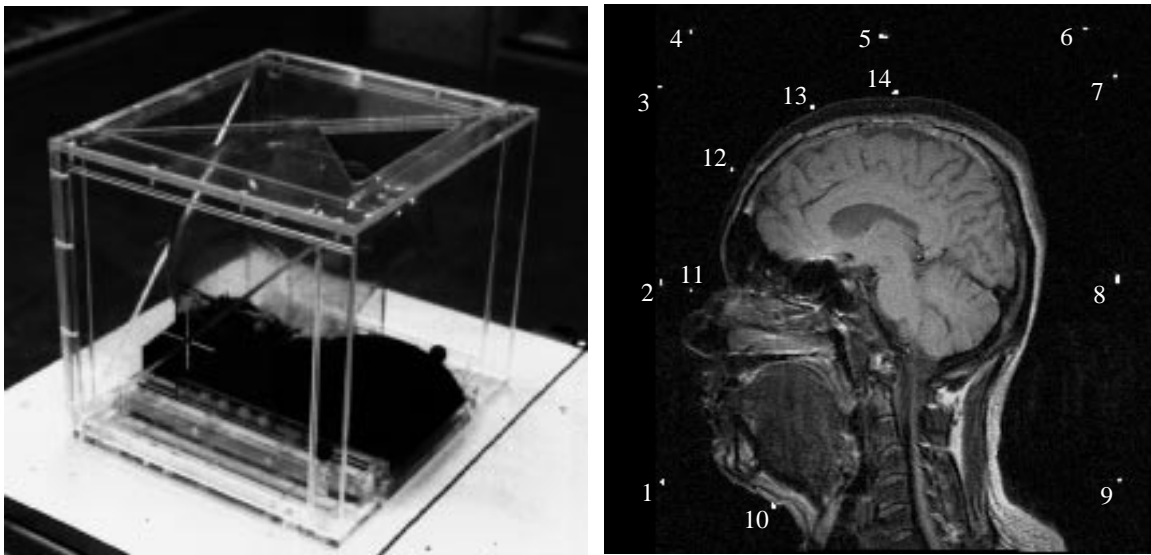


Figure 4.2: The localization frame with headcast and headrest (left). A midsagittal MR image of the head with the external markers indicated (right).

with an inner diameter of 2 mm, filled with doped water (770 mg $\text{CuSO}_4 \cdot 5\text{H}_2\text{O}/\text{l}$), were set in a Z-shape in grooves milled in the Perspex plates. Together with five tubes attached to the headcast at different locations in the midsagittal plane they served as external markers (see figure 4.2). The markers in the localization frame were numbered 1 to 9 and the markers attached to the cast were numbered 10 to 14.

4.2.2 Imaging experiments

A healthy volunteer underwent MR scanning in the radiotherapy position on a flat table top with the head fixed by a plastic cast in the home-built localization frame. Imaging experiments were performed on a 1.5 T whole body MRI system with 3 mT/m maximum gradient capability (Gyrosan S15, Philips Medical Systems, Best, The Netherlands). The pulse sequences were conventional T_1 -weighted spin echo sequences. Relevant parameters included $TR \approx 900$ ms, $TE = 30$ ms, NEX = 2, matrix = $256 * 256$, single midsagittal

slice, slice thickness = 5 mm, FOV = 320 mm, body coil, magnitude reconstruction. Images were acquired with opposite directions of relatively weak read-out gradients (0.68 mT/m) for experimental analysis of object-related image distortions. Since field inhomogeneity results in spatial distortions in the direction of the read-out gradient, the true position (apart from distortions caused by gradient errors) of an image structure is half-way between the two distorted positions in both images (Chang and Fitzpatrick 1992).

4.2.3 Image processing

The images, which were acquired with opposite directions of the read-out gradient, were corrected for geometric distortions caused by machine imperfections using the method as described in chapter 3. The remaining image distortions, being the susceptibility-induced distortions and the chemical shift effects were determined by comparing image coordinates of corresponding structures in both images. Corresponding structures may be external markers, body contours or internal contours. Body contours were determined automatically using edge detection modules from the Application Visualization System (AVS) software package (Advanced Visual Systems Inc., USA). The image coordinates of the external markers were determined using an algorithm which calculates the centre of gravity of signal intensities within an interactively positioned square of pixels. Since the true position of an image structure is half-way between the two positions in both images, the distortion is half the difference of the two image coordinates of a structure. In the following a spatial distortion is defined as the distance between the true position and the distorted position and a displacement is defined as the distance between two positions in images acquired with opposite directions of the read-out gradient.

4.2.4 Results

Outer contours

Figure 4.3 shows two midsagittal spin echo images, which were acquired with opposite directions of the read-out gradient and corrected for machine imperfections, so that the susceptibility-induced distortions and chemical shift effects are the remaining error sources. The third image in figure 4.3 is the difference between the two MR images illustrated by means of contours. For the sake of clearness the internal contours were eliminated in figure 4.3. The difference image illustrates that the most cranial part of the outer contour of the head is influenced by the reversal of the gradient, which may be attributed to the chemical shift of the subcutaneous fat. In this area susceptibility-induced distortions could be neglected as was verified by numerical analysis of the magnetic field (see section 4.3). In the positive gradient image the subcutaneous fat is shifted 7 mm in the cranio-caudal direction leaving the outer contour undisturbed. In the negative gradient image the subcutaneous fat is shifted 7 mm in the caudo-cranial direction resulting in an overprojection of the subcutaneous fat and the skin, which leads to errors in automatic contour detection. In the 1.5 T MR images acquired with a negative read-out gradient of 0.68 mT/m the most cranial part of the head contour shows spatial distortions up to 4 mm. Larger distortions of the outer contour occurred in the neck region. The posterior neck contour in figure 4.3 showed a complicated pattern of distortions up to -12 mm in the positive gradient image and up to 12 mm in the negative gradient image, which was significantly larger than the chemical shift effect of 7 mm in these images. The remaining distortion of 5 mm could be attributed to susceptibility-induced distortions as was verified by numerical analysis (see

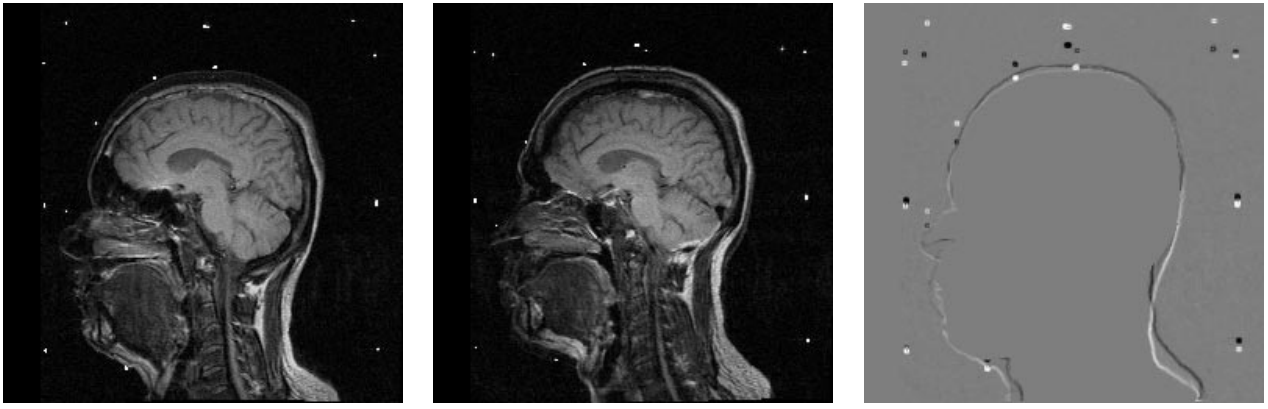


Figure 4.3: Distortion of outer contours and external markers. The two midsagittal spin echo images were acquired with opposite read-out gradients and corrected for distortions caused by machine imperfections (read-out gradient $G_z = 0.68$ mT/m and -0.68 mT/m along the caudo-cranial direction, $B_0 = 1.5$ T, FOV = 320 mm, grid size = $256 * 256$ pixels), the third image is the difference between the two MR-images illustrated by means of contours.

section 4.3). The outer contours at the mouth and nose region were severely degraded by susceptibility-induced geometry and intensity distortions. In these regions the outer contour was hard to recognise.

Internal contours

Susceptibility-induced distortions may be expected at interfaces between tissues with large differences in susceptibility. These differences exist between brain tissue and air in the cavities. Figure 4.3 clearly illustrates different shapes of the sinus frontalis and the sinus sphenoidalis in the positive and negative gradient images indicating that the air cavities were severely distorted in 1.5 T MR images acquired with a read-out gradient strength of 0.68 mT/m. These shape deformations can be quantified for particular points, e.g. a point at the interface between the sinus sphenoidalis and the brain tissue anterior to the pituitary gland. The positive and negative gradient images revealed a displacement of this point of 12.6 mm, the spatial distortion in the positive gradient image amounted 6.3 mm in the caudo-cranial direction.

Localization frame

Susceptibility-induced distortions of the markers 1 to 9 in the localization frame (see figure 4.2) were also determined from the positive and negative gradient images, which were only corrected for the machine imperfections. Taking into account the field of view (320 mm) and the offset (60 mm anterior) of these sagittal images, the image coordinates of the external markers were converted into world coordinates in mm. The observed coordinates of the external markers are shown in table 4.1. Coordinates in the positive and negative gradient images were denoted (y_1, z_1) and (y_2, z_2) respectively. The results indicated distortions in the direction of the read-out gradient (along the z -axis) as expected. The coordinates y_1 were equal to the coordinates y_2 , since magnetic field inhomogeneity does not lead to distortions in the direction of the phase-encoding gradient: $y_1 - y_2 = -0.3 \pm 1$ mm (mean \pm standard deviation). The standard deviation of the displacement $z_1 - z_2$ was estimated to be as small as the standard deviation of the difference $y_1 - y_2$, so that the susceptibility-induced marker

Table 4.1: Observed marker locations in positive (y_1, z_1) and negative gradient SE images (y_2, z_2), which were only corrected for machine imperfections. Phase-encoding was chosen along y (postero-anterior) and read-out along z (caudo-cranial) and $-z$ ($G_z=0.68$ mT/m). The last column gives the susceptibility-induced marker distortions in the positive gradient image determined as $(z_1 - z_2)/2$.

marker	y_1 (mm)	z_1 (mm)	y_2 (mm)	z_2 (mm)	$\Delta B_0/G_z$ (mm)
1	186.5	-117.3	186.6	-114.9	-1.2 ± 0.5
2	187.3	-1.5	187.1	3.5	-2.5 ± 0.5
3	188.5	112.3	187.3	121.5	-4.6 ± 0.5
4	170.0	145.0	172.5	119.5	12.8 ± 0.5
5	57.5	141.5	57.5	126.6	7.4 ± 0.5
6	-59.0	146.4	-58.8	123.8	11.3 ± 0.5
7	-77.0	118.6	-77.0	121.5	-1.4 ± 0.5
8	-77.9	0.1	-77.9	6.0	-2.9 ± 0.5
9	-79.5	-116.3	-79.5	-109.0	-3.7 ± 0.5
10	120.0	-129.8	122.6	-124.6	-2.6 ± 0.5
11	170.0	-5.2	169.9	-17.4	6.1 ± 0.5
12	146.3	63.9	145.9	48.9	7.5 ± 0.5
13	99.6	101.0	99.8	111.5	-5.3 ± 0.5
14	50.2	109.0	50.2	122.6	-6.8 ± 0.5

distortion was determined with a standard deviation of 0.5 mm (see the last column of table 4.1). The markers 4 to 6 in the localization frame showed the largest distortions ranging from 7.4 to 12.8 mm in the positive gradient image. The markers 1 to 3 and 7 to 9 showed distortions ranging from -4.6 to -1.2 mm. The different behaviour of the markers 4 to 6 compared to the markers 1 to 3 and 7 to 9 was also analyzed by means of the numerical method to calculate the magnetic field perturbations (see section 4.3).

Markers on the head

Spatial distortions of the markers 10 to 14 on the head ranged from -6.8 to 7.5 mm. The amplitude and sign of the marker distortion depended strongly on the position of the marker with respect to the head. In the positive gradient image, marker 12 on the forehead shifted 7.5 mm in the cranial direction, whereas marker 14 on top of the head shifted 6.8 mm in the caudal direction. These observations were also investigated by means of numerical analysis (see section 4.3).

4.3 Numerical analysis of the magnetic field for arbitrary susceptibility distributions: application to the head

4.3.1 Theory

For a magnetostatic problem the Maxwell equations reduce to the Laplace equation (Bhagwandien et al. 1992a)

$$\nabla \cdot (\mu \nabla \Phi_M) = 0. \quad (4.1)$$

The μ is the magnetic permeability (dimensionless) ($\mu = 1 + \chi$), χ the magnetic susceptibility (dimensionless) and Φ_M the magnetic scalar potential [Wb/m]. For a given μ -distribution, Φ_M is determined by (numerically) solving eq. 4.1. With $\mathbf{H} = -\nabla \Phi_M$ (\mathbf{H} the magnetic field [A/m]), the induced magnetic field \mathbf{B} [T] is calculated as $\mathbf{B} = \mu_0 \mu \mathbf{H}$ (μ_0 is the magnetic permeability in vacuum, $\mu_0 = 4\pi \cdot 10^{-7}$ H/m). The solution of eq. 4.1 results in the macroscopic induced magnetic field, which differs from the induced magnetic field experienced by the nucleus. In magnetic resonance imaging, the induced magnetic field experienced by the nucleus determines the resonant frequency and thus its spatial encoding. In the following, the induced magnetic field experienced by the nucleus is derived by adding the Lorentz correction ($-\frac{2}{3}\mu_0\chi\mathbf{H}$) to the calculated macroscopic induced magnetic field (Chu et al. 1990; Van Ee 1992).

4.3.2 Numerical solution

The calculation of the magnetic field for arbitrary geometries is based on the numerical solution of eq. 4.1. This equation is solved with a finite difference technique by transforming it into a diffusion equation with the introduction of an iteration coordinate τ (a pseudo time). The stationary state of the diffusion equation is then the magnetic scalar potential (Φ_M) distribution (Bhagwandien et al. 1992a). This means that the general definition of convergence of such a process has the form

$$C \frac{d\Phi_M}{d\tau} = \nabla \cdot (\mu(x, y, z) \nabla \Phi_M(x, y, z; \tau)) \quad (4.2)$$

where

$$\lim_{\tau \rightarrow \infty} \Phi_M(x, y, z; \tau) = \Phi_M(x, y, z). \quad (4.3)$$

C is a constant and the dimension of $C/d\tau$ is $[m^{-2}]$. The standard Fourier implementation scheme involves two iteration coordinate levels at coordinate τ and coordinate $\tau + d\tau$ for node (0). For a rectangular grid this gives for every node:

$$\Phi_M(0; \tau + d\tau) - \Phi_M(0; \tau) = \sum_{i=1}^6 B(i) \cdot \Phi_M(i; \tau) + B(7) \cdot \Phi_M(0; \tau), \quad (4.4)$$

with the summation over the six neighbouring nodes. The coefficients $B(1)$ to $B(7)$ are dimensionless. They are related to the magnetic permeability as follows:

$$B(i) = \frac{2\mu(i) \cdot \mu(0)}{\mu(i) + \mu(0)} \cdot \frac{d\tau}{C(dx)^2}, \quad (i = 1 \text{ to } 6) \quad (4.5)$$

$$B(7) = -\sum_{i=1}^6 B(i).$$

$B(i)$ represents the effective permeability between two nodes, assuming that each elementary node contains only one type of material (the permeability $\mu(i)$). This two iteration coordinate level scheme is known to be unstable when the iteration coordinate step $d\tau$ exceeds the maximal permissible iteration coordinate step (Bhagwandien et al. 1992a).

Modifying this iteration scheme with the Du Fort-Frankle algorithm (Mitchell and Griffiths 1980), the explicit finite difference scheme involving three coordinate levels for node (0) is given by

$$\Phi_M(0; \tau + d\tau) = \sum_{i=1}^6 D(i) \cdot \Phi_M(i; \tau) + D(7) \cdot \Phi_M(0; \tau - d\tau). \quad (4.6)$$

The coefficients $D(i)$ are calculated from the coefficients $B(i)$ from eq. (4.5):

$$\begin{aligned} D(i) &= \frac{2 \cdot B(i)}{2 - B(7)} \quad (\text{for } i = 1 \text{ to } 6), \\ D(7) &= \frac{2 + B(7)}{2 - B(7)}. \end{aligned} \quad (4.7)$$

Note that the Φ_M at the new iteration coordinate step $\tau + d\tau$ is calculated with the Φ_M at iteration coordinate step τ and iteration coordinate step $\tau - d\tau$. This scheme is unconditionally stable for an arbitrary iteration coordinate step $d\tau$ and thus $d\tau$ may be increased.

4.3.3 Implementation

The boundaries are the fixed top and bottom boundaries. For the numerical implementation the object is assumed to be placed in an area such that the field distortions from the object do not influence the field at the boundaries of the area. This means that the magnetic field is homogeneous at a large distance from the object. The other four boundaries (left, right, front and back) are chosen such that no Φ_M gradient exists across the boundaries.

The procedure for calculating the magnetic field is divided into two steps. This is schematically shown in figure 4.4. In the first step (figure 4.4a) the calculation is performed at a low resolution scale (e.g. 4 mm/pixel). Φ_M is iteratively calculated until the stationary solution is achieved. The new boundaries, closer to the object, can be copied for the second step (figure 4.4b). The calculation is performed again, but now with the new boundaries and full resolution (e.g. 1 mm/pixel).

The field calculation of the magnetic scalar potential is done in double precision, which results in an accuracy better than one part per million. The numerical calculations for a cylinder model compared with the analytical solutions showed that the accuracy of the simulations was on the order of 0.3 ppm (Bhagwandien et al. 1992a).

4.3.4 Materials

The numerical method was applied to study the geometric distortions in and around the head fixed by a cast in the home-built localization frame (see figure 4.2). The susceptibility distribution was determined from a midsagittal MR head image of a healthy volunteer. This image was acquired with a maximum read-out gradient (2.9 mT/m) to reduce geometric distortions caused by magnetic field inhomogeneity and was corrected for in-plane distortions caused by machine imperfections to derive as accurately as possible the object geometry for numerical analysis. The image was converted into a susceptibility distribution by manual

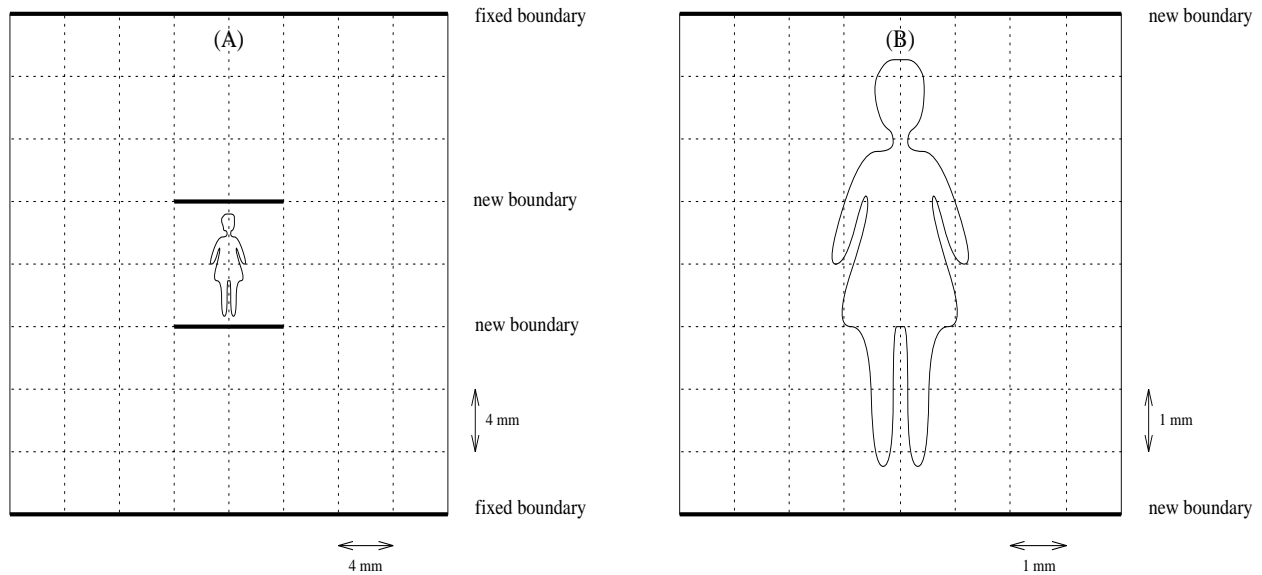


Figure 4.4: A schematic overview of the main steps in calculating the Φ_M -distribution. (a) In the first step the calculation is performed in a low resolution scale, where the boundaries are at large distance from the object. The Φ_M is iteratively calculated until the stationary solution is achieved. (b) In the second step the calculation is performed again, but now with the new boundaries closer to the object (copied from the first step) and full resolution.

contouring of water-equivalent tissue (soft tissues and bone, $\chi = -9 \times 10^{-6}$) and air ($\chi = 0$) (Sumanaweera et al. 1993; Weast and Astle 1980). This is a fair approximation, since significant susceptibility inhomogeneities only occur at tissue-air interfaces. Soft tissues, blood and bone show susceptibilities ranging from -7.5 to -10×10^{-6} (Bhagwandien 1994; Sumanaweera et al. 1993; Weast and Astle 1980; Weisskoff and Kiihne 1992). The Perspex frame, not visible in an MR image, was included in the susceptibility distribution guided by the location of the tubes (figure 4.2). Since the susceptibility of Perspex was not found in the literature, we performed an experiment as described by Lüdeke et al. 1985 and Sumanaweera et al. 1993. The susceptibility of Perspex was determined from reversed read-out gradient experiments on a coaxial cylinder with a Perspex inner region and the annular region filled with water. In these spin echo and gradient echo images the read-out gradient was chosen minimal ($G = 0.85$ mT/m) to obtain maximal sensitivity for visualisation of susceptibility-induced image distortions. Nevertheless, the images showed no susceptibility artifacts, from which we could conclude that the susceptibility of Perspex is equal to that of water: $\chi_{\text{Perspex}} = -9 \times 10^{-6}$. Figure 4.5 shows the segmented 2D susceptibility distribution of the head in the localization frame, for which the magnetic field was calculated.

4.3.5 Results

The magnetic field in and around the head was calculated in the midsagittal plane in 2D. Figure 4.5 shows the segmented susceptibility distribution and the resulting magnetic field perturbations in steps of 0.5 ppm. High image intensities depict field strengths larger than the applied magnetic field of 1.5 T, low intensities depict field strengths smaller than 1.5 T.

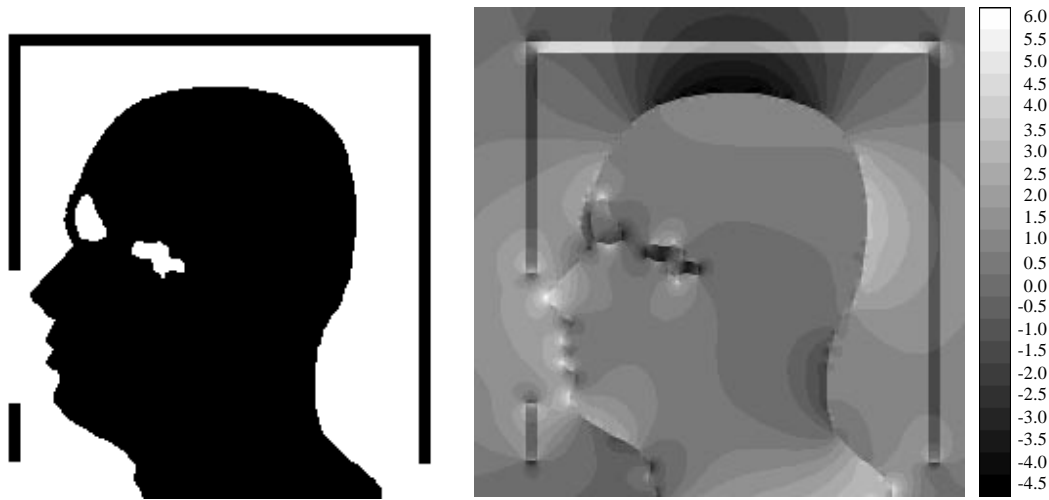


Figure 4.5: Segmented susceptibility distribution (left) and simulated \mathbf{B} -field (right), $B_0 = 1.5$ T, FOV = 320 mm, grid size = $256 * 256$ pixels. The perturbations are shown by means of shades with a step size of 0.5 ppm. Light shades indicate a stronger field, dark shades indicate a weaker field than the 1.5 T magnetic field, applied in the caudo-cranial direction. The objects were segmented into soft tissues, bone and Perspex, $\chi = -9 \times 10^{-6}$ and air, $\chi = 0$. Note the variation in magnetic field perturbation with the orientation of the Perspex plates.

Outer contour

Except for regions with air-tissue interfaces (around the air cavities) or irregular contours (nose and chin) the \mathbf{B} -field inside the skull varies only slightly. Going along the contour of the skull the field perturbations inside the skull vary from 0.8 ppm frontal to 1.2 ppm cranial to 0.6 ppm occipital and the average value of the magnetic field inside the skull is about 0.6 ppm above the applied 1.5 T. As a result the outer contour of the head was hardly distorted (see figure 4.3). In 1.5 T images acquired with a read-out gradient strength of 0.68 mT/m, the 0.6 ppm magnetic field deviation in the skull resulted in contour distortions not exceeding 1.5 mm. The observed contour distortions at the top of the head in figure 4.3 were due to chemical shift of the subcutaneous fat with respect to the other tissues (see section 4.2.4). In the neck area both susceptibility-induced field perturbations and chemical shift of the subcutaneous fat contributed to the observed contour distortions. In the neck posterior, the susceptibility-induced field perturbations ranged from -2 to 3 ppm and the chemical shift of subcutaneous fat resulted in a field perturbation of -3.2 ppm. As a result the neck contour showed a complicated pattern of distortions ranging from -12 to 0 mm in the positive gradient image acquired with a read-out gradient strength of 0.68 mT/m. The irregular contours at the mouth and nose region led to magnetic field perturbations ranging from -1 to 5 ppm resulting in severe geometry and intensity distortions. In these regions the outer contour was hard to recognise (see figure 4.3).

Internal contours

According to the simulations, the tissue-air interfaces at the sinus sphenoidalis and the sinus frontalis resulted in an irregular magnetic field distribution. Field perturbations at the cranio-caudal tissue-air interfaces were positive and ranged from 0 to 4 ppm, whereas perturbations at the antero-posterior interfaces were negative and ranged from 0 to -4 ppm. In 1.5 T images acquired with a read-out gradient strength of 0.68 mT/m these field perturbations resulted in spatial distortions of points at the interface between -9 and 9 mm. For

a point at the cranio-caudal interface between the sinus sphenoidalis and the brain tissue anterior to the pituitary gland, a spatial distortion of 6.3 mm was measured in the positive gradient image (see section 4.2.4). This was in good agreement with the simulations.

Localization frame

Calculation of the magnetic field revealed that the field strength in the frame was dependent on the orientation of the plates with respect to the main magnetic field (see figure 4.5). The field strength inside the posterior and anterior plates, which were parallel to the magnetic field, was 2.8 parts per million (ppm) smaller than the field strength outside. The field strength inside the cranial plate, which was perpendicular to the magnetic field, was 5.8 ppm larger than the field strength outside. The field strength in the plates was also influenced by the field perturbation by the head. For 1.5 T images acquired with a read-out gradient strength of 0.68 mT/m, the simulations predicted spatial distortions ranging from -5 to -1 mm for the markers in the posterior and anterior plates and from 6 to 11 mm for the markers in the cranial plate. In previous work we estimated the accuracy of the simulations to be on the order of 0.3 ppm or 0.7 mm in 1.5 T images acquired with a read-out gradient strength of 0.68 mT/m (Bhagwandien et al. 1992a). The simulations showed a pattern of spatial distortions of the markers comparable to that of the measurements (see Table 4.2). The largest deviations between simulations and measurements occurred for landmarks 4 (-2.7 mm) and 7 (3.0 mm). This may be explained by errors in the calculation of the susceptibility-induced magnetic field perturbations, since the magnetic field was calculated in 2D instead of 3D. Errors caused by inaccuracies in assessment of the object geometry, which was derived from a distorted image, may be neglected. In a study on ten patients we found systematic spatial distortions of the external landmarks with a standard deviation of 0.5 mm, indicating that the magnetic field perturbations are insensitive to relatively small deviations in object geometry (see chapter 6).

Markers on the head

Calculation of the magnetic field in and around the head predicted largest perturbations outside the head at the interface between the head and the surrounding air. The magnetic field resembled a dipole field in the midsagittal plane of calculation with a larger field strength anterior and posterior to the head and a smaller field strength cranial to the head than the applied 1.5 T magnetic field. Magnetic field perturbations ranged from -4 ppm on top of the head to 2 ppm at the forehead. On the “diagonals”, the magnetic field perturbations were close to zero (figure 4.5). If a tube on the cast may be regarded as an infinitely long cylinder with its axis perpendicular to \mathbf{B}_0 the tube experiences an additional magnetic field perturbation, given by:

$$\mathbf{B}_i \approx \mathbf{B}_0 \left(1 - \frac{\chi_i}{6}\right), \quad (4.8)$$

where \mathbf{B}_i is the internal magnetic field, χ_i is the susceptibility of the tube ($\chi_i = -9$ ppm) and the Lorentz correction has been taken into account (Chu et al. 1990; Van Ee 1992; Bhagwandien 1994). Thus, the marker experiences the sum of the magnetic field perturbation induced by the head and the 1.5 ppm magnetic field perturbation induced by the marker itself. For 1.5 T images acquired with a read-out gradient strength of 0.68 mT/m and taking into account the 1.5 ppm marker-induced field perturbation, the field simulations predicted spatial marker distortions ranging from -6 mm on top of the head to 8 mm at the forehead. The accuracy of the simulated marker distortions was determined by the accuracy of the

Table 4.2: Spatial distortions of external markers on the headcast and in the localization frame in a midsagittal 1.5 T MR image according to measurements and simulations (read-out gradient $G_z = 0.68$ mT/m).

marker	$\Delta z_{meas.}$ (mm)	$\Delta z_{sim.}$ (mm)
1	-1.2 ± 0.5	-1.8 ± 0.7
2	-2.5 ± 0.5	-0.9 ± 0.7
3	-4.6 ± 0.5	-4.9 ± 0.7
4	12.8 ± 0.5	10.1 ± 0.7
5	7.4 ± 0.5	6.2 ± 0.7
6	11.3 ± 0.5	11.0 ± 0.7
7	-1.4 ± 0.5	-4.4 ± 0.7
8	-2.9 ± 0.5	-1.8 ± 0.7
9	-3.7 ± 0.5	-3.1 ± 0.7
10	-2.6 ± 0.5	0.7 ± 1.1
11	6.1 ± 0.5	6.2 ± 1.1
12	7.5 ± 0.5	7.7 ± 1.1
13	-5.3 ± 0.5	-4.4 ± 1.1
14	-6.8 ± 0.5	-6.0 ± 1.1

field calculations (0.3 ppm) and the accuracy of positioning the markers in the calculated field distribution, which was estimated to be 0.2 ppm. The total accuracy in determination of the field perturbation at the positions of the markers 10 to 14 was thus 0.5 ppm or 1.1 mm in 1.5 T images acquired with a read-out gradient strength of 0.68 mT/m. The simulations were in good agreement with the observed spatial distortions of the markers on the head. An exception is landmark 10, of which the simulated distortion deviated about 3 mm from the measured value (see table 4.2). This may be explained by errors in the calculation of the susceptibility-induced magnetic field perturbations, since the magnetic field was calculated in 2D for a midsagittal slice of the head and neck region instead of the 3D total body.

4.4 Discussion

In this study of 1.5 T midsagittal MR head images only in-plane distortions were assessed. Images were corrected for machine-related magnetic field inhomogeneity and non-linearity of the read-out and phase-encoding gradient. Slice warp caused by magnetic field inhomogeneity and non-linearity of the slice selection gradient, was not corrected. The maximum slice selection gradient was chosen to reduce slice warp caused by magnetic field inhomogeneity. Slice warp caused by non-linearity of the slice selection gradient may have led to inaccuracies in assessment of object geometry. However, the influence of this on the calculation of the magnetic field perturbation may be neglected. After correction for machine-related in-plane image distortions, the internal and external contours and the external markers still exhibited distortions, for the latter ranging from -6.8 mm to 12.8 mm. From the numerical analysis, it was concluded that these residual distortions could be attributed to magnetic field perturbations by the head and the localization frame. Several authors have addressed the problem of correcting object induced geometric distortions in MRI. Chang and Fitzpatrick 1992 presented a method which requires the acquisition of two images of the same

object with altered gradients, from which the correct image can be calculated. The efficacy of the technique was proven for phantom experiments. Bakker et al. 1992 adapted the method for the correction of patient images, the results of which were not yet satisfying. Cho et al. 1988 and Cho and Ro 1992 proposed inhomogeneity correction methods, which require modification of the pulse sequences and are therefore not readily available in a clinical environment. In previous work (Bhagwandien 1994) we developed a method based on just one image, the distorted MR image. The main steps in this method are the conversion of the MR image into a magnetic susceptibility distribution by segmenting the image into air and water equivalent tissue, the calculation of the \mathbf{B} -field and the calculation of the corrected MR image by applying a reversed read-out gradient. A disadvantage of the method is that these steps take a few hours computing time for correction of one image on a *Silicon Graphics Workstation* with an R4000 processor. All together, correction methods are not yet readily available in a clinical environment and therefore it seems more practical to adapt imaging protocols, which reduce object-induced geometric distortions to acceptable values. Since susceptibility-induced field inhomogeneity $\Delta\mathbf{B}_0$ is proportional to the applied field \mathbf{B}_0 and since the corresponding geometric distortions are inversely proportional to the read-out gradient strength, object-induced geometric distortions can be reduced by imaging at a low magnetic field (e.g. 0.5 T instead of 1.5 T) and choosing relatively large gradient strengths. We have described object-induced geometric distortions in 1.5 T head images acquired with a read-out gradient strength of 0.68 mT/m. The largest distortion occurred for a marker in the localization frame and amounted 12.8 mm. This maximum distortion can be reduced to 1 mm, which in general is smaller than the pixel size, by imaging at 0.5 T and using gradient strengths ≥ 3 mT/m. At 1.5 T, the gradients should be 9 mT/m. Nowadays, on most commercial MRI scanners these gradient strengths are readily available. A drawback of using large gradients is the concurrent decrease of signal to noise ratio of the MR image. Thus, the improved geometric accuracy may result in a decreased diagnostic quality of the MR image. In clinical practice the read-out gradient is usually operated to about 3 mT/m. To our opinion, with the state of the art 0.5 T MRI scanners it is possible to derive images acquired with gradient strengths on the order of 3 mT/m of adequate diagnostic quality for radiotherapy treatment planning purposes. Thus, if the geometric distortions caused by magnetic field inhomogeneity can be reduced to smaller than the pixel size, the gradient non-linearity is the remaining significant source of image distortions to be corrected.

Thus far, we described patient-related image distortions in the head region. The question may arise whether significant distortions occur at other body sites. Figure 4.6 shows the magnetic field perturbation by a body in steps of 0.3 ppm. The magnetic field was calculated in 2D and it was assumed that the body was placed in a homogeneous magnetic field \mathbf{B}_0 in the caudo-cranial direction (Bhagwandien 1994). The figure shows that field perturbations are more severe around irregularly shaped parts of the body like the head and the head and neck region and around protruding parts like the extremities, the hands and the feet. The field perturbations around the thoracic, abdominal and pelvic regions are relatively small. Figure 4.7 shows transversal positive and negative gradient images and a composite image, which reveals distortions in the ventro-dorsal direction, which was the direction of the read-out gradient. In the positive gradient image the fatty tissues shifted in the dorsal direction, which made that the ventral tube seemed to float above the belly. In the negative gradient image the fatty tissues shifted in the ventral direction, which resulted in overprojection of the ventral tube and the subcutaneous fat. In 1.5 T images acquired with a relatively weak read-out gradient strength of 0.54 mT/m, the chemical shift of -3.2 ppm resulted in a shift of -8.9 mm of the fatty tissues with respect to the other tissues. From the

positive and the negative gradient images with a pixel size of 1.6 mm we determined contour distortions up to 6.3 ± 1.6 mm, which could be predominantly attributed to the chemical shift effect. Three plastic tubes with an inner diameter of 3 mm, filled with doped water (770 mg $\text{CuSO}_4 \cdot 5\text{H}_2\text{O}/\text{l}$), were attached to the body, one tube ventral and two tubes at either lateral side. Susceptibility-induced distortions of the markers were small. The spatial distortions of the ventral, right and left lateral marker were 2.9, -0.9 and 0.5 mm respectively in the 1.5 T positive gradient image, which was acquired with a read-out gradient strength of 0.54 mT/m.

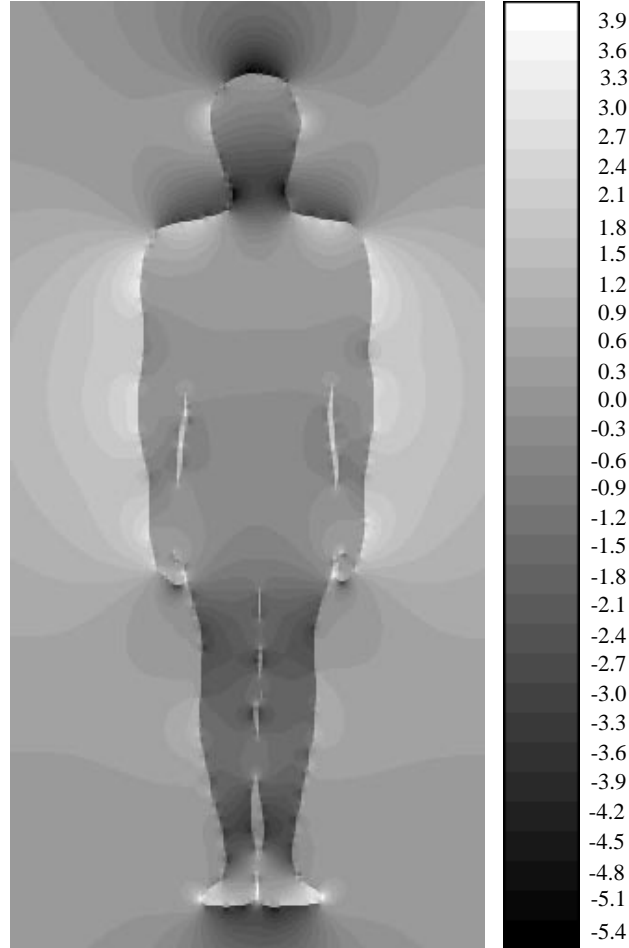


Figure 4.6: The 2D \mathbf{B} -field deviation of the body in steps of 0.3 ppm ($\chi_{\text{body}} = -9 \times 10^{-6}$, $\chi_{\text{air}} = 0$). The homogeneous magnetic field \mathbf{B}_0 is 1.5 T along the caudo-cranial direction.

4.5 Conclusions

The magnetic field around the head resembled a dipole field in the midsagittal plane of calculation with minimal field perturbation on the diagonals. The magnetic field in the localization frame depended strongly on the orientation of the Perspex plates with respect to the applied magnetic field. The maximum spatial distortion of external landmarks in the localization frame amounted 12.8 mm in a 1.5 T MR head image acquired with a read-out gradient strength of 0.68 mT/m. Susceptibility-induced distortions in the pelvic region were smaller than 3 mm in 1.5 T images acquired with a read-out gradient strength of 0.54 mT/m. From these observations we may conclude that object-related distortions can be reduced to

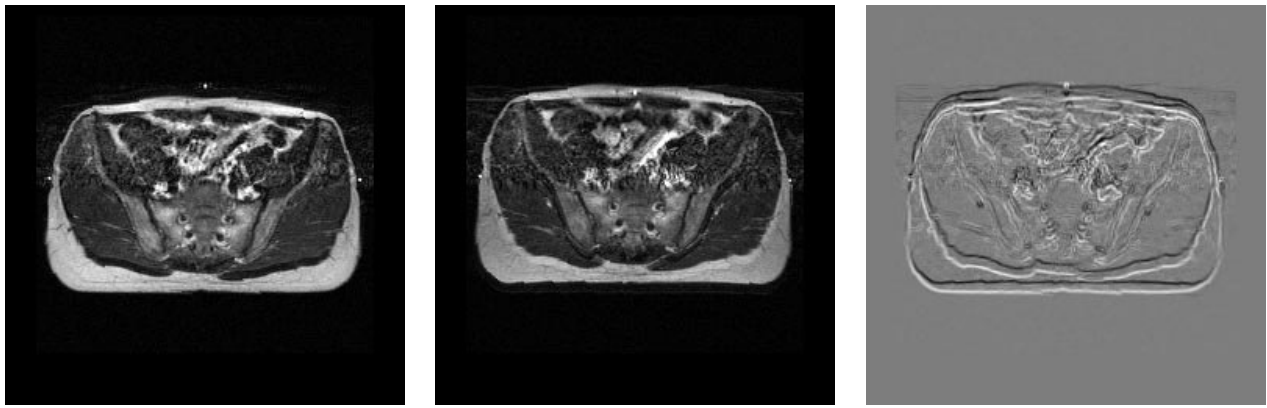


Figure 4.7: Two spin echo images of the pelvic region, acquired with opposite relatively weak read-out gradients and corrected for distortions caused by machine imperfections (read-out gradient $G_y = 0.54$ mT/m and -0.54 mT/m along the postero-anterior direction, $\mathbf{B}_0 = 1.5$ T, FOV = 400 mm, grid size = $256 * 256$ pixels), the third image is the difference of the two MR-images, illustrated by means of contours. Differences were predominantly caused by chemical shift.

the order of the pixel size by imaging at 0.5 T and using gradient strengths on the order of 3 mT/m. Whereas object-related distortions can be reduced by scan protocol optimization, image distortions caused by gradient non-linearity should be checked on each MRI scanner and if necessary corrected to meet the geometric accuracy requirements for radiotherapy treatment planning (see chapter 3).

Chapter 5

MR pulse sequence parameters
affecting the severity of geometry and
intensity distortions

5.1 Introduction

Susceptibility (χ) artifacts in MRI are caused by inhomogeneities of the static magnetic field \mathbf{B}_0 experienced by the nuclei. In part the inhomogeneity of \mathbf{B}_0 is a matter of system design (Bakker et al. 1992), in part it stems from the magnetic and geometric properties of the object being imaged (Lüdeke et al. 1985; Edmonds and Wormald 1988; Ericsson et al. 1988; Chu et al. 1990; Posse and Aue 1990; Bhagwandien et al. 1992a). In chapter 4 we have shown that not only the patient but any object in the magnet, e.g. a localization frame, causes magnetic field perturbations.

In spin echo imaging, static field errors give rise to geometric and intensity distortions in the slice selection and the read-out direction. The distortion is proportional to the field error and inversely proportional to the strengths of the applied gradients (Lüdeke et al. 1985; Ericsson et al. 1988; Chang and Fitzpatrick 1992; Bakker et al. 1992; O'Donnell and Edelstein 1985).

In gradient echo imaging, local disturbances of \mathbf{B}_0 cause, apart from the geometric effects mentioned above, severe intensity losses due to uncompensated intravoxel phase dispersion, the so called T_2^* -effect (Young et al. 1989).

In the past few years several studies have been undertaken to establish the experimental conditions which determine susceptibility artifacts in spin echo and gradient echo imaging and to provide a theoretical basis for the observed phenomena (Young et al. 1988; Haacke et al. 1989; Yamada et al. 1990; Cho and Ro 1992; Summers et al. 1986). In previous work (Bakker et al. 1993) we proposed a method for simulation of susceptibility artifacts, which follows the actual sequence of events in an imaging experiment and deals with the effects of error fields in the time domain (\mathbf{k} -space). Simulation in the time domain requires a precise definition of the pulse sequence and the data acquisition scheme involved, and a specification of the field of view, output resolution, the amplitude and the duration of the gradients, and the number of phase and frequency samples. Most parameters are known to the operator, but some parameters may be hidden or their values may be determined by other parameters, e.g. the range of selectable gradient amplitudes may depend on the acquisition matrix and the field of view. In our experience, it is not generally recognized which factors are pertinent to the severity of the susceptibility artifacts. For radiotherapy treatment planning purposes, it would seem a useful exercise to take a simple phantom and carry out the necessary experiments to identify the scan parameters, which affect the severity of susceptibility artifacts in MR imaging.

5.2 Methods and materials

All experiments in this study were carried out with a coaxial cylinder phantom with its axis perpendicular to the scan table and \mathbf{B}_0 . The magnetic field in and around a coaxial cylinder is theoretically well understood (Lüdeke et al. 1985) and was subject of previous experiments and simulation studies (Bakker et al. 1992; Bhagwandien 1994). The phantom consisted of a bottle containing mildly doped water ($T_1 \approx 1000$ ms, $T_2 \approx 95$ ms) and a 12 mm diameter cylindrical air cavity. Imaging of the coaxial cylinder was performed in the coronal plane, so that slice selection effects could be ignored. Imaging was done on a 1.5 T whole body MRI scanner with 15 mT/m maximum gradient capability (Gyrosan ACS-NT, Philips Medical Systems, Best, The Netherlands). In order to identify the scan parameters, which affect the severity of susceptibility artifacts, the phantom was subjected to currently available scan techniques and options for the parameter settings usually encountered in clinical studies.

Images were taken with a slice thickness of 5 mm. The severity of the susceptibility artifacts for different scan techniques and parameter settings was evaluated by visual inspection.

5.3 Results and discussion

The appearance of susceptibility artifacts and its dependence on scan parameters is described for the basic spin echo (SE) and fast field echo (FFE) pulse sequences and the fast variants, namely the turbo spin echo (TSE) and echo planar imaging (EPI) pulse sequences. Other available pulse sequences such as inversion recovery (IR), turbo field echo (TFE) and gradient and spin echo (GRASE) can be thought of as modifications and/or combinations of the basic pulse sequences (GRASE is a combination of TSE and EPI), resulting in susceptibility artifacts which generally could be explained from the artifacts also occurring for their constituting basic pulse sequences.

In spin echo imaging, the echo of the MR signal is recalled by a 180° RF pulse which rephases the magnetization. At the centre of the echo, rephasing of reversible relaxation due to applied magnetic gradients and static magnetic field inhomogeneities is complete and the dephasing develops as time increases in either direction away from the centre of the echo signal, resulting in geometry and concurrent intensity distortions (see chapter 2).

In fast field echo imaging, an echo signal of the transverse magnetization is produced by gradient reversal which does not eliminate the dephasing effects of magnetic field inhomogeneities. Dephasing begins at the excitation pulse and progresses with time throughout the sampling period resulting not only in geometry distortions, but also in signal loss (see chapter 2).

Turbo spin echo imaging is a fast imaging method which acquires a number of profiles after a single excitation. The turbo factor specifies the number of profiles to be measured after each excitation. As in SE imaging, the echos of the MR signal are recalled by 180° RF pulses. The experiments revealed that turbo spin echo experiments were, in principle, not more sensitive to susceptibility artifacts than spin echo experiments. However, since the minimal water fat shift selectable was smaller in TSE experiments than in SE experiments with identical acquisition matrix and field of view, the achievable geometric accuracy was higher in the TSE experiments.

Echo planar imaging is a fast imaging method which acquires a number of profiles after a single excitation. The spatial information is encoded by an oscillating frequency-encoding gradient in combination with a small and constant phase-encoding gradient, thus, as in FFE imaging, the echos of the MR signal are produced by gradient reversals. In a variant of EPI, the constant phase-encoding gradient is replaced by a series of short phase-encoding gradient pulses (see chapter 2). The EPI experiments were sensitive to both geometry distortions and signal loss (figure 5.5). Geometric distortions occurred in both the frequency and phase-encoding direction. However, distortions in the phase-encoding direction dominated distortions in the frequency-encoding direction, since the phase-encoding gradient pulses are smaller than the read-out gradient pulses, especially in the case of single shot EPI (see chapter 2). Distortions are reduced in multiple shot EPI, where the EPI factor specifies the number of profiles to be measured after a single excitation. Distortions were most severe in EPI sequences with large EPI factors and thus small phase-encoding gradient pulses (figure 5.5). EPI can be combined with spin echo imaging (SE-EPI). The SE-EPI experiments were sensitive to geometry distortions, but not to signal loss (figure 5.6).

In the following the most common scan parameters are briefly described and its influence

on the appearance of susceptibility artifacts discussed.

Water fat shift. The water fat shift was a main determinant of susceptibility artifacts. At the Philips Gyroscan ACS-NT, the water fat shift parameter controls the misregistration (in pixels) of adipose tissue with respect to watery tissues. The frequency at which transverse magnetization precesses depends slightly on the molecular environment (Stark and Bradley 1992). The precessional frequency for magnetization from a watery tissue, such as muscle, is about 3.2 parts per million (ppm) larger than that for adipose tissue. This difference of precessional frequencies is called the chemical shift or water fat shift. A 3.2 ppm water fat shift changes the precessional frequency by 204 Hz at 1.5 T. Water fat shifts cause spatial misregistration in MR images. Magnetic field variations originating from susceptibility inhomogeneities also cause geometrical distortions and apparent intensity changes, both along the read-out direction of the image (O'Donnell and Edelstein 1985; Lüdeke et al. 1985). These distortions could be reduced by decrease of the water fat shift parameter, which physically meant increase of the amplitude of the read-out gradient pulse and concurrent increase of the sampling frequency at the same field of view and acquisition matrix resulting in a greater bandwidth per pixel. Figures 5.1 and 5.2 show the geometry distortions and concurrent intensity changes in SE and FFE images for different values of the water fat shift parameter. The arrow in figure 5.1a depicts the direction of the read-out gradient, which was caudo-cranial as in all images in this chapter, except the image of figure 5.7b.

Field of view (FOV). The field of view defines the area of the object to be imaged. The edges of the FOV are determined by the highest frequency of the MR signals that is sampled and thus on the amplitude of the frequency-encoding pulse and the sampling interval. The FOV influences the size of pixels or the spatial resolution in an MR image. The appearance of susceptibility artifacts depended on the field of view. Increase of the FOV at the same acquisition matrix and water fat shift (in pixels) resulted in larger voxels and thus in more severe signal loss by intravoxel dephasing in FFE and in greater geometrical distortions (in mm) in SE, FFE and EPI. Increase of the FOV at the same acquisition matrix and water fat shift (in pixels) is physically achieved by a proportional decrease of the amplitude of the read-out gradient.

Fold-over. Fold-over is also called back-folding or wrap-around and occurs if the dimension of the object in the phase-encoding direction is larger than the field of view. The part of the object outside the field of view is folded back at the opposite of the image. The parameter fold-over direction chooses the direction of the phase-encoding gradient and thus the direction of the read-out gradient, which is the direction of geometric distortions caused by magnetic field inhomogeneity. Fold-over suppression eliminates fold-over artifacts by oversampling or REST (regional saturation technique). REST is a saturation technique to suppress the MR signal from two contiguous slabs next to the field of view. Neither oversampling nor REST influenced the appearance of susceptibility artifacts.

Scan matrix. The scan matrix defines the number of phase-encoding and frequency-encoding steps to be measured, usually 256^2 . The scan matrix influences the scan duration, the signal to noise ratio and the resolution of the images. Decrease of the scan matrix at the same FOV and water fat shift (in pixels) resulted in larger voxels and thus in more severe signal loss by intravoxel dephasing in FFE and in greater geometrical distortions (in mm) in SE, FFE and EPI.

Scan percentage. The parameter scan percentage allows a reduced number of phase-

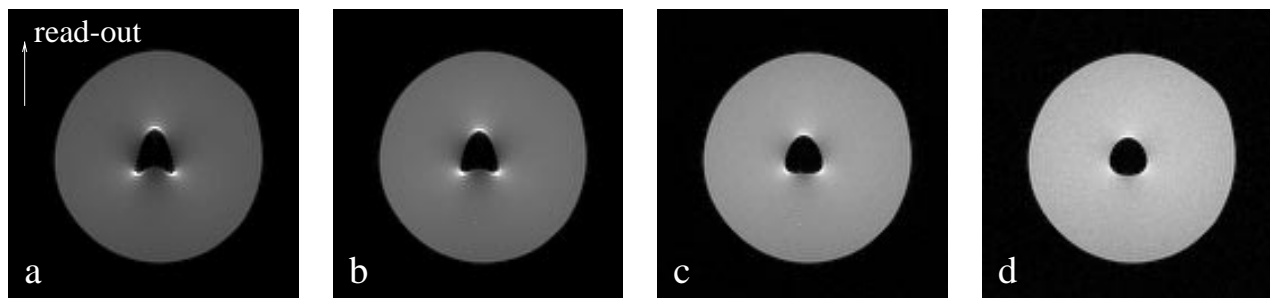


Figure 5.1: Coronal 2DFT SE images of the coaxial cylinder for different values of the water fat shift parameter: a) wfs = 5 pixels, b) wfs = 4 pixels, c) wfs = 2 pixels and d) wfs = 1 pixel. Other parameters: $TR = 250$ ms, $TE = 30$ ms, FOV = 256 mm. The arrow depicts the direction (caudo-cranial) of the read-out gradient.

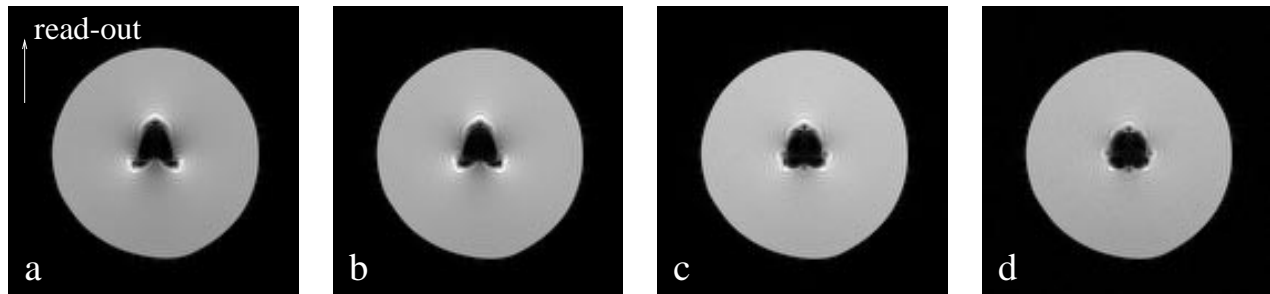


Figure 5.2: Coronal 2DFT FFE images of the coaxial cylinder for different values of the water fat shift parameter: a) wfs = 5 pixels, b) wfs = 4 pixels, c) wfs = 2 pixels and d) wfs = 1 pixel. Other parameters: $TR = 250$ ms, $TE = 14.1$ ms, FOV = 256 mm. The arrow depicts the direction (caudo-cranial) of the read-out gradient.

encoding steps (profiles) to be measured resulting in a proportional reduction of scan time. Only the central profiles are sampled and the missing profiles are filled with zeros. Since the higher profiles are not measured, the spatial resolution (in the foldover direction of the image) is reduced. Ringing artifacts may occur at high contrast transitions (Gibbs phenomenon). In spin echo imaging, the susceptibility artifacts were not dependent on the scan percentage. In gradient echo imaging, a 50% acquisition resulted in more severe signal loss compared to a 100% acquisition (figures 5.3a and b).

Half scan. Half scan is an acquisition method in which half of the phase-encoding steps is acquired, resulting in a reduction of the scan time. Half scan is possible under the condition of perfect magnetic field homogeneity, since in that case the spatial frequency spectrum

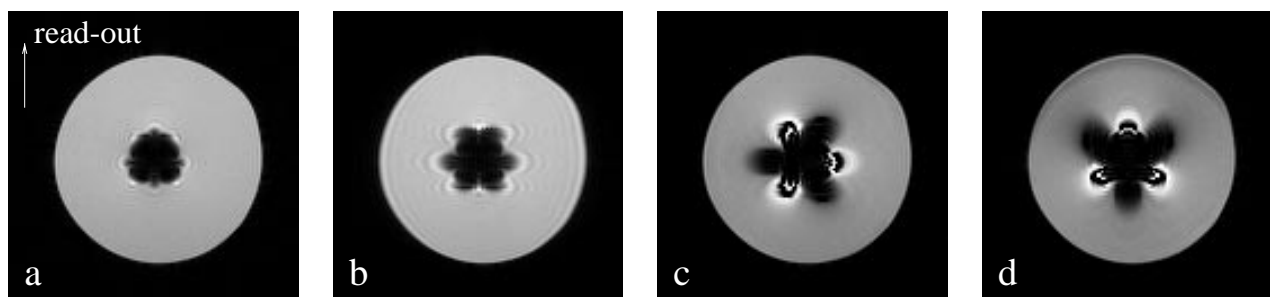


Figure 5.3: Coronal 2DFT FFE images of the coaxial cylinder for different scan matrices: a) 100% acquisition, b) 50% acquisition, c) half scan and d) partial echo. Other parameters: $TR = 250$ ms, $TE = 30$ ms, water fat shift = 2 pixels, FOV = 256 mm. The arrow depicts the direction (caudo-cranial) of the read-out gradient.

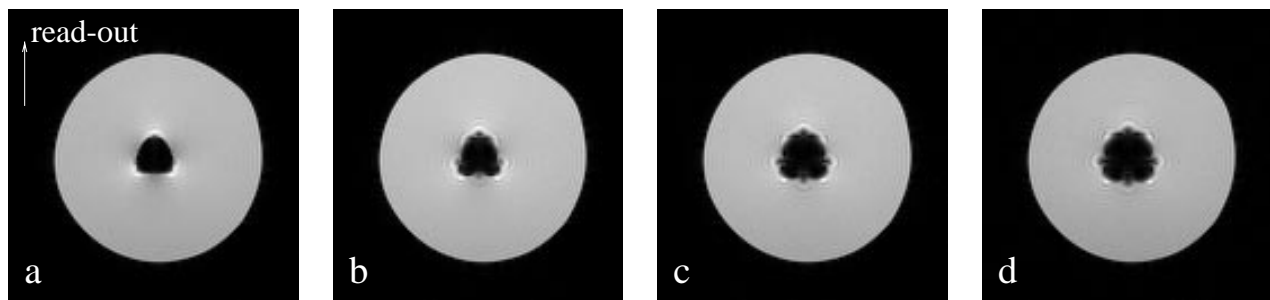


Figure 5.4: Coronal 2DFT FFE images of the coaxial cylinder for different echo times: a) $TE = 7.5$ ms, b) $TE = 15$ ms, c) $TE = 22.5$ ms and d) $TE = 30$ ms. Other parameters: $TR = 250$ ms, water fat shift = 2 pixels, FOV = 256 mm. The arrow depicts the direction (caudo-cranial) of the read-out gradient.

corresponding to a stationary object possesses conjugate symmetry (Song et al. 1982), in other words, data of measurements made with a certain positive value of the phase-encoding gradient are identical to the data with the same negative value. The other half of the matrix can be replicated from the measured data. In contrast to reduced acquisition, half scan does not affect the spatial resolution of the image. In reduced acquisition, only the central profiles are acquired, resulting in a loss of resolution of the image. In half scan, however, one half of the matrix is acquired and since the highest profiles are included, there is no loss of resolution in the phase-encoding direction of the image. If static field inhomogeneities introduce phase errors, the complete spatial frequency spectrum is required to reconstruct an accurate image of the object and half scan will affect the susceptibility induced signal loss in gradient echo imaging (figure 5.3c). In fact, in half scan techniques a little more than half the acquisition matrix is acquired to correct to some extent for phase errors.

Partial echo. Partial echo is an acquisition method in which half of the acquisition data in the read-out direction is acquired. It allows shorter echo times and the fine resolution of the image is not affected. Partial echo also makes use of the symmetry in the data. The second half of the data is replicated from the measured data. However, because of the field inhomogeneity induced by the coaxial cylinder, partial gradient echo imaging resulted in signal loss in the same way as half scan, apart from a 90° rotation (figures 5.3c and d). In fact, a little more than half the acquisition data is acquired to correct to some extent for phase errors.

Echo time TE . The influence of the echo time depends on the pulse sequence. In FFE imaging, dephasing begins at the excitation pulse and progresses with time throughout the sampling period. Signal loss caused by intra-voxel dephasing increased with echo time in FFE and EPI (figure 5.4). The minimum TE is longer for low-bandwidth pulse sequences, because the sample interval is longer and one-half the data samples are collected before TE (Stark and Bradley 1992). If a spin echo is used for data acquisition, dephasing due to magnetic field inhomogeneities is eliminated at the echo centre. The echo time TE did not affect geometry distortions or signal loss in SE and TSE.

Modified spin echo (MSE). Modified spin echo is available for single echo SE scans. MSE is selected in spin echo scans with short repetition time. The spin echo pulse is followed by an additional RF pulse to realign the magnetization with the direction of the main magnetic field. This parameter did not affect the appearance of susceptibility artifacts.

TSE factor. The TSE factor is the number of profiles acquired after each excitation and thus determines the scan time reduction in turbo spin echo imaging. This parameter did not influence the appearance of susceptibility artifacts.

Profile order. The profile order can be selected for turbo spin echo imaging and can be

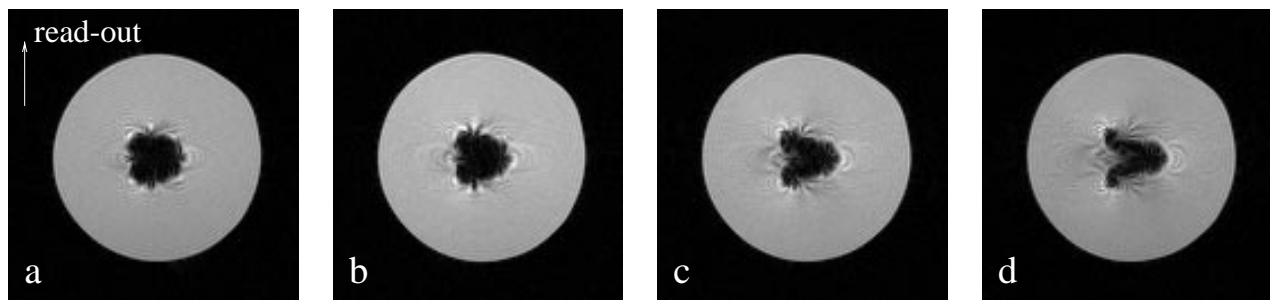


Figure 5.5: Coronal 2DFT EPI images of the coaxial cylinder for different values of the EPI factor and the resulting water fat shift in the phase-encoding direction: a) EPI factor = 3, wfs = 2.7 pixels, b) EPI factor = 5, wfs = 4.1 pixels, c) EPI factor = 9, wfs = 6.8 pixels and d) EPI factor = 13, wfs = 9.5 pixels. Other parameters: $TR = 250$ ms, $TE = 30$ ms, $FOV = 256$ mm. The arrow depicts the direction (caudo-cranial) of the read-out gradient. Note that geometry distortions are most severe in the phase-encoding direction (left-right).

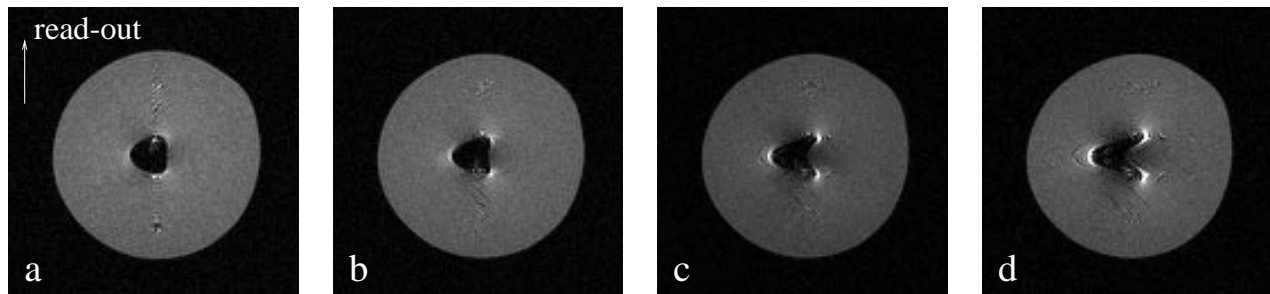


Figure 5.6: Coronal 2DFT SE-EPI images of the coaxial cylinder for different values of the EPI factor and the resulting water fat shift in the phase-encoding direction: a) EPI factor = 3, wfs = 2.7 pixels, b) EPI factor = 5, wfs = 4.0 pixels, c) EPI factor = 9, wfs = 6.7 pixels and d) EPI factor = 13, wfs = 9.4 pixels. Other parameters: $TR = 250$ ms, $TE = 80$ ms, $FOV = 256$ mm. The arrow depicts the direction (caudo-cranial) of the read-out gradient. Note that geometry distortions are most severe in the phase-encoding direction (left-right).

linear, reverse linear, or low-high. TSE profile order and TSE factor influence the interval between two echoes, the so called echo spacing. The appearance of susceptibility artifacts was not affected by the profile order.

EPI factor. This factor determines the number of gradient reversals per MR signal and thus the scan time reduction in echo planar imaging. The EPI factor influences the amplitude and duration of the phase-encoding gradient pulses and thus the resulting water fat shift (as a measure for distortions) in the phase-encoding direction. Distortions occurred in both the frequency and phase-encoding directions. However, distortions in the phase-encoding direction dominated, since the phase-encoding gradient pulses are smaller than the read-out gradient pulses (see chapter 2). Distortions were most severe in EPI sequences with large EPI factors and thus small phase-encoding gradient pulses. The EPI factor did not noticeably affect the severity of signal loss in echo planar imaging (figure 5.5). In spin echo-echo planar imaging (SE-EPI), the 90° excitation pulse is followed by a 180° refocussing pulse to reduce the susceptibility effects. SE-EPI images showed geometry distortions, but no signal loss (figure 5.6)

Optimized second echo. This parameter enables optimization of the second echo by decreasing the read-out gradient strength to increase the signal to noise ratio. Setting this parameter will adversely affect the severity of susceptibility artifacts in the second echo image.

RF pulse angle. The RF pulse angle is the rotation angle by which the magnetization is

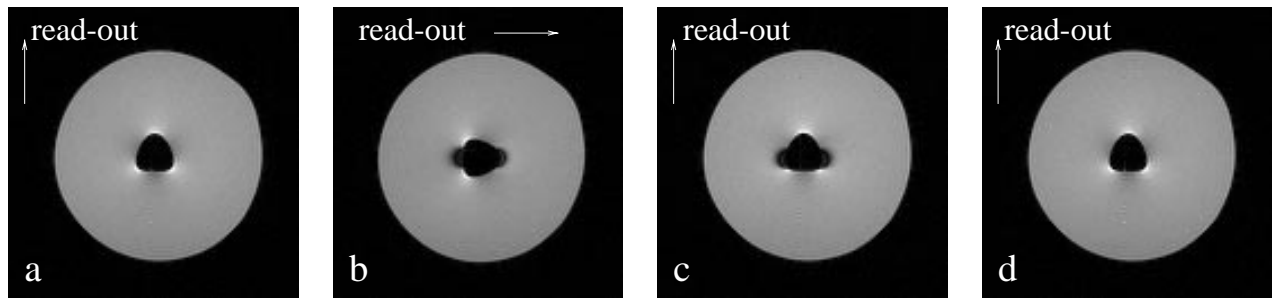


Figure 5.7: Coronal 2DFT SE images of the coaxial cylinder: a) standard, b) SPIR, left-right read-out gradient, c) SPIR, caudo-cranial read-out gradient and d) MTC. Other parameters: $TR = 250$ ms, $TE = 30$ ms, water fat shift = 2 pixels, FOV = 256 mm. The arrows depict the direction of the read-out gradient.

rotated around an axis perpendicular to the main magnetic field during the RF excitation pulse. This parameter did not affect the appearance of susceptibility artifacts.

Repetition time. The repetition time is the time between two successive excitation pulses (90°) of the same slice. This parameter did not affect the appearance of susceptibility artifacts.

Contrast enhancement. This parameter controls the type of FFE sequence that will be executed. The options no enhancement and T_1 -enhancement gave identical signal loss and the option T_2 -enhancement resulted in geometry distortion but no signal loss, which may be explained by the fact that the stimulated echo of a T_2 -enhanced gradient echo experiment behaves like a spin echo.

Auto shim. Setting this parameter activates a preparation phase to optimize the main magnetic field homogeneity. Extra shimming is performed with the linear gradient components on a large volume. Shimming improves global magnetic field homogeneity, but local magnetic field perturbations at interfaces of materials with different susceptibilities cannot be corrected by the linear gradient components and thus auto shimming did not affect the appearance of susceptibility artifacts.

Spectral presaturation with inversion recovery (SPIR). This technique enables the suppression of the fat component in images. Setting this parameter resulted in suppression of signal from regions with about 3.2 ppm magnetic field perturbation (figures 5.7b and c) and thus influenced the appearance of susceptibility artifacts.

Magnetization transfer contrast (MTC). This parameter manipulates contrast in certain tissues or between different tissues by applying an RF prepulse before the imaging sequence. The result of the MTC prepulse is that bound water is saturated, but due to magnetization transfer, the magnetization of the free water is transferred to the bound water until equilibrium is reached. The resulting images will have less signal from the free water, i.e. tissue will appear darker. This parameter did not affect the appearance of susceptibility artifacts (figure 5.7 d).

Number of signals averaged (NSA). The number of signal averages defines the number of times a profile is measured. Increasing NSA increases signal to noise ratio, decreases motion and flow artifacts, but linearly increases scan times. This parameter did not affect the appearance of susceptibility artifacts.

5.4 Conclusions

The strength of the read-out gradient, which is controlled by the water fat shift parameter, was the main factor affecting the severity of the susceptibility artifact. The range of water fat shifts, that could be selected, was influenced by the field of view and the acquisition matrix. In echo planar imaging, the EPI factor strongly influenced the severity of geometric distortions in the phase-encoding direction. In applications of MRI, which require geometric accuracy, we should be aware that these parameters indirectly affect the severity of image distortions. Spatial distortions occurred in the direction of the read-out gradient in SE and FFE imaging but also and more strongly in the direction of the phase-encoding gradient in echo planar imaging. The direction of the read-out gradient was controlled by the fold-over direction parameter, which is the direction of the phase-encoding gradient. Signal loss was most severe in FFE images acquired with relatively long echo times and/or in case of partial \mathbf{k} -space sampling (reduced scan matrix, half matrix or partial echo). Generally, highest accuracy and least signal loss is achieved in spin echo imaging with minimal water fat shift and in fast field echo imaging with minimal water fat shift and short echo time.

Chapter 6

Investigation of geometric distortions in 1.5 T magnetic resonance images for use in radiotherapy treatment planning of patients with brain tumours

This chapter is based on the following publication:

M.A. Moerland, R. Beersma, R. Bhagwandien, H.K. Wijrdeman and C.J.G. Bakker. Analysis and correction of geometric distortions in 1.5 T magnetic resonance images for use in radiotherapy treatment planning. *Physics in Medicine and Biology*, 40, 1651-1664, 1995.

Abstract

The aim of this study is to investigate and correct for machine and object related distortions in magnetic resonance images for use in radiotherapy treatment planning.

Patients with brain tumours underwent magnetic resonance imaging (MRI) in the radiotherapy position with the head fixed by a plastic cast in a Perspex localization frame. The imaging experiments were performed on a 1.5 T whole body MRI scanner with 3 mT/m maximum gradient capability. Image distortions, caused by static magnetic field inhomogeneity, were studied by varying the direction of the read-out gradient. For purposes of accuracy assessment, external and internal landmarks were indicated. Tubes attached to the cast and in the localization frame served as external landmarks. In the mid-sagittal plane the brain-sinus sphenoidalis interface, the pituitary gland-sinus sphenoidalis interface, the sphenoid bone and the corpora of the cervical vertebra served as internal landmarks. Landmark displacements as observed in the reversed read-out gradient experiments were analyzed with respect to the contributions of machine related static magnetic field inhomogeneity and susceptibility and chemical shift artifacts. The machine related static magnetic field inhomogeneity in the mid-sagittal plane was determined from measurements on a grid phantom. Distortions due to chemical shift effects were estimated for bone marrow containing structures like the sphenoid bone and the corpora of the cervical vertebra using the values obtained from the literature. Susceptibility induced magnetic field perturbations are caused by the patient and the localization frame. Magnetic field perturbations were calculated for a typical patient dataset. The mid-sagittal head image was converted into a susceptibility distribution by segmenting the image into water equivalent tissues and air. Also the Perspex localization frame was included in the susceptibility distribution. Given the susceptibility distribution, the magnetic field was calculated by numerically solving the Maxwell equations for a magnetostatic field. Results were shown as magnetic field perturbations and corresponding spatial distortions of internal and external landmarks. The mid-sagittal head images were corrected for the machine imperfections (gradient non-linearity and static magnetic field inhomogeneity). The locations of the external landmarks in the frame were also corrected for susceptibility artifacts. The efficacy of the corrections was evaluated for these external landmarks in the localization frame with known geometry.

In this study at 1.5 T with read-out gradient strength of 3 mT/m, machine related and susceptibility induced static magnetic field inhomogeneity were on the same order, resulting in spatial distortions between -2 and 2 mm. Internal structures containing yellow bone marrow (the sphenoid bone) shifted 1.6 mm and structures containing red bone marrow shifted 0.8 mm in the direction opposite to the read-out gradient. Both the patient and the localization frame proved to perturb the magnetic field. The field perturbations were shown to be additive. In total, static magnetic field inhomogeneity led to spatial distortions ranging from -2 to 4 mm in the direction of the read-out gradient. Non-linearity of the gradients resulted in spatial distortions ranging from -3.5 to 0.5 mm. After correction for the machine imperfections and susceptibility artifacts, the geometric accuracy of the landmarks in the localization frame was better than 1.3 mm.

6.1 Introduction

In radiotherapy treatment planning (RTP) accurate localization of tumour volume and critical organs and accurate placement of treatment fields is of major importance, because it enables the radiation dose to the tumour to be increased whilst allowing the dose to the sur-

rounding dose limiting normal brain tissues to be minimized (Brahme 1984; Dutreix 1984; Goitein 1985; Mijnheer et al. 1987; Suit and Du Bois 1991; Suit and Miralbell 1989). Of the different imaging modalities, magnetic resonance imaging (MRI) shows most promise for tumour localization for RTP because of its excellent soft tissue contrast resolution and ability to scan in any plane orientation (Heesters et al. 1993; Just et al. 1991; Stark and Bradley 1992; TenHaken et al. 1992). However, the introduction of MRI into RTP is seriously hampered by the geometric distortions of magnetic resonance (MR) images. MR image distortions are caused by non-linearity of the gradients and static magnetic field inhomogeneity. Field inhomogeneity is known to stem from the MRI scanner and from the magnetic properties of the object itself (Bakker et al. 1992; Bhagwandien et al. 1992a; Ericsson et al. 1988; Lüdeke et al. 1985; Schad et al. 1987a). The feasibility of measurement and correction of machine-related distortions has been demonstrated before (Bakker et al. 1992; Schad et al. 1987a; Sekihara et al. 1984). The magnetic properties of the object induce the chemical shift and the susceptibility artifacts in MR images. The term 'chemical shift' is given to the variation in resonant frequency of a particular nucleus with molecular environment. The relative shift in the resonant frequency is caused by the local magnetic field due to the surrounding molecular structure. Protons in fat experience a magnetic field, which is 3.2 parts per million (ppm) weaker than the magnetic field experienced by protons in water (Dixon 1984). In 2-dimensional Fourier transform (2DFT) imaging, the read-out gradient relates the frequency of a proton to its location along the read-out gradient axis. The consequence for MRI is, that the fat-containing tissues will be shifted with respect to the other tissues. Susceptibility is the property which relates the magnetization of an object to the applied magnetic field. Susceptibility distributions lead to magnetic field perturbations, e.g. the presence of a patient in an MRI scanner will perturb the applied magnetic field because of the difference in susceptibility between the patient's body and the surrounding air. The severity of the field perturbations outside the body depends on the susceptibility difference with the surrounding air, the shape of the body and the orientation of the body with respect to the applied magnetic field. Field perturbations are more severe around protruding parts like the extremities, the fingers of the hand and the nose. Inside the human body static magnetic field inhomogeneity is influenced by the shape of the body and the presence of local susceptibility inhomogeneities, e.g. the tissue-air interfaces around air cavities. External devices like localization frames as used for RTP will also perturb the magnetic field. Correction methods for susceptibility induced geometric distortions have been described and the efficacy has been demonstrated for the correction of distorted phantom images (Bakker et al. 1992; Bhagwandien 1994; Chang and Fitzpatrick 1992; Cho et al. 1988) and in a single case for the correction of an MR head scan (Sumanaweera et al. 1993). Machine imperfections and magnetic properties of the object (chemical shift and susceptibility) lead to static magnetic field inhomogeneity. The resulting image distortions can be reduced by choosing maximum read-out and slice-selection gradients (Bakker et al. 1992; Chang and Fitzpatrick 1992). The aim of this work is to analyze and correct for image distortions in studies on patients with brain tumours, which were imaged in the radiotherapy position on a 1.5 T MRI scanner with the head fixed by a cast in a localization frame as described by Leksell (1951). MRI compatible localization frames are widely used for image registration purposes. However, MRI compatibility does not mean that the applied magnetic field is not perturbed and in our view this problem has not been fully explored yet. Magnetic field perturbations will be measured by means of reversed read-out gradient experiments. The contribution of susceptibility induced magnetic field inhomogeneity will be analyzed using a numerical method for calculating the magnetic field for arbitrary magnetic susceptibility

distributions (Bhagwandien et al. 1992a). The efficacy of the methods for correction of distortions caused by non-linearity of the gradients and static magnetic field inhomogeneity will be investigated using the frame with known geometry.

6.2 Methods and materials

6.2.1 Experiments

Ten patients with brain tumours underwent MR scanning in the radiotherapy position on a flat table top with the head fixed by a plastic cast in a home-built localization frame. Imaging experiments were performed on a 1.5 T whole body MRI scanner with 3 mT/m maximum gradient capability (Gyrosan S15, Philips Medical Systems, Best, The Netherlands). The pulse sequences were a conventional T_2 -weighted spin echo sequence for tumour visualization ($TR \approx 2000$ ms, $TE = 30, 100$ ms, NEX = 2, matrix = 256 x 256, number of slices ≈ 15 , slice thickness = 5 mm, slice gap = 1 mm, FOV = 320 mm, offset = 60 mm anterior, magnitude reconstruction) and a T_1 -weighted spin echo sequence with reversed read-out gradient for the study of image distortions caused by static magnetic field inhomogeneity ($TR \approx 900$ ms, $TE = 30$ ms, other parameters as above). These datasets acquired with opposite directions of the read-out gradient enable the study of image distortions caused by static magnetic field inhomogeneity. Since static magnetic field inhomogeneity results in spatial distortions in the direction of the read-out gradient, the true position (apart from distortions caused by gradient errors) of an image structure is half-way between the two distorted positions in both datasets (Chang and Fitzpatrick 1992). In the following, a spatial distortion is defined as the distance between the true position and the distorted position and a displacement is defined as the distance between two positions in images acquired with opposite directions of the read-out gradient. Distortions caused by static magnetic field inhomogeneity are inversely proportional to the strength of the read-out gradient; this gradient was chosen to be a maximum (3 mT/m) to give minimal distortions. In the experiments at 1.5 T with read-out gradient strength of 3 mT/m, static magnetic field inhomogeneity results in spatial distortions of 0.5 mm per ppm. Although beyond the scope of this study, the slice-selection gradient was also chosen to be a maximum (3 mT/m) to reduce plane warp. The localization frame is shown in figure 6.1. The plastic cast and the frame are both attached to a base plate, so that patient and frame can be positioned reproducibly. The five Perspex plates of the frame and the base form a box, open at the caudal end, with outer dimensions width x height x length = 30 cm x 27 cm x 27 cm. This set-up fits closely in the body coil of the MRI scanner and provides enough space for a patient to be positioned with the head on a headrest, which is also used during radiotherapy. For purposes of accuracy assessment, external and internal landmarks were chosen. Plastic tubes with an inner diameter of 2 mm, filled with doped water (770 mg $\text{CuSO}_4 \cdot 5\text{H}_2\text{O}/\text{l}$), were set in a Z-shape in grooves milled in the Perspex plates. Together with three tubes attached to the cast of the patient at the position of the forehead they served as external landmarks (figure 6.2a). In the mid-sagittal plane the pituitary gland, the brain-sinus sphenoidalis interface, the sphenoid bone and the corpora of the cervical vertebra served as internal landmarks. The image coordinates of the external landmarks were determined using an algorithm which calculates the center of gravity of signal intensities within an interactively positioned square of pixels. The internal landmarks were indicated interactively. Displacements around air cavities were measured at the brain-sinus sphenoidalis interface and the pituitary gland-sinus sphenoidalis interface (figure 6.2a). The position of the pituitary gland was characterized by its most

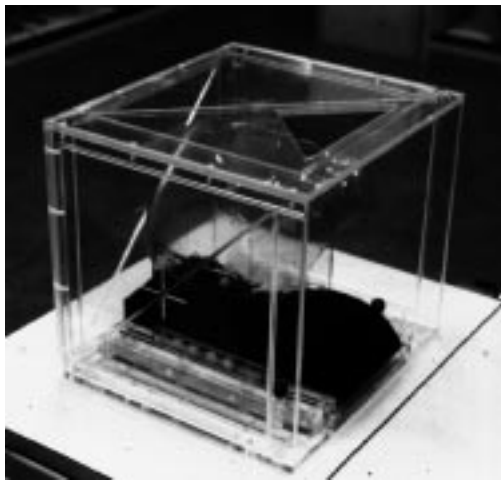


Figure 6.1: The localization frame with headcast and headrest.

caudal extension (interface pituitary gland-sinus sphenoidalis). The sphenoid bone and the corpora of the cervical vertebra were indicated at the corner points. For these structures the displacements of the corner points were averaged to obtain the displacement of each structure.

6.2.2 Analysis

The landmark displacements, as observed in the reversed read-out gradient experiments, originate from machine related static magnetic field inhomogeneity, susceptibility and chemical shift artifacts. The experiments reveal total displacements; the different contributions cannot be separated. The contribution of machine related static magnetic field inhomogeneity could be determined from measurements on a grid phantom (see subsection 6.2.3). Contributions of chemical shift effects are to be expected for bone marrow containing structures like the sphenoid bone and the corpora of the cervical vertebra. Values for these contributions were obtained from literature. The contribution of susceptibility induced static magnetic field inhomogeneity was numerically calculated.

Susceptibility induced field perturbations may be caused by the patient and the localization frame. The susceptibility induced magnetic field perturbations were calculated for a typical patient in this study. The mid-sagittal MR image was converted into a susceptibility distribution by segmenting the image into water equivalent tissue (soft tissues and bone: susceptibility $\chi = -9 \times 10^{-6}$) and air ($\chi = 0$). This is a fair approximation, since significant susceptibility inhomogeneities only occur at tissue-air interfaces. Soft tissues, blood and bone show susceptibilities ranging from -7.5 to -10×10^{-6} (Bhagwandien 1994; Sumanaweera et al. 1993; Weast and Astle 1980; Weisskoff and Kiihne 1992). The Perspex frame was included in the susceptibility distribution guided by the location of the tubes, which were clearly visible in the MR images (figure 6.2a). The susceptibility of Perspex was determined from reversed read-out gradient experiments on a coaxial cylinder with a Perspex inner region and the annular region filled with water (Lüdeke et al. 1985; Sumanaweera et al. 1993). Spin echo and gradient echo images were acquired with minimal read-out gradient ($G = 0.85$ mT/m) to obtain maximal sensitivity for visualization of susceptibility induced image distortions. Nevertheless, the images showed no susceptibility artifacts, from which we could conclude that the susceptibility of Perspex is equal to that of water: $\chi_{\text{Perspex}} = -9 \times 10^{-6}$. Given this susceptibility distribution, the magnetic field was calculated by numerically solv-

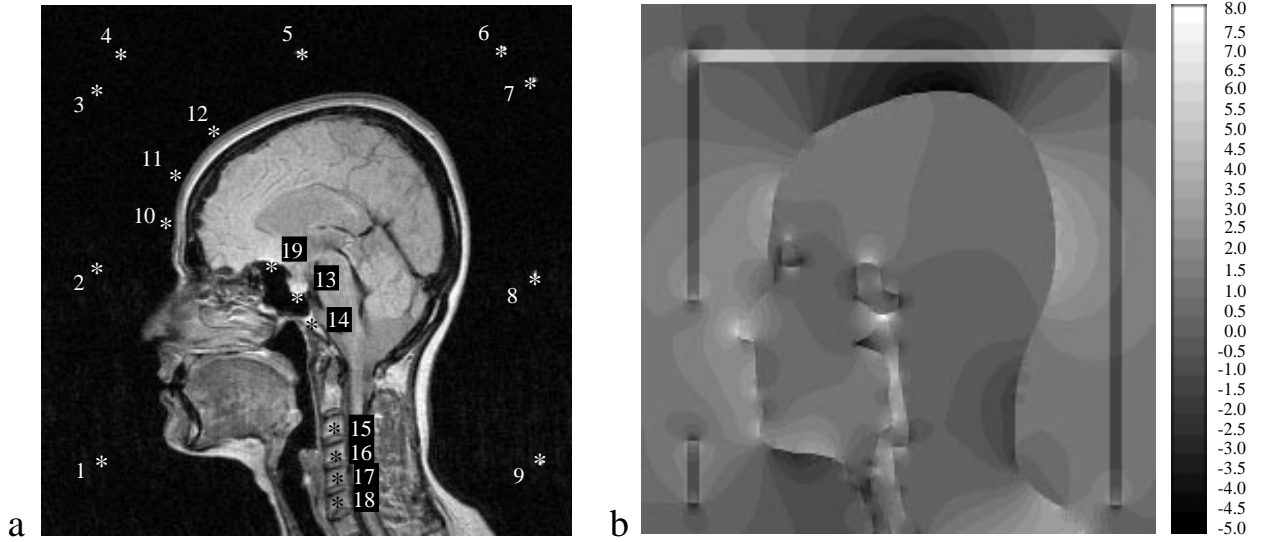


Figure 6.2: a) Mid-sagittal MR head image with internal and external landmarks indicated: 1-9, external landmarks in the localization frame; 10-12, external landmarks attached to the cast at the forehead; 13, pituitary gland; 14, sphenoid bone; 15-18, corpora of the cervical vertebra; 19, interface brain-sinus sphenoidalis. b) Calculated magnetic field perturbations in the mid-sagittal plane. The perturbations are shown by means of shades with a step size of 0.5 ppm. Light shades indicate a stronger field, dark shades indicate a weaker field than the 1.5 T magnetic field, applied in the caudo-cranial direction. The head was segmented into soft tissues, bone and Perspex: $\chi = -9 \times 10^{-6}$ and air: $\chi = 0$. Note the variation in magnetic field perturbation with the orientation of the Perspex plates.

ing the Maxwell equations (Bhagwandien et al. 1992a; Bhagwandien et al. 1994). In the following we will give a brief description of the method. The Maxwell equations for magnetostatic problems reduce to the Laplace equation

$$\nabla \cdot (\mu \nabla \Phi_M) = 0, \quad (6.1)$$

where μ is the magnetic permeability (dimensionless) ($\mu = 1 + \chi$), χ the magnetic susceptibility (dimensionless) and Φ_M the magnetic scalar potential [Wb/m]. For a given μ -distribution, Φ_M is determined by (numerically) solving eq. (6.1). This is done by transforming eq. (6.1) into a diffusion equation with the introduction of an iteration coordinate τ (a pseudo time). The stationary state of the diffusion equation is then the magnetic scalar potential (Φ_M) distribution. This means that the general definition of convergence of such a process has the form

$$C \frac{d\Phi_M(x, y, z; \tau)}{d\tau} = \nabla \cdot (\mu(x, y, z) \nabla \Phi_M(x, y, z; \tau)), \quad (6.2)$$

where

$$\lim_{\tau \rightarrow \infty} \Phi_M(x, y, z; \tau) = \Phi_M(x, y, z). \quad (6.3)$$

C is a constant and the dimension of $C/d\tau$ is [m^{-2}]. With the standard finite difference Fourier implementation scheme, which involves two iteration coordinate levels at coordinate τ and coordinate $\tau + d\tau$, the solution is achieved for a rectangular grid. With $\mathbf{H} = -\nabla \Phi_M$ (\mathbf{H} the magnetic field [A/m]), the induced magnetic field \mathbf{B} [T] is calculated as $\mathbf{B} = \mu_0 \mu \mathbf{H}$ (μ_0 is the magnetic permeability in vacuum ($4\pi \times 10^{-7}$ H/m)). The solution of eq. 6.1 results in the macroscopic induced magnetic field. The induced magnetic field experienced by the nucleus is derived by adding the Lorentz correction ($-\frac{2}{3}\mu_0\chi\mathbf{H}$) to the calculated macroscopic induced magnetic field (see section 4.3).

6.2.3 Correction

Correction of the image distortions was performed in two steps. The first step corrects for the machine imperfections (gradient non-linearity and static magnetic field inhomogeneity), which were determined from sets of multiple slice images of a grid phantom with known geometry (chapter 3). By variation of the direction of the read-out gradient, static field and gradient field errors were determined at the phantom tube positions, from which 3D error maps were inferred by bicubic interpolation. Patient images were corrected using the error maps and taking into account actual gradient directions, strengths, field of view and offsets. The second step corrects for the object related image distortions, viz. the chemical shift and susceptibility induced image distortions. The necessary corrections were determined from the displacements in images, which were acquired with opposite directions of the read-out gradient and which were corrected for machine related static magnetic field inhomogeneity and non-linearity of the gradients. The true position of an image structure is half-way between the two distorted positions in both images. The efficacy of the methods to correct for machine related and object related image distortions was evaluated for landmarks at defined locations, viz. the external landmarks 1, 3, 4, 6, 7 and 9 in the localization frame. The frame coordinate system was related to the coordinate system of the MR image, which was corrected for machine and object related image distortions. The frame coordinates and the corrected image coordinates of the external landmarks 1, 3, 4, 6, 7 and 9 were matched using an algorithm for least squares fitting of two 3D point sets (Arun et al. 1987). The real frame coordinates were thus transformed into image coordinates, which were taken as the true image coordinates. Spatial distortions of external landmarks in uncorrected and corrected images were evaluated with respect to these true image coordinates.

6.3 Results and discussion

6.3.1 Experiments

Reversed gradient images were acquired from 10 patients, of which 3 patients were imaged with the localization frame attached to the base of the patient's headcast. Internal landmark displacements were measured in all patient studies, the displacements of the external landmarks in the frame (1 to 9) in 3 patient studies and the external landmarks attached to the cast at the location of the forehead (10, 11, 12) in 7 patient studies. For this patient set-up and the applied scan protocol the mean spatial image distortions caused by static magnetic field inhomogeneity were systematic, ranging from -2 to 4 mm with a standard deviation of 0.5 mm for the external landmarks and 1 mm for the internal landmarks (figure 6.3a).

6.3.2 Analysis

The image distortions were analyzed with respect to the contributions of the different sources of static magnetic field inhomogeneity for a typical patient imaged in the localization frame.

Machine related static magnetic field inhomogeneity

The machine related static magnetic field inhomogeneity in the mid-sagittal plane was determined from the measurements on a grid phantom. The asterisks in figure 6.3b denote the machine related field errors in ppm (right-hand ordinate) and corresponding spatial distortions in mm (left-hand ordinate) at the locations of the internal and external landmarks.

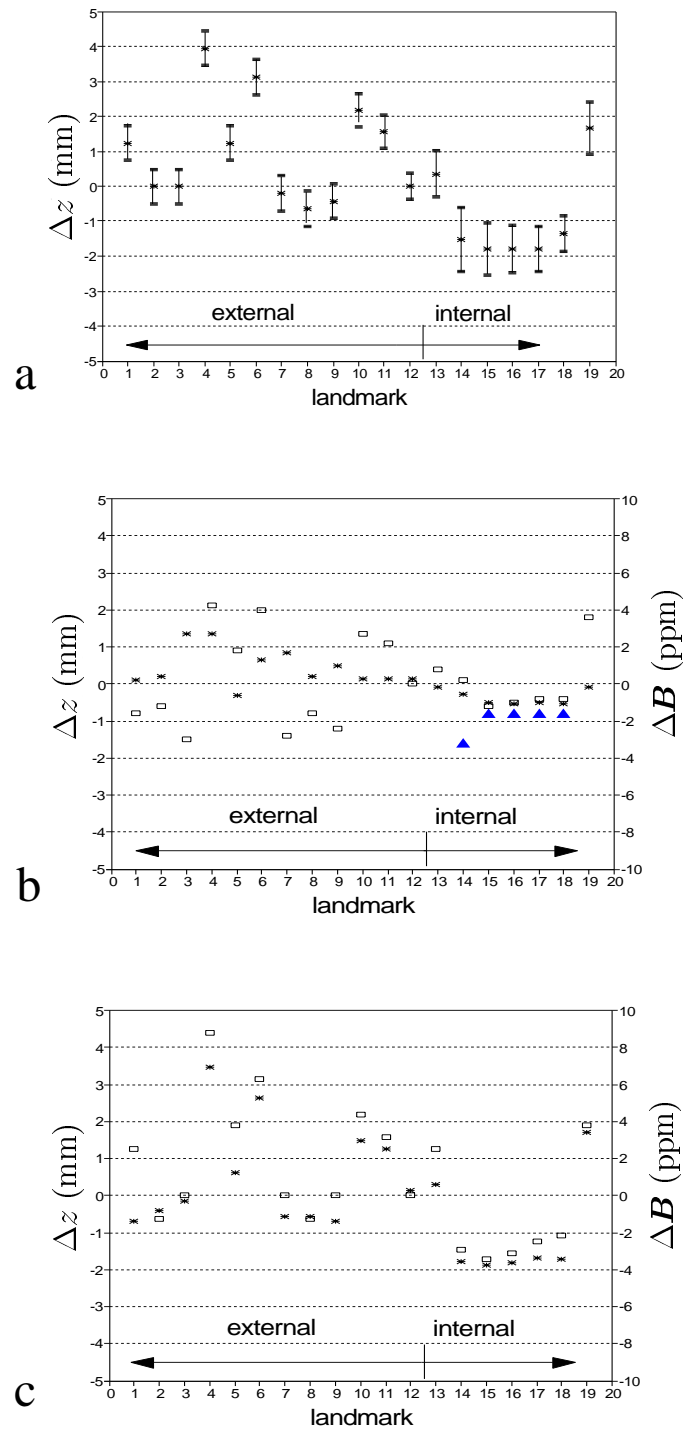


Figure 6.3: a) Spatial image distortions (Δz) in the mid-sagittal plane caused by static magnetic field inhomogeneity according to the reversed read-out gradient experiments on 10 patients (average \pm standard deviation). The read-out gradient strength was 3 mT/m. b) Field inhomogeneity (ΔB) and resulting spatial image distortions (Δz) in the mid-sagittal plane caused by machine related static field inhomogeneity (asterisks), chemical shift (triangles) and susceptibility (rectangles) induced static magnetic field inhomogeneity. Field inhomogeneity is expressed in ppm (right-hand ordinate), corresponding spatial distortions in mm (left-hand ordinate). The read-out gradient strength was 3 mT/m. Analysis for a typical patient. c) Comparison between measured static magnetic field inhomogeneity or corresponding spatial distortions (rectangles) and sum of contributions (asterisks) from machine related static magnetic field inhomogeneity (measurement), chemical shift (literature values) and susceptibility induced static magnetic field inhomogeneity (numerical calculation). Analysis for a typical patient.

In the experiments at 1.5 T with read out gradient strength of 3 mT/m, static magnetic field inhomogeneity results in spatial distortions of 0.5 mm per ppm. Machine related static magnetic field inhomogeneity resulted in mean spatial distortions ranging from -0.5 to 1.5 mm.

The chemical shift effect

In this study, bone marrow containing internal structures were the sphenoid bone and the corpora of the cervical vertebra. The sphenoid bone and the corpora of the cervical vertebra showed different signal intensities and spatial distortions (figures 6.2a and 6.3b). The contribution of chemical shift effects was estimated from values in the literature as follows. In the normal human adult, bone marrow can be divided into yellow (fatty) marrow and red (hematopoietic) marrow (Bloom and Fawcett 1968). The sphenoid bone marrow signal is bright, comparable to subcutaneous fat (figure 6.2a). This suggests yellow bone marrow in the sphenoid bone (Wisner et al. 1985), which results in a chemical shift of -3.2 ppm (triangle for landmark 14 in figure 6.3b). Vertebrae contain red marrow, about 70 % of which is composed of cellular elements containing mostly water protons; the remainder consists of fat, intimately admixed with the cellular elements (Cristy 1981). The admixture of fat and water constituents is such that high fractional volumes of each contribute signal to the image voxel (Wisner et al. 1985), which resulted in about half the chemical shift because of partial volume effects (triangles for landmarks 15 to 18 in figure 6.3b).

Susceptibility induced static magnetic field inhomogeneity

The patient and the localization frame perturbed the applied magnetic field of 1.5 T, which is along the caudo-cranial direction (figure 6.2b). Calculation of the magnetic field revealed that, on average, the field strength in the patient's brain was 0.8 ppm above the applied field of 1.5 T. Spatial landmark distortions were measured with respect to the position of the brain tissue, which showed no displacements in the reversed read-out gradient experiments. Therefore, magnetic field strengths at different locations will be expressed as deviations (in ppm) from the magnetic field strength in the brain tissue. The field strength in the frame proved to be dependent on the orientation of the plates with respect to the main magnetic field. The field perturbation in the posterior and anterior plates, which were parallel to the magnetic field, was about -2 ppm (rectangles for landmarks 1 to 3 and 7 to 9 in figure 6.3b). The field perturbation in the cranial plate, which was perpendicular to the magnetic field, was maximally 4.2 ppm (rectangles for landmarks 4 to 6 in figure 6.3b). The field perturbation at the position of landmark 5 in the middle of the cranial plate was partly canceled by the magnetic field perturbation by the patient's head resulting in a total field deviation of 2 ppm.

The magnetic field around the head resulted in displacements of the tubes attached to the cast of the patient. Depending on the position, susceptibility induced field perturbations ranged from 0 to 3 ppm (rectangles for landmarks 10 to 12 in figure 6.3b).

Also inside the head local susceptibility inhomogeneities lead to magnetic field perturbations, e.g. at the interface between tissue and air cavities like the sinus sphenoidalis. The susceptibility induced field perturbations at the interfaces of the sinus sphenoidalis with the pituitary gland and the brain tissue were respectively 0.8 and 3.6 ppm (rectangles for landmarks 13 and 19 in figure 6.3b). The smaller size of the neck area with respect to the head resulted in a susceptibility induced field perturbation of about -1 ppm at the position of the cervical spine (rectangles for landmarks 15 to 18 in figure 6.3b).

Total static magnetic field inhomogeneity

The analysis of MR image distortions is rather complicated because of the contributions of different sources of magnetic field inhomogeneity apart from distortions by gradient non-linearity. In this study mean spatial image distortions caused by static magnetic field inhomogeneity ranged from -2 to 4 mm. Matching of a mid-sagittal MR image with a lateral simulator film based on bony structures like the corpora of the cervical vertebra could result in a mismatch as large as 6 mm for landmark 4 in the frame (figure 6.3a). For an accurate use of MR images for RTP, it is important to know the image distortions and from what error source they are originating. In this study at 1.5 T with read-out gradient strength of 3 mT/m the respective contributions of machine related, chemical shift and susceptibility induced spatial distortions of landmarks were on the same order, ranging from -2 to 2 mm with only negative values for the chemical shift effect. The observed mean total distortions ranging from -2 to 4 mm could be ascribed to the contributions from machine related, chemical shift and susceptibility induced static magnetic field inhomogeneity. An exception is landmark 1, of which the observed distortion deviated about 2 mm from the expected value (figure 6.3c). This may be explained by errors in calculating the susceptibility induced magnetic field perturbations, since the magnetic field was calculated for the head and neck region instead of the total body.

Our analysis of object related image distortions was based on studies on a 1.5 T MRI scanner with 3 mT/m gradient capability, but the results are more widely of interest. Although nowadays MRI scanners are mostly equipped with 10 mT/m gradients, in clinical practice the read-out gradient is usually operated up to about 3 mT/m in order to have sufficient signal to noise ratio. Furthermore, the object related image distortions as measured in this study can be directly extrapolated to distortions to be expected at different static and gradient field strengths, since they are proportional to the main magnetic field strength and inversely proportional to the read-out gradient strength. In 0.5 T magnetic resonance images acquired with the same read-out gradient strength as applied in this study (3 mT/m), image distortions will be a factor of 3 smaller. At 0.5 T for this patient set-up, distortions caused by static magnetic field inhomogeneity can be reduced to 1.5 mm, which is of the order of the pixel size. However, each system, irrespective of the static field strength or the gradient field strength, should be checked for image distortions caused by gradient non-linearity. In our experience with different MRI scanners, increase of gradient capability does not imply improvement of gradient linearity.

6.3.3 Correction method

The efficacy of the correction method was evaluated for the external landmarks 1, 3, 4, 6, 7 and 9 in the localization frame, since for these landmarks the real geometry is known. Figure 6.4a shows the spatial distortions in the uncorrected mid-sagittal MR images of the three patients which were imaged in the frame. Mean spatial distortions in the y -direction between -3.5 and 0.5 mm were caused by non-linearity of the y -gradient, which was the phase encoding gradient. Spatial distortions in the z -direction were larger, ranging from -4.5 to 3 mm. These distortions were caused by non-linearity of the read-out gradient and machine related and susceptibility induced static magnetic field inhomogeneity. Figure 6.4b shows the results after correction for the machine imperfections. Accuracy in the y -direction was better than 1.3 mm and in the z -direction distortions ranged from -2.5 mm to 3.5 mm, which indicated that susceptibility artifacts had also to be corrected for. Figure 6.4c shows the results after correction for all sources of distortion. Residual errors are on the order of

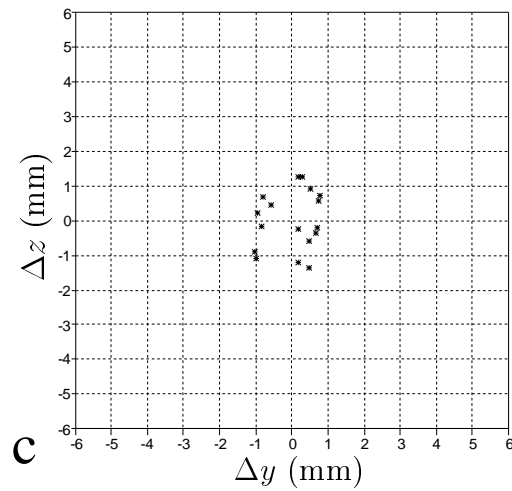
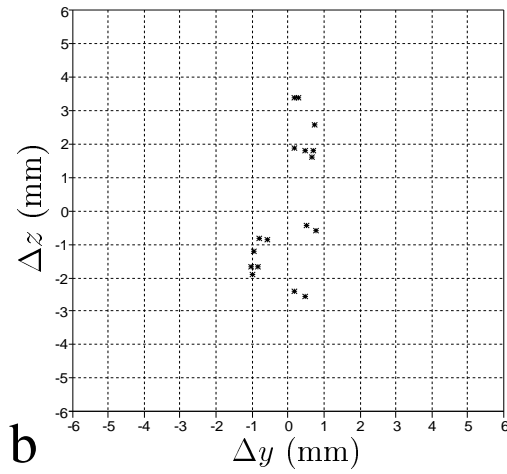
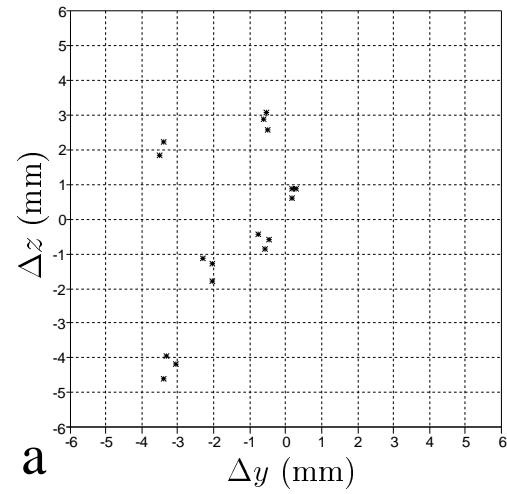


Figure 6.4: Spatial distortions (Δy , Δz) of the external landmarks 1, 3, 4, 6, 7, 9 in the localization frame in MR images of three patient studies. The phase-encoding gradient was directed along the y -axis, the read-out gradient was directed along the z -axis. a) Spatial distortions in uncorrected MR images. b) Spatial distortions in MR images corrected for machine imperfections. c) Spatial distortions in MR images corrected for machine imperfections and susceptibility artifacts.

1.3 mm, which may be explained by the MR image resolution (pixel size is 1.25 mm x 1.25 mm) and inaccuracies in the numerical calculation of the susceptibility induced magnetic field perturbations. In principle, the correction scheme will lead to the same accuracy for the patient structures. This is more difficult to evaluate, since the real geometry is unknown in these studies. In the future, uncorrected and corrected MR datasets will be compared with computerized tomography (CT) datasets for accuracy assessment.

Geometric accuracy is a need if MR images are to be used as the only input for RTP. A different approach is the use of both CT and MRI. These methods rely on CT for geometric accuracy and on MRI for tumour visualization (Van den Elsen 1993; Fraass et al. 1987; Kessler et al. 1991; Kooy et al. 1994; Pelizzari et al. 1989; Schad et al. 1987b). This approach requires matching of both datasets, which theoretically can be better accomplished if MR image distortions have been reduced by pulse sequence optimization or if the distortions have been corrected.

6.4 Conclusions

In this study at 1.5 T with read-out gradient strength of 3 mT/m, machine related and susceptibility induced static magnetic field inhomogeneity were on the same order, resulting in spatial distortions between -2 and 2 mm. Internal structures containing yellow bone marrow (the sphenoid bone) shifted 1.6 mm and structures containing red bone marrow shifted 0.8 mm in the direction opposite to the read-out gradient. Both the patient and the localization frame proved to perturb the magnetic field. The field perturbations were shown to be additive. In total, static magnetic field inhomogeneity led to spatial distortions ranging from -2 to 4 mm in the direction of the read-out gradient. Non-linearity of the gradients resulted in spatial distortions ranging from -3.5 to 0.5 mm. After correction for the machine imperfections and susceptibility artifacts, the geometric accuracy of the landmarks in the localization frame was better than 1.3 mm.

Chapter 7

The influence of respiration induced motion of the kidneys on the accuracy of radiotherapy treatment planning, a magnetic resonance imaging study

This chapter is based on the following publication:

M.A. Moerland, A.C.M. van den Bergh, R. Bhagwandien, W.M. Janssen, C.J.G. Bakker, J.J.W. Lagendijk and J.J. Battermann. The influence of respiration induced motion of the kidneys on the accuracy of radiotherapy treatment planning, a magnetic resonance imaging study. *Radiotherapy and Oncology*, 30:150–154, 1994.

Abstract

A magnetic resonance imaging (MRI) study has been performed to determine the respiration induced motion of the kidneys. Under normal respiration conditions, displacements of the left and right kidney varied from 2 to 24 mm and 4 to 35 mm respectively. Under forced respiration conditions, displacements were larger and ranged from 10 to 66 mm for the left kidney and 10 to 86 mm for the right kidney. The influence of kidney motion on the radiation dose was determined for patients irradiated on the total abdomen for ovarian cancer with shielding of the kidneys during part of the treatment. The kidney motion resulted in a larger fraction of the kidney volume receiving a dose between 20 and 22 Gy.

7.1 Introduction

New imaging techniques like 3D-CT and 3D-MRI are now being evaluated on their potential for radiotherapy treatment planning (Bhagwandien et al. 1992a; Ende et al. 1992; Fraass et al. 1987; Glatstein et al. 1985; Schad et al. 1987a; Schad et al. 1987b; Shuman et al. 1985; TenHaken et al. 1992; Thornton et al. 1992; Toonkel et al. 1988). The application of these imaging techniques allows optimization of treatment plans by the use of non-coplanar beam settings and conformation therapy (Boesecke et al. 1991; Brahme 1988). These techniques lead to treatment volumes which approximate the target volumes as close as possible. In view of this tendency to employ conformation therapy based on treatment planning techniques using static CT and/or MRI instead of dynamic fluoroscopy, knowledge about organ motion is becoming more and more important.

Motion of abdominal organs may result in dose uncertainty near the edge of the treatment field when irradiating e.g. kidney, pancreas or spleen. In the next sections we present an MRI study of respiration induced motion of the kidneys and results of the kidney movement study will be used to determine the influence on the kidney dose in patients irradiated on the total abdomen for ovarian cancer.

7.2 Methods and materials

In 14 volunteers, 6 males and 8 females aging between 26 and 64 years, displacements of the right and left kidney under normal respiration and forced respiration conditions were measured using a 1.5 T MRI scanner (Gyrosan S15, Philips Medical Systems, Best, The Netherlands). Images were acquired using the Fast Field Echo (FFE) sequence, which allows acquisition of one image per breath hold. For the breath hold studies, the parameters which gave optimal contrast in a short measurement time, were a minimum repetition time TR of 37 ms and a pulse angle of 30° . The echo time was chosen 16.1 ms for which water and fat protons have opposed phases. The FFE sequence was an RF spoiled gradient echo sequence, which improves the T_1 image contrast (Van der Meulen et al. 1988). For the motion studies, signal acquisition was triggered on the respiration cycle using a respiration monitor with sensor (Type MR 10, Graseby Medical Ltd, Watford, England) in combination with the scanners triggering device. The FFE sequence was combined with multi-phase imaging.

The procedure started with a transversal multiple slice study to locate both kidneys. The next step was to choose the scan plane for the respiration induced movement studies. The movement of the kidneys predominantly occurred in a tilted coronal plane through the longitudinal axis of the kidneys, which can be explained by the fact that the kidneys move

Table 7.1: MR imaging protocol for the study of movement of the kidneys during the respiration cycle

Scan 1: Transversal multiple slice study (5 slices), breath holding, manual start. FFE, $TR = 37$ ms, $TE = 16.1$ ms, pulse angle 30° , resolution 256×256 , slice thickness 20 mm, 2 measurements, reduced acquisition time (80%), T_1 contrast enhancement. Scan time 5×18 s.

Scan 2: Sagittal scouts, breath holding, manual start, 2 slices. FFE, $TR = 37$ ms, $TE = 16.1$ ms, pulse angle 30° , resolution 256×256 , slice thickness 20 mm, 2 measurements, reduced acquisition time (80%), T_1 contrast enhancement. Scan time 2×18 s.

Scan 3: Respiration triggered multi-phase study, 16 phases, single angular coronal slice through both kidneys. FFE, TR typical 300 ms (16 phases during a respiration cycle of 5 s), $TE = 16.1$ ms, pulse angle 30° , resolution 128×128 , slice thickness 20 mm, 2 measurements, reduced acquisition time (60%), T_1 contrast enhancement. Scan time typical 13 minutes.

Scan 4: Forced inspiration study, breath holding, manual start, single angular coronal slice through both kidneys. FFE, $TR = 37$ ms, $TE = 16.1$ ms, pulse angle 30° , resolution 256×256 , slice thickness 20 mm, 2 measurements, reduced acquisition time (80%), T_1 contrast enhancement. Scan time 18 s.

Scan 5: Forced expiration study, breath holding, manual start, single angular coronal slice through both kidneys. FFE, $TR = 37$ ms, $TE = 16.1$ ms, pulse angle 30° , resolution 256×256 , slice thickness 20 mm, 2 measurements, reduced acquisition time (80%), T_1 contrast enhancement. Scan time 18 s.

along the psoas muscles. The exact angle of this coronal plane was determined individually for each volunteer from sagittal scouts through both kidneys. After determination of the plane of motion, the respiration triggered multi-phase study was started. These images were acquired with a lower resolution to reduce imaging time. As shown in table 7.1, a respiration triggered multi-phase study took about 13 minutes depending on the respiration frequency. Divided over the respiration cycle, 16 images were acquired which led to a repetition time of typically 300 ms. The series of multi-phase images were displayed as a movie which helped to interpret the movement of the kidneys. After the respiration triggered multi-phase study under normal respiration conditions, forced inspiration and expiration studies were performed. These images were acquired under breath hold conditions with the usual image resolution. From these images extreme displacements of the kidneys were determined. In this study the displacement is defined as the total movement of the kidney between the end of inspiration and the end of expiration. Displacements were measured by subtracting kidney upper lobe coordinates acquired from inspiration and expiration images. Since the kidneys lie on both sides of the vertebral column, the vertebrae can be used as anatomical reference points for absolute localization of the kidneys, which is e.g. relevant for the positioning of shielding blocks.

Results of the kidney movement study were used to determine the influence on the kidney dose in patients irradiated on the total abdomen for ovarian cancer. At our department these patients are treated with opposing fields (antero-posterior and postero-anterior). The target

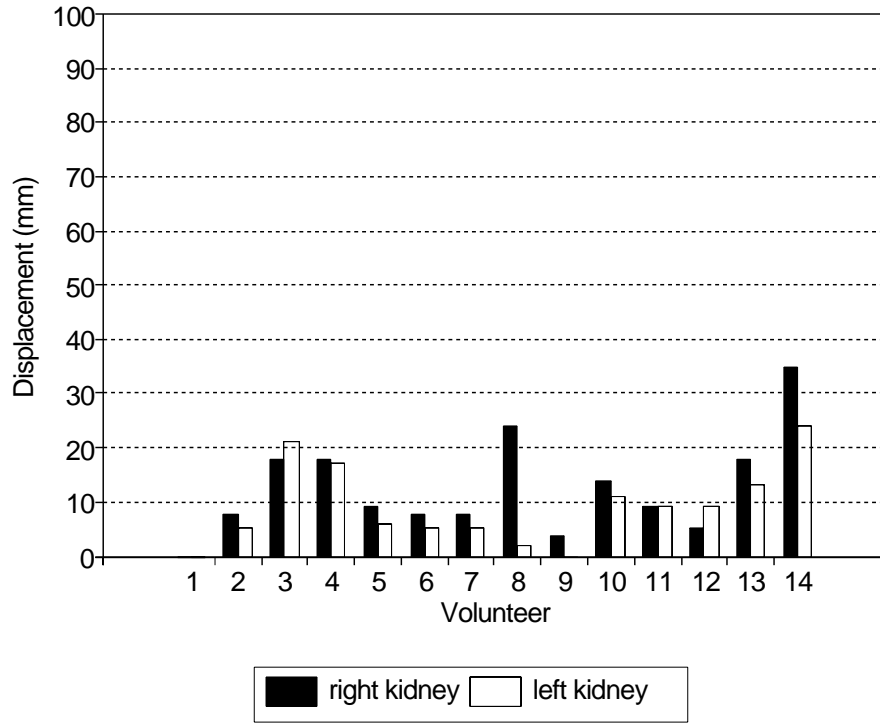


Figure 7.1: Displacements of the right and left kidney at normal respiration.

dose at the ICRU specification point is 25 Gy in fractions of 1.25 Gy, 5 fractions a week. After 15 Gy target dose the kidneys are shielded in the PA field. In most cases the size of the block is chosen such that the kidney is just covered and the position of the block is an average between the inspiration and expiration position, guided by Intra Venous Urography (I.V.U.) images. The kidney irradiation dose was determined using a radiotherapy treatment planning system (Plato RTS, Nucletron International B.V., Veenendaal, The Netherlands). As the treatment planning system cannot handle motion of external or internal contours, the kidney motion was simulated by moving the shielding block relative to the kidney. The positions of the shielding block and the weights of the corresponding PA beams were determined from a typical multi-phase study. The kidney motion was digitized into 8 positions with the origin defined as the average position between inspiration and expiration. For each position the relative time interval was determined, which gave the weights of the corresponding postero-anterior (PA) beams in the treatment plan.

7.3 Results

Under normal respiration conditions displacements of the left and right kidney varied from 2 to 24 mm and 4 to 35 mm respectively (figure 7.1). In this study we were not able to evaluate the normal respiration induced motions of 3 out of 28 kidneys because of poor image quality of the multi-phase triggered studies in question. The multi-phase triggered studies revealed kidney motion during the normal respiration cycle. The first image of the motion study was within 10 ms of the start of inspiration and the last image was as close as possible to the end of the respiration cycle, typically within 200 ms. In general, kidney motion could roughly be characterized by 4 phases: i) motion during inspiration, ii) rest at the end of inspiration, iii)

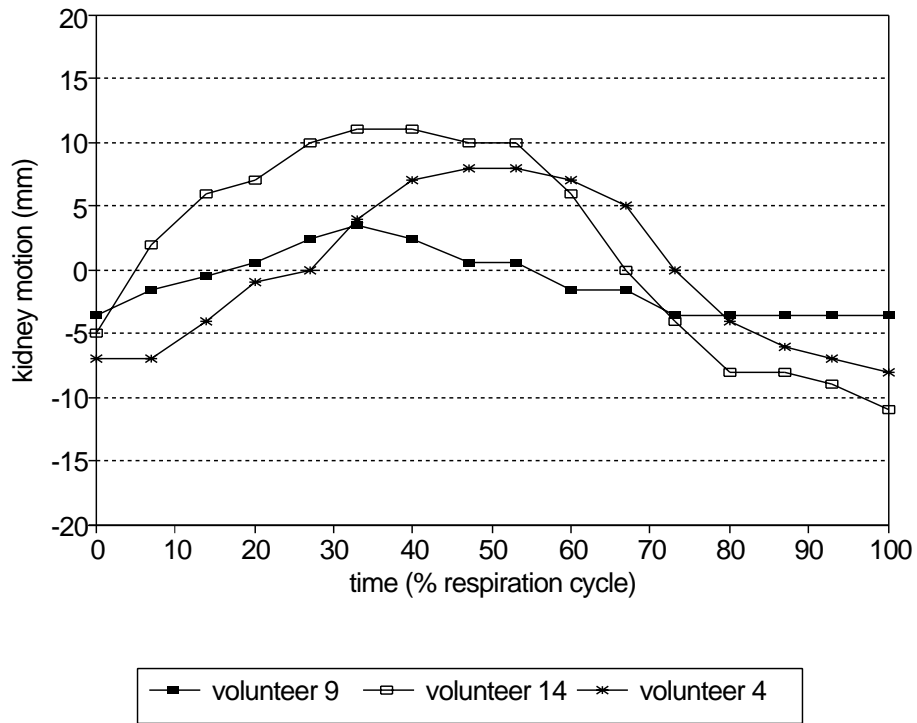


Figure 7.2: Kidney motion during normal respiration.

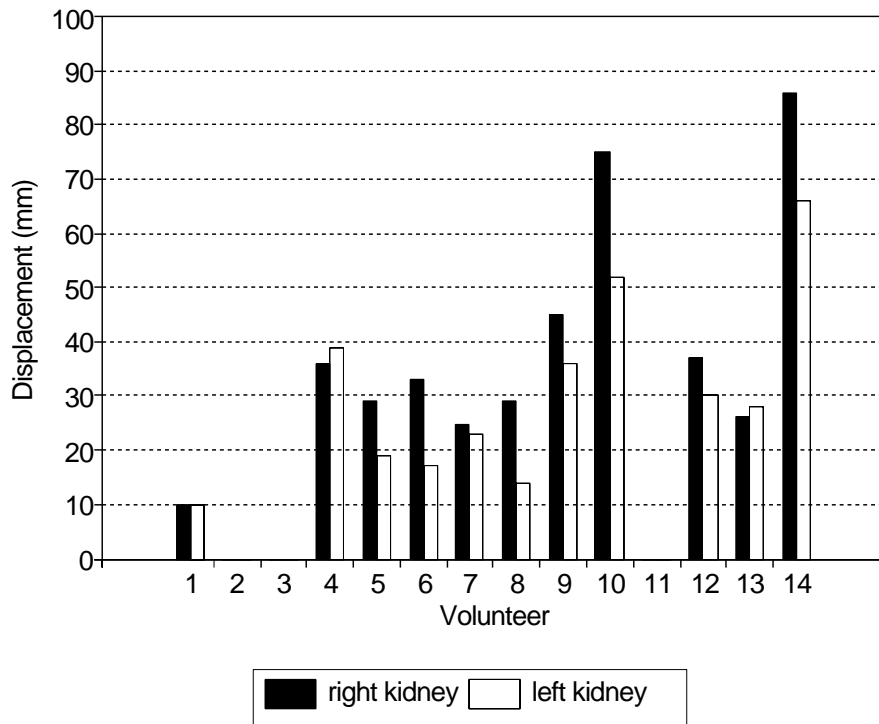


Figure 7.3: Displacements of the right and left kidney at forced respiration.

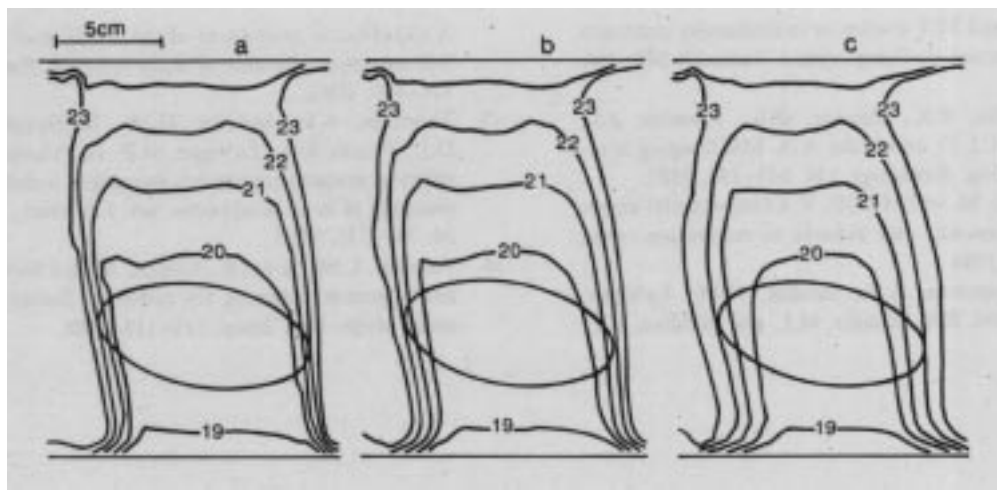


Figure 7.4: The influence of respiration induced motion on the dose distribution (in Gy) in a sagittal cross section through the kidney. a) dose distribution without kidney motion, b) dose distribution based on a volunteer study with a moderate kidney displacement of 14 mm, c) dose distribution based on displacement of the kidney of 28 mm.

motion during expiration and iv) rest at the end of expiration. Examples of relatively small (volunteer 9), moderate (volunteer 4) and large (volunteer 14) respiration induced kidney motion are given in figure 7.2 with the origin defined as the average kidney position between inspiration and expiration. As expected, under forced respiration conditions displacements were larger and ranged from 10 to 66 mm for the left kidney and 10 to 86 mm for the right kidney (figure 7.3). In 3 cases forced respiration studies were not performed.

The influence of the kidney motion is illustrated in figure 7.4. Three dose distributions were calculated, one distribution without and two distributions taking into account the kidney motion. The distribution in figure 7.4b is based on the moderate kidney motion of volunteer 4, whereas the distribution in figure 7.4c is based on kidney displacements, which were supposed to be twice as large. Without movement of the kidney and a shielding block, which just covers the kidney, the irradiation dose does not exceed 20 Gy apart from a small fraction of the kidney volume, which receives a dose between 20 and 22 Gy (figure 7.4a). The respiration induced motion of the kidneys results in a larger fraction of the kidney volume receiving a dose between 20 and 22 Gy and this fraction increases with the amplitude of the kidney motion (figures 7.4b and c).

7.4 Discussion

The proposed MR imaging protocol is valid if the organ of interest mainly moves in one plane. If the movement is not restricted to one plane, 3D image acquisitions divided over the respiration cycle should be performed. However, the extension to 3D image acquisition is very time consuming and only feasible with ultra fast imaging techniques. In case of the kidneys, single slice studies were adequate to determine the respiration induced movement. In 10 to 15 minutes acquisition time a respiration triggered multi-phase study was performed resulting in 16 low resolution images divided over the respiration cycle. The image quality was sufficient to get insight into the movement of the kidneys. Once general knowledge about organ movement is gathered static MR imaging of the inspiration and expiration position of the organ in an individual patient might be sufficient for Radiotherapy Treatment Planning

purposes like determination of field margins, shielding blocks, beam angles, etc. These static high resolution images take only about 20 s acquisition time using a gradient echo sequence.

In this study on 14 volunteers large interindividual variations were observed. Our limited amount of data does not allow a search for correlations between kidney displacement and e.g. sex, age, body length, body weight or pathology. In the literature such correlation studies are scarce, one of which showed that kidney displacements were larger in subjects under 60 years than in those over 60 years (Suramo et al. 1984). To our opinion correlation studies are relevant to get a general insight in the motion of an organ, but for an individual patient an individual organ motion study will still be mandatory.

For a typical kidney motion as in figure 7.4b a shielding block, which just covers the kidney at the average position between inspiration and expiration, seems adequate. For larger displacements, as in volunteer 14, it might be appropriate to cover the kidney with some margin at the cost of shielding more of the target volume. The placement of kidney shielding blocks should be based on images acquired under normal respiration conditions. Forced inspiration or forced expiration X-ray I.V.U. or CT images are not appropriate.

Motion of an organ, which is closely covered by a shielding block or by the treatment field as in conformation therapy, results in widening of the penumbra near the edge of the organ. Widening of the penumbra may also be caused by patient movement and/or errors in radiation field alignment (Huizenga et al. 1988; Meertens 1989). Therefore individual organ motion studies and position verification by portal imaging are indicated in accurate radiotherapy treatment planning.

Individual organ motion studies are a means to individualize margins, so that the individual patient can be treated to a higher dose because of more tight margins. An even more sophisticated approach would be motion gated radiotherapy, e.g. respiration gated radiotherapy, if an organ at risk or the target moves with respiration (Kubo and Hill 1996; Ohara et al. 1989).

Chapter 8

Evaluation of permanent I-125 prostate implants using radiography and magnetic resonance imaging

This chapter is based on the following publication:

M.A. Moerland, H.K. Wijrdeman, R. Beersma, C.J.G. Bakker and J.J. Battermann. Evaluation of permanent I-125 prostate implants using radiography and magnetic resonance imaging. *International Journal Radiation Oncology Biology Physics*, submitted.

Abstract

The aim of this study is the evaluation of permanent I-125 prostate implants using radiography and magnetic resonance imaging (MRI).

Twenty-one patients underwent radiography on the simulator and MRI within 3 days after implantation of the I-125 seeds. Isocentric radiographs were used for reconstruction of the seed distribution, after which registration with the seed induced signal voids on MRI provided the seed positions in relation to the prostate. The prostate was contoured on the transversal magnetic resonance images and dose volume histograms were computed to evaluate the implants.

The validity of the ellipsoidal prostate volume approximation, as applied in pre-implant dose calculation, was assessed by comparison of ellipsoidal volumes given by prostate width, height and length and prostate volumes obtained by a slice by slice contouring method, both on post-implant MRI.

Prostate volume changes due to post-implant prostate swelling, were assessed from radiographs taken at 3 days and 1 month after the implantation.

The seeds were readily identified on T_1 -weighted spin echo images and matched with the seed distribution reconstructed from the isocentric radiographs. The matching error, averaged over twenty-one patients, amounted 1.8 ± 0.4 mm (mean \pm standard deviation).

The fractions of the prostate volumes receiving the prescribed matched peripheral dose (MPD) ranged from 32 to 71% (mean \pm standard deviation: $60 \pm 10\%$).

Prostate volumes, obtained by the contouring method on post-implant MRI, were a factor 1.5 ± 0.3 larger than the ellipsoidal volumes given by the prostate dimensions on post-implant MRI.

Prostate volumes 3 days after the implantation were a factor 1.3 ± 0.2 larger than the prostate volumes 1 month after the implantation.

Registration of the reconstructed seed distribution and the MR images showed inaccuracies in seed placement, e.g. two or more seeds clustering together or seeds outside the prostate.

Registration of the reconstructed seed distribution and the MR images enabled evaluation of target coverage, which amounted $60 \pm 10\%$. The discrepancy between prescribed dose and realized dose was caused by underestimation of the pre-implant prostate volume due to the ellipsoidal approximation, post-implant prostate swelling at the time of evaluation and inaccuracies in seed placement.

8.1 Introduction

Localized prostatic cancer is treated by radical prostatectomy, external beam irradiation or a permanent implant with I-125 seeds (Blasko et al. 1987; Whitmore Jr. et al. 1972). Permanent implants in general are applied for small tumours (T1-T2) with a good to moderate histological differentiation. At our institute, the technique used is a transrectal ultrasound (TRUS) guided transperineal implantation technique (Holm et al. 1983). We aim for a uniform seed distribution with 1 cm seed spacing such that the initial dose rate surface of 7.8 cGy/h encompasses the prostate resulting in an accumulated dose of 160 Gy. Since accurate seed placement is hampered by possible deformation and swelling of the prostate caused by inserting the needles and by seed migration during and after implantation, post-implant dosimetric evaluation is an important part of the process. It provides the necessary feed-back to ensure the quality of the implant procedure and to evaluate the clinical outcome (Feygelman et al. 1995). Up till now, at our institute, the seed distributions were evaluated

from isocentric radiographs, which do not show the relationship with the prostate. Information on the position of the seeds relative to the prostate can be gained by ultrasound, computerized tomography (CT) or magnetic resonance imaging (MRI) examinations. On ultrasound, the seeds give rise to artifacts, which hamper evaluation of the prostate and the seed distribution. A CT-based evaluation method for permanent prostate implants has been developed by Roy et al. 1993. Seed positions and prostate contours were depicted at axial CT scans. Grimm et al. 1994 remarked that CT images frequently overestimate the size of the prostate in the most anterior and lateral areas, because the periprostatic venous plexus and the periprostatic fat pad are frequently not well distinguished from the prostate gland itself. The aim of this study is the evaluation of permanent I-125 prostate implants using radiography and magnetic resonance imaging. We employ the excellent soft tissue imaging capabilities of MRI to delineate the prostate (Stark and Bradley 1992) and the high resolution of isocentric radiographs to identify the seeds. Pertinent issues that were investigated, include i) reconstruction of the seed distribution in relation to the prostate, ii) implant evaluation by dose volume histogram computations, iii) the validity of the ellipsoidal target volume approximation, and iv) estimation of post-implant prostate swelling.

8.2 Methods and materials

8.2.1 Pre-implant dose calculation

The patients undergo digital rectal examination (DRE) and transrectal ultrasound to obtain an estimate of the prostate volume, which is required to determine the number of seeds for the implant. The prostate volume is estimated as an ellipsoidal volume, which is given by $V = (\pi/6)abc$, where a , b and c are the orthogonal dimensions of the prostate obtained by TRUS. At our institute, prostates with volumes not exceeding 40 cm^3 are regarded to be eligible for a permanent implant. Typically, about 40 I-125 seeds (Amersham International, type 6711, apparent activity 0.57 mCi, 4.5 mm long, 0.8 mm diameter) are implanted with 1 cm spacing giving a planned uniform seed density of 1 seed/cm^3 . This approach follows the guidelines by Anderson 1976, giving a matched peripheral dose (MPD) of 160 Gy. The MPD is defined as the dose for which the computed isodose volume equals the volume of an ellipsoid having the same dimensions as the target volume. The dosimetry of sources used in interstitial brachytherapy has been the subject of considerable research in recent years. Also for I-125 seeds, revision of basic dosimetry data, including dose rate constants, radial dose functions and anisotropy functions has been advocated. In our study, dose calculation was based on point source approximations with a 4π averaged anisotropy factor and on the dosimetric constants supplied by Ling et al. 1983. Application of the newly proposed dosimetric constants by Nath et al. 1995 (AAPM Task Group 43) and correction for seed anisotropy would result in 25 % lower calculated doses.

8.2.2 Reconstruction of the seed distribution in relation to the prostate

Although the I-125 seeds were generally well depicted on MRI, identification of all seeds of an implant proved to be difficult. In some cases differentiation between seeds in the periphery of the prostate and blood vessels in the prostate capsule was difficult. Also seeds located close to or in the rectal wall, which may occur occasionally, were not easily detected. It also happened that two or more seeds clustered, which presented on MRI as one large area of

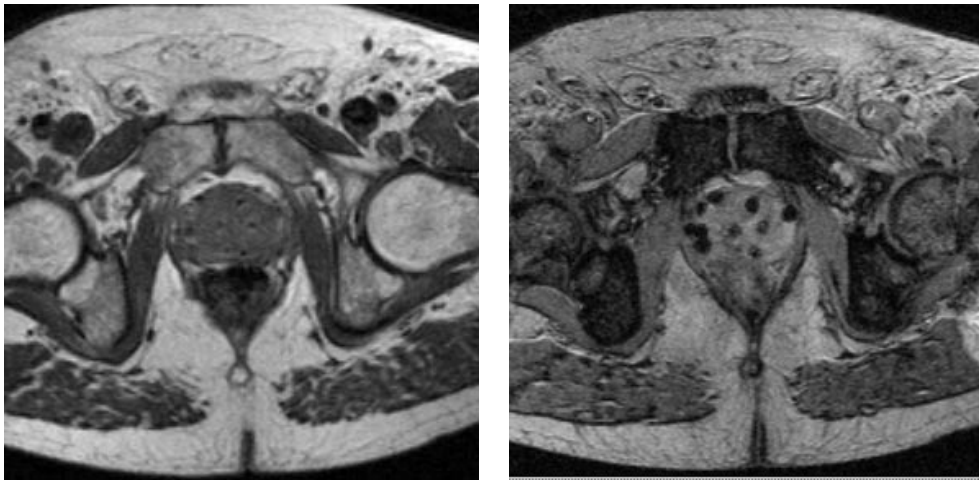


Figure 8.1: Transversal spin echo (left) and gradient echo (right) image of the prostate. I-125 seeds are depicted as signal voids.

signal void, from which the number of seeds could not be deduced. For these reasons we have not chosen for seed reconstruction based on MRI alone. Instead, we have developed a more redundant method by combining conventional radiography and MRI. Seed identification is optimal on conventional radiography, visualization of the prostate is optimal on MRI.

Visualization of the seeds and the prostate

Since radiography does not depict the prostate, we attempt to use MRI for depicting the prostate and the seed distribution. In a pilot study, we employed spin echo (SE) and gradient echo (GE) pulse sequences and varied parameters (viz. the repetition time TR , the echo time TE and the read-out gradient strength) to achieve adequate visualization of the prostate and the seed distribution. Variation of the read-out gradient strength influenced the size of the seed induced signal voids in spin echo images and even more pronounced in gradient echo images. As also remarked by Roy et al. 1993, for the transperineal needle-guided implant the seeds tend to align along the longitudinal axis within $\pm 30^\circ$, so that transversal images should depict the transversal cross sections of the seeds. On the transversal T_1 -weighted spin echo images acquired with a 1.4 mT/m read-out gradient, the seeds with a physical 0.8 mm diameter cross section presented as more or less circular signal voids with a diameter of about 2 mm providing adequate visualization of the seeds without deteriorating visualization of the prostate (see figure 8.1). On the transversal gradient echo images acquired with a 2.9 mT/m read-out gradient, the seeds presented as signal voids with a diameter of about 6 mm. Two seeds clustered together presented as a signal void with a diameter of about 10 mm. These findings led to the conclusion that the signal voids were caused by disturbance of the local magnetic field homogeneity around the seeds (Bakker et al. 1994; Bhagwandien 1994). In our experience, the prostate and the seeds were best depicted on T_1 -weighted spin echo images with a relatively weak read-out gradient (1.4 mT/m), but in some cases gradient echo images aided in identifying the seeds, e.g. when differentiation between a seed in the periphery of the prostate and a blood vessel in the prostate capsule was difficult on a spin echo image. In those cases, the larger area of signal loss on the gradient echo image reveals the seed. Visualization of the prostate was worse on gradient echo images compared to spin echo images because of the low soft tissue contrast of gradient echo images (see figure 8.1).

Spatial distortions of the seeds were determined by means of reversed read-out gradient

experiments. Since static magnetic field inhomogeneity results in spatial distortions in the direction of the read-out gradient, the true position of a seed is half-way between the two distorted positions in the MR image acquired with a positive read-out gradient and the MR image acquired with a negative read-out gradient (Bakker et al. 1992; Chang and Fitzpatrick 1992; Moerland et al. 1995). The seeds were shown to shift ≈ 2 mm in the postero-anterior direction, if the images were acquired using a spin echo pulse sequence with a 1.4 mT/m read-out gradient in the postero-anterior direction. This systematic spatial distortion of the seed positions in the image was corrected for in the image registration and the histogram computation. Since spatial distortions are inversely proportional to gradient strength, the slice selection gradient was chosen to be maximal (3 mT/m), so that distortions in the slice direction were smaller than 0.5 mm and neglected.

Registration of reconstructed seed distribution and MR images

An evaluation method was developed, which is based on registration of the seed distribution reconstructed from the radiographs and the MR images. Patients undergo radiography and MR scanning within 3 days after implantation. Isocentric, antero-posterior (AP) and lateral radiographs are acquired on the simulator. The seed coordinates are reconstructed on the conventional manner from a pair of isocentric radiographs. The reconstructed seed distributions are verified on the antero-posterior and lateral radiographs. Patients undergo MR scanning on a flat table top in order to have reproducible patient positioning between MR scanning and radiography. Sets of transversal spin echo and gradient echo images of the prostate are acquired with 4 mm slice thickness and 1 mm slice gap. Other parameters include: $TR \approx 800$ ms, $TE = 30$ ms, read-out gradient = 1.4 mT/m (SE), 2.9 mT/m (GE), $NEX = 2$, matrix = 256x256, number of slices ≈ 15 , FOV = 350 mm, magnitude reconstruction. Registration of the reconstructed seed distribution with the MR images provides the seed positions relative to the prostate. We use the Application Visualisation System (AVS) package (Advanced Visual Systems Inc., USA) for image processing. The reconstructed seed positions and the stack of transversal MR spin echo images of a patient are read into AVS. After scaling of the MR dataset to the real size seed distribution, corresponding seeds in the dataset of reconstructed seed positions and signal voids in the MR images are interactively identified. The respective coordinates of the identified seeds are filed, after which the two sets of coordinates are matched using an algorithm for least squares fitting of two 3D point sets (Arun et al. 1987). The resulting rotation and translation matrices provide the registration between the reconstructed seed positions and the MR dataset. Generally, a total of about ten corresponding seeds, distributed over a cranial, central and caudal transversal slice through the prostate, is considered to be adequate for matching. The applied matching algorithm provides an estimate of the matching error averaged over the seeds. After rotation and translation of the reconstructed dataset, the registration is interactively checked for all seeds using AVS.

8.2.3 Implant evaluation by dose volume histogram computation

For the purpose of treatment evaluation in terms of coverage, the prostate is contoured on each transversal MR slice by a radiation oncologist using AVS. The prostate volume serves as a mask for the dose volume histogram computation. The dose to each 1 mm x 1 mm x 1 mm voxel within a 10 cm x 10 cm x 10 cm volume is calculated. Dose calculation is based on the seed distribution as reconstructed from the isocentric radiographs. Thus, the diameter

size of the seed induced signal voids on MRI has no direct effect on the accuracy of dose calculation. The effect on the accuracy of the evaluation method is minimized by choosing about ten corresponding reconstructed seeds and the centres of the signal voids to match the reconstructed seed distribution and the MR images. The dose distribution is analyzed by counting the number of prostate voxels within a certain initial dose rate interval. We use 200 dose rate intervals ranging from 0 to 40 cGy/h (accumulated dose ranging from 0 to 820 Gy, the latter being more than five times the prescribed dose) and generate cumulative histograms showing the fraction of the prostate volume as a function of initial dose rate level.

8.2.4 The validity of the ellipsoidal target volume approximation

As mentioned above, the prostate is contoured on each transversal slice of the MR dataset which is acquired within three days after the implantation. Analogous to the TRUS ellipsoidal volume approximation method, prostate width and height are obtained from the largest prostate contour on the post-implant MRI. The prostate length is derived from the number of slices on which the prostate is depicted and the slice to slice distance. Ellipsoidal volumes thus given by prostate dimensions are compared to prostate volumes obtained by the slice by slice contouring method, both on post-implant MRI.

8.2.5 Estimation of post-implant prostate swelling

Post-implant prostate swelling was estimated from antero-posterior (AP) radiographs, which were obtained at 3 days and 1 month after implantation to check for any loss of I-125 seeds. In most cases, these radiographs were acquired under comparable geometry conditions, i.e. same magnification factor and projection angle, so that any prostate swelling could be estimated from shrinkage of the implant in the first month after implantation. The right-left and caudo-cranial dimensions of the implant were measured on the successive radiographs. The antero-posterior dimension was supposed to change as much as the average change of the right-left and caudo-cranial dimensions.

8.3 Results and discussion

8.3.1 Implant evaluation

Twenty-one patients, who were implanted between January and September 1994, underwent MR scanning. The seeds were readily identified and matched with the seed distribution reconstructed from the radiographs. The matching error, averaged over twenty-one patients, amounted 1.8 ± 0.4 mm (mean \pm standard deviation). Table 8.1 shows several parameters related to the implants, which are sorted on the number of implanted seeds. The number of seeds to be implanted was chosen on guidance of DRE and TRUS and ranged from 34 to 47, which resulted in volumes ranging from 29 to 42 cm³ receiving a prescribed dose of at least 160 Gy. The two last columns of table 8.1 show that target coverage did not correlate with the number of implanted seeds. The fractions of the prostate volumes receiving the prescribed dose ranged from 32 to 71 % (mean \pm standard deviation: 60 ± 10 %). The isodose levels, for which 99 % target coverage was achieved, ranged from 21 to 70 Gy (mean \pm standard deviation: 46 ± 13 Gy).

The 160 Gy prescription dose is based on the MPD approach, with the MPD regarded as the dose representative of that in the target periphery. On average, the realized volumes

receiving at least 160 Gy were of the order of the ellipsoidal volumes given by prostate dimensions obtained from pre-implant TRUS (see table 8.2, columns 2 and 4). However, according to our MRI-based evaluation method, the realized peripheral dose values (providing 99 % target coverage) were, on average, 3.5 times smaller than the 160 Gy MPD (see table 8.1). Roy et al. 1993 developed a CT-based evaluation method and found that the realized peripheral dose values were on average 2 times smaller than the MPD values, which were calculated for ellipsoidal volumes given by prostate dimensions obtained from CT images. They concluded that the disparity between MPD and the minimum target dose is due to the fact that a portion of the target is protruding from the ellipsoidal approximation and receiving a considerably smaller dose than the MPD. Thus, errors in prostate volume determination may attribute to the discrepancy between planned MPD and realized peripheral dose. In our evaluation method, pre-implant dose calculation is based on an ellipsoidal volume approximation obtained by TRUS, whereas post-implant evaluation is based on a slice by slice MRI contouring method. Post-implant prostate volumes according to MRI were on average a factor 1.9 larger than the pre-implant volumes according to TRUS (see table 8.2, column 6). Apart from errors in prostate volume determination, inaccuracies in seed placement may attribute to the discrepancy between planned MPD and realized peripheral dose.

8.3.2 The validity of the ellipsoidal target volume approximation

Prostate volumes obtained by the contouring method on post-implant MRI were a factor 1.5 ± 0.3 larger than the ellipsoidal volumes given by prostate dimensions obtained from post-implant MRI, or the ellipsoidal approximation resulted in 33 % prostate volume underestimation (see table 8.2, column 7). Rahmouni et al. 1992 compared prostate volumes determined by TRUS ellipsoidal approximation and MRI contouring method with volumes derived from the weight of freshly excised specimen. They found that MRI better predicted the prostate volumes. The TRUS ellipsoidal approximation led to prostate volume underestimations of about 36 %, whereas the MRI contouring method led to underestimations of about 5 %.

8.3.3 Post-implant prostate swelling

The post-implant prostate swelling could be evaluated on the radiographs, originally acquired to check for any loss of I-125 seeds, of twelve patients. We found that prostate volumes 3 days after implantation were a factor 1.3 ± 0.2 (mean \pm standard deviation) larger than the prostate volumes 1 month after implantation. Post-implant prostate swelling and the volume underestimations by the ellipsoidal approximation accounted for the total discrepancy between the pre-implant TRUS volumes and the post-implant MRI volumes by a factor of 1.9 ± 0.6 (see table 8.2, columns 6, 7 and 8).

8.3.4 Accuracy of seed placement

In our study, post-implant radiography and MRI showed that in most cases the planned uniform seed distribution was only achieved to some degree. Figure 8.2 shows an implant with a rather good seed distribution resulting in a calculated 68 % target coverage, whereas figure 8.3 shows an implant with a target coverage of only 32 % due to placement of too many seeds in the caudal part of the prostate. In some cases, post-implant radiography showed two or more seeds clustering together. The difficulty of achieving a uniform seed

Table 8.1: Parameters of the implants: number of implanted seeds, volume receiving a dose of 160 Gy, dose levels, for which 99 % target coverage was achieved and fraction of prostate receiving a dose of 160 Gy. The last rows give the mean and the standard deviation of the dose levels, for which 99 % target coverage was achieved and the mean and the standard deviation of the fractions of the prostates receiving a dose of 160 Gy.

patient	# seeds	volume at 160 Gy (cm ³)	dose level for 99 % target coverage (Gy)	% prostate volume at 160 Gy
1	34	29	47	61
2	36	32	45	68
3	36	29	21	32
4	36	31	70	67
5	37	32	62	71
6	37	32	57	59
7	37	33	70	67
8	38	35	41	46
9	38	34	43	60
10	38	35	53	57
11	39	34	53	60
12	39	37	55	58
13	40	31	33	42
14	40	33	37	56
15	40	34	57	68
16	40	34	41	53
17	40	37	33	48
18	40	34	31	44
19	42	41	37	55
20	43	39	33	54
21	47	42	49	68
mean			46	60
std			13	10

distribution is acknowledged by several authors (Dawson et al. 1994; Grimm et al. 1994; Van 't Riet et al. 1992; Vijverberg et al. 1993). Seed placement may be inaccurate due to deformation of the prostate caused by inserting the needles and by seed migration during and after implantation. Grimm et al. 1994 used AP fluoroscopy at the conclusion of the implantation procedure to aid in identifying apparent cold spots. If necessary, extra seeds were implanted in cold spots.

8.3.5 Reflections on adjustment of implantation technique and dose prescription

The discrepancy between the MPD approach and the post-implant MRI evaluation suggests that the ellipsoidal volume approximation is inaccurate and that pre-planning should be based on slice-by-slice imaging of the prostate. For two patients (2 and 3) we calculated the dose volume histograms and target coverage in case of uniform seed distribution with 1 cm

Table 8.2: Volume receiving a dose of 160 Gy, pre-implant prostate volume determined by DRE, pre-implant prostate volume determined by TRUS (ellipsoidal approximation), post-implant prostate volume determined by MRI (contouring method), ratio of prostate volume determined by contouring method on post-implant MRI and prostate volume by TRUS ellipsoidal approximation, ratio of prostate volume determined by contouring method and ellipsoidal prostate volume on post-implant MRI, ratio of implant volume at 3 days and volume at 1 month after implantation on radiographs. The last rows give the mean values and the standard deviations.

patient	volume at 160 Gy (cm ³)	V_{DRE} (cm ³)	V_{TRUS} (cm ³)	V_{MRI} (cm ³)	$\frac{V_{MRI}}{V_{TRUS}}$	$\frac{V_{cont}}{V_{ellips}}$	$\frac{V_{at\ 3\ days}}{V_{at\ 1\ month}}$
1	29	27	16	39	2.4	1.8	1.0
2	32	25	15	36	2.4	1.1	n.a.
3	29	35	30	55	1.8	1.6	1.5
4	31	n.a.	13	41	3.2	1.7	n.a.
5	32	25	20	39	2.0	2.1	n.a.
6	32	30	23	45	2.0	1.4	n.a.
7	33	25	26	35	1.3	1.5	1.2
8	35	35	33	46	1.4	1.5	1.3
9	34	25	20	42	2.1	1.4	n.a.
10	35	25	22	57	2.6	1.0	1.4
11	34	30	18	25	1.4	0.9	n.a.
12	37	20	12	41	3.4	1.5	1.8
13	31	36	35	63	1.8	1.4	1.1
14	33	33	31	47	1.5	1.5	1.4
15	34	20	n.a.	38	n.a.	1.6	1.2
16	34	n.a.	25	42	1.7	1.3	n.a.
17	37	40	40	69	1.7	1.3	1.1
18	34	30	39	50	1.3	1.4	1.2
19	41	37	40	58	1.5	1.4	n.a.
20	39	32	35	43	1.2	1.3	n.a.
21	42	35	33	25	0.8	2.0	1.1
mean	34	30	26	45	1.9	1.5	1.3
std	3	6	9	11	0.6	0.3	0.2

n.a. = not available

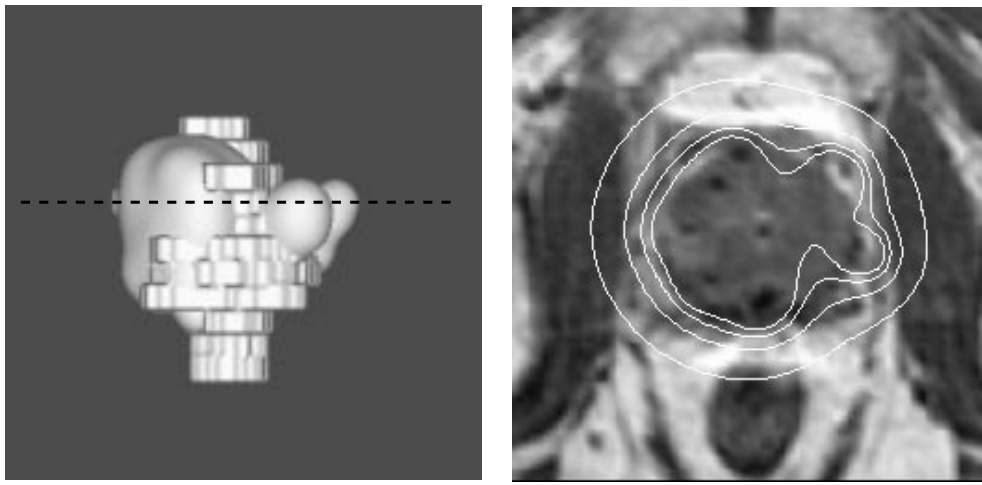


Figure 8.2: Prostate implant with a target coverage of 68 %. The left image shows an anterior view on the prostate contours (5 mm thick slices) and the 7.8 cGy/h surface (smooth surface). The right image shows the realized initial dose rates (2, 4, 6 and 8 cGy/h) through a transverse section of the prostate indicated by the dashed line in the left image.

spacing in the prostate volume as contoured on the post-implant MRI. Figure 8.4 compares the cumulative histograms of the uniform implants and the actual implants. The uniform implants required 43 and 61 seeds respectively, whereas in reality in both patients 36 seeds were implanted. In the uniform implants 99 % target coverage by the 82 Gy and 117 Gy dose levels would be achieved, whereas in the actual implants 99 % target coverage by the 45 Gy and 21 Gy dose levels was realized. These examples show that target coverage may be improved. However, physicians and physicists should be cautious to alter a treatment technique. Change of actual irradiation dose should be based on results regarding local control of the prostate cancer and normal tissue morbidity. Using the MRI-based evaluation method we found that, on average, 99 % target coverage was achieved for the 46 Gy dose level. If we decide to leave the MPD approach and prescribe the minimum peripheral dose, based on a slice-by-slice imaging method, we should lower the prescription dose when aiming for local control and normal tissue morbidity comparable to those of patients implanted in the past. Roy et al. 1993 lowered the 160 Gy prescription dose, which was based on the MPD approach, to 140 Gy (first five patients) and 150 Gy (rest of prostate patients) on the basis of peripheral dose and achieved dose levels for 99 % target coverage between 62 and 100 Gy.

Our analysis showed that target coverage may be improved, if pre-implant prostate volume determination is based on a slice-by-slice imaging study. This approach would generally result in larger prostate volumes and thus larger numbers of I-125 seeds to be implanted compared to the MPD approach. Uniform placement of the seeds within the prostate volume remains a challenging task. More accurate seed placement may be achieved using rigid columns of seeds and spacers (Van 't Riet et al. 1992).

8.4 Conclusions

Using MRI, the prostate and the seeds were well depicted on T_1 -weighted spin echo images, acquired with a relatively weak read-out gradient. Registration of the seed distribution, reconstructed from the isocentric radiographs, and the seed induced signal voids on the MR images enabled reconstruction of the seed and dose distribution in relation to the prostate

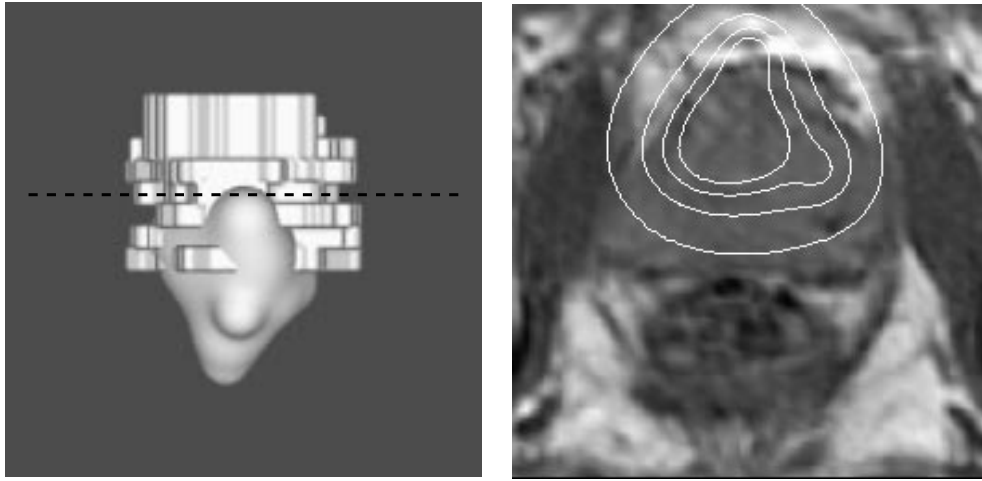


Figure 8.3: Prostate implant with a target coverage of 32 %. The left image shows an anterior view on the prostate contours (5 mm thick slices) and the 7.8 cGy/h surface (smooth surface). The right image shows the realized initial dose rates (2, 4, 6 and 8 cGy/h) through a transverse section of the prostate indicated by the dashed line in the left image.

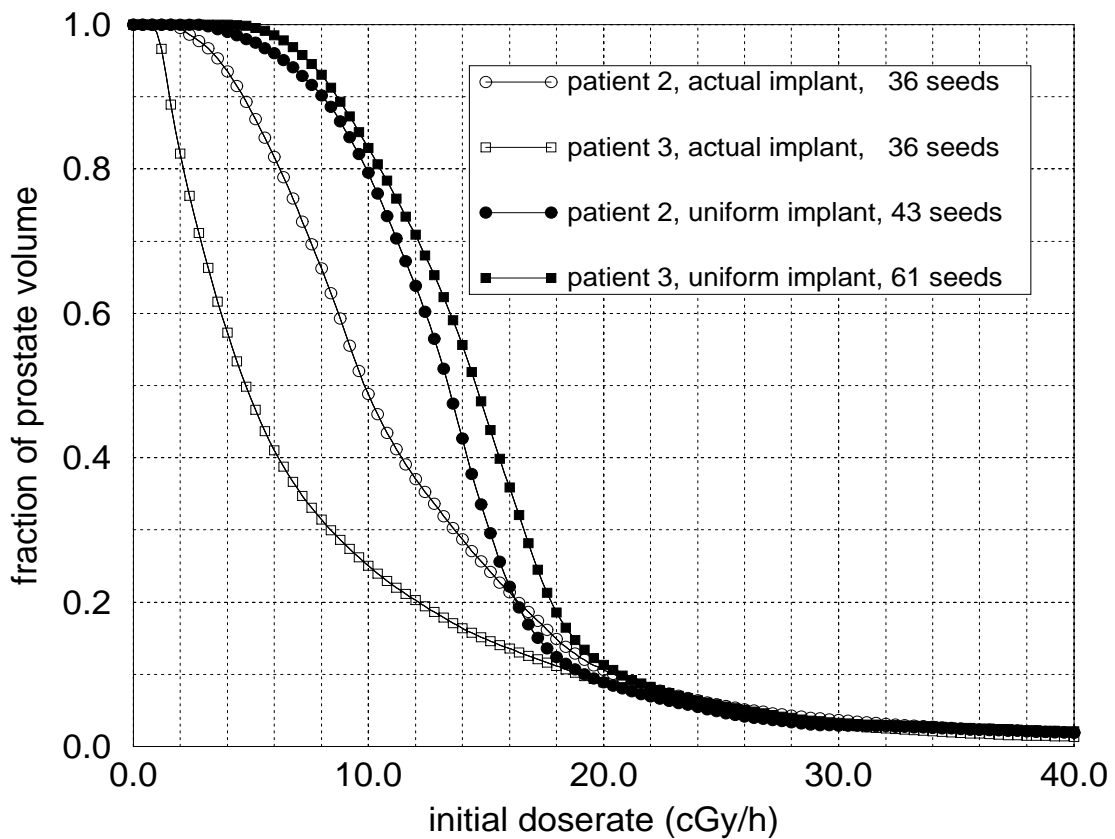


Figure 8.4: Cumulative histograms of actual implants and implants with uniform seed distributions in two patients showing the fractions of the prostate volumes as a function of initial doserate level.

and thus evaluation of target coverage. The fractions of the prostate volumes receiving the prescribed MPD of 160 Gy, ranged from 32 to 71% (mean \pm standard deviation: 60 \pm 10%). The discrepancy between the prescribed dose and realized dose was caused by underestimation of the pre-implant prostate volume due to the ellipsoidal approximation, post-implant prostate swelling at the time of evaluation and inaccuracies in seed placement.

Summary and Conclusion

From its inception in the early 1970's up to the present, magnetic resonance imaging (MRI) has evolved into a sophisticated technique, which has aroused considerable interest in various subfields of medicine including radiotherapy. MRI is capable of imaging in any plane and does not use ionizing radiation by virtue of which MRI lends itself admirably to the purpose of prolonged time course studies. MRI is capable of excellent spatial resolution and it presents information over large areas of the body. The MRI signal depends on multiple parameters resulting in excellent contrast resolution of the soft tissues. Within the realm of radiotherapy, MRI offers prospects with regards to identification of tissues and tissue abnormalities (tumour, oedema, necrosis, fibrosis, cysts), determination of tumour extent in relation to surrounding tissues and organs and assessment of response to treatment. The goal of radiotherapy is to administer a high dose to the tumour while sparing healthy surrounding tissues as much as possible. Since tight margins around the target are applied, accurate information on tumour extent is of great value in radiotherapy treatment planning (RTP). Also information on motion of the tumour and surrounding organs, e.g. caused by respiration, is of importance for defining the margins and can be acquired by fast MR imaging techniques. However, the introduction of MRI into RTP is seriously hampered by geometry and intensity distortions which are known to be present in MRI. These distortions are caused by non-idealities of the equipment (non-uniformity of the static magnetic field and non-linearities of the gradient magnetic fields of the MRI scanner) and by magnetic field perturbations induced by the object to be imaged, in this case the patient. These magnetic field inhomogeneities and gradient field non-linearities lead to image distortions, the severity of which depends on the type of pulse sequence and its parameters. The aim of this thesis is to investigate the capabilities of MRI in radiotherapy treatment planning and to explore the MR image distortions and how distortions can be reduced or, if necessary, corrected in order to integrate MRI into RTP in a reliable manner. Image distortions and the efficacy of correction methods were evaluated in phantom, volunteer, and patient studies. Furthermore, the potential of MRI in organ motion studies was investigated and it was explored whether the image artifacts induced by I-125 seeds could be used to evaluate permanent prostate implants in brachytherapy.

Chapter 1 introduces the potentials and problems with regard to the use of MRI for radiotherapy treatment planning and gives a review of the literature concerning MR image distortions, integration of MRI into RTP, MRI organ motion studies for RTP, and MRI-based brachytherapy evaluation.

Chapter 2 briefly reviews the basic principles of nuclear magnetic resonance (NMR), spatial encoding in MRI, and the sources of geometry and intensity distortions in MRI, viz. machine-related magnetic field inhomogeneity and gradient non-linearity and patient-related magnetic field inhomogeneity due to chemical shift and susceptibility.

Chapter 3 describes the measurement, analysis, and correction of machine dependent geometric distortions in MRI with special attention for phantom design and field error stability in time and for different pulse sequence parameters. Inhomogeneity of the static field and non-linearity of the gradients was established by phantom experiments. A grid phantom of equally spaced tubes appeared to be very suitable for this purpose. Interchanging the directions of the read-out and the phase-encoding gradients enabled decomposition of the image distortions into contributions from static field inhomogeneity and the non-linearity of the three gradients. A 3D map of static field inhomogeneity and non-linearity of the gra-

dients was thus obtained from sagittal, coronal, and transversal multiple slice images with for each acquisition the phantom positioned such that the tubes were perpendicular to the image plane. Time series of measurements on the Gyroscan S15 showed field error stability within the experimental errors of ± 1 ppm for static field inhomogeneity and ± 1 mm for the gradient fields. Measurements on the Gyroscan ACS-NT, equipped with active shielding technology, showed field error stability under different imaging conditions. These observations imply that the measured error maps can be used for correction of patient images which may have been acquired with a pulse sequence that is not necessarily identical to the pulse sequence applied for phantom imaging. The correction procedure reduced distortions up to 13 mm within a volume of interest (VOI) with dimensions $336 \times 336 \times 210 \text{ mm}^3$ to smaller than 2 mm. In a study on the Leksell frame, distortions up to 6.4 mm were reduced to smaller than 1.5 mm. We conclude that MR image corrections are necessary in applications which require mm accuracy and that correction methods, based on 3D maps of static field inhomogeneity and gradient non-linearity, are feasible in clinical practice.

Chapter 4 describes the analysis of the patient related magnetic field perturbations and resulting image distortions in case of MRI of the head and the pelvic region. The magnetic field was calculated by numerically solving the Maxwell equations for a magnetostatic field. The magnetic field around the head resembled a dipole field in the midsagittal plane of calculation with minimal field perturbation on the diagonals. The magnetic field in the localization frame depended strongly on the orientation of the Perspex plates with respect to the applied magnetic field. The maximum spatial distortion of external landmarks in the localization frame amounted 12.8 mm in a 1.5 T MR head image acquired with a relatively weak read-out gradient of 0.68 mT/m. Susceptibility-induced distortions in the pelvic region were smaller than 3 mm in 1.5 T images acquired with a read-out gradient strength of 0.54 mT/m. Since susceptibility induced distortions are proportional to the static magnetic field strength and inversely proportional to the gradient strength, we may conclude that object-related distortions can be reduced to the order of the pixel size by imaging at 0.5 T and using gradient strengths on the order of 3 mT/m.

Chapter 5 describes qualitatively the influence of the type of pulse sequence and its parameters on geometry and intensity distortions. The strength of the read-out gradient, which is controlled by the water fat shift parameter, was the main factor affecting the severity of the susceptibility artifact. The range of water fat shifts, that could be selected, was influenced by the field of view and the acquisition matrix. In echo planar imaging (EPI), the EPI factor (number of profiles acquired after a single excitation) strongly influenced the water fat shift (in pixels) in the phase encoding direction. In applications of MRI, which require geometric accuracy, we should be aware that these parameters indirectly affect the severity of image distortions. Spatial distortions occurred in the direction of the read-out gradient in spin echo (SE) and fast field echo (FFE) imaging, but also and more strongly in the direction of the phase-encoding gradient in echo planar imaging. The direction of the read-out gradient was controlled by the fold-over direction parameter which is the direction of the phase-encoding gradient. Signal loss was most severe in FFE images acquired with relatively long echo times and/or in case of partial k -space sampling (reduced scan matrix, half matrix or partial echo). Generally, highest accuracy and least signal loss is achieved in spin echo imaging with minimal water fat shift and in fast field echo imaging with minimal water fat shift and short echo time.

Chapter 6 describes the investigation of geometric distortions in 1.5 T MR images for use in radiotherapy treatment planning of patients with brain tumours. Patients underwent magnetic resonance imaging in the radiotherapy position with the head fixed by a plastic cast in a Perspex localization frame. For purposes of accuracy assessment, external and internal landmarks were indicated. Tubes attached to the cast and in the localization frame served as external landmarks. In the mid-sagittal plane the brain-sinus sphenoidalis interface, the pituitary gland-sinus sphenoidalis interface, the sphenoid bone and the corpora of the cervical vertebra served as internal landmarks. Landmark displacements as observed in the reversed read-out gradient experiments were analyzed with respect to the contributions of machine related static magnetic field inhomogeneity and susceptibility and chemical shift artifacts. In this study at 1.5 T with read-out gradient strength of 3 mT/m, machine related and susceptibility induced static magnetic field inhomogeneity were on the same order, resulting in spatial distortions between -2 and 2 mm. Internal structures containing yellow bone marrow (the sphenoid bone) shifted 1.6 mm and structures containing red bone marrow shifted 0.8 mm in the direction opposite to the read-out gradient. Both the patient and the localization frame proved to perturb the magnetic field. The field perturbations were shown to be additive. In total, static magnetic field inhomogeneity led to spatial distortions ranging from -2 to 4 mm in the direction of the read-out gradient. Non-linearity of the gradients resulted in spatial distortions ranging from -3.5 to 0.5 mm. After correction for the machine imperfections and susceptibility artifacts, the geometric accuracy of the landmarks in the localization frame was better than 1.3 mm. From this study, we may conclude that accurate treatment setup can be achieved by using a localization frame as a reference coordinate system, provided that the MR images are corrected for image distortions.

Chapter 7 illustrates the use of fast MRI scan techniques for organ motion studies. A magnetic resonance imaging study was performed to determine the respiration induced motion of the kidneys. Under normal respiration conditions displacements of the left and right kidney varied from 2 to 24 mm and 4 to 35 mm, respectively. Under forced respiration conditions displacements were larger and ranged from 10 to 66 mm for the left kidney and 10 to 86 mm for the right kidney. The influence of kidney motion on the radiation dose was determined for patients irradiated on the total abdomen for ovarian cancer with shielding of the kidneys during part of the treatment. The kidney motion resulted in a larger fraction of the kidney volume receiving a dose between 20 and 22 Gy. Individual organ motion studies are a means to individualize margins, so that the individual patient can be treated to a higher dose because of more tight margins. An even more sophisticated approach would be motion gated radiotherapy, e.g. respiration gated radiotherapy, if an organ at risk or the target moves with respiration.

Chapter 8 describes a technique for the evaluation of permanent I-125 prostate implants using radiography and magnetic resonance imaging. Twenty-one patients underwent radiography on the simulator and MRI within 3 days after implantation of the I-125 seeds. Isocentric radiographs were used for reconstruction of the seed distribution, after which registration with the seed induced signal voids on MRI provided the seed positions in relation to the prostate. The prostate was contoured on the transversal magnetic resonance images and dose volume histograms were computed to evaluate the implants. The validity of the ellipsoidal prostate volume approximation, as applied in pre-implant dose calculation, was assessed by comparison of ellipsoidal volumes given by prostate width, height and length and prostate volumes obtained by a slice by slice contouring method, both on post-implant MRI. Prostate

volume changes due to post-implant prostate swelling, were assessed from radiographs taken at 3 days and 1 month after the implantation.

The seeds were readily identified on T_1 -weighted spin echo images and matched with the seed distribution reconstructed from the isocentric radiographs. The matching error, averaged over twenty-one patients, amounted 1.8 ± 0.4 mm (mean \pm standard deviation). The fractions of the prostate volumes receiving the prescribed matched peripheral dose (MPD) ranged from 32 to 71% (mean \pm standard deviation: $60 \pm 10\%$). Prostate volumes, obtained by the contouring method on post-implant MRI, were a factor 1.5 ± 0.3 larger than the ellipsoidal volumes given by the prostate dimensions on post-implant MRI. Prostate volumes 3 days after the implantation were a factor 1.3 ± 0.2 larger than the prostate volumes 1 month after the implantation. Registration of the reconstructed seed distribution and the MR images showed inaccuracies in seed placement, e.g. two or more seeds clustering together or seeds outside the prostate. Registration of the reconstructed seed distribution and the MR images enabled evaluation of target coverage, which amounted $60 \pm 10\%$. The discrepancy between prescribed dose and realized dose was caused by underestimation of the pre-implant prostate volume due to the ellipsoidal approximation, post-implant prostate swelling at the time of evaluation and inaccuracies in seed placement.

The MRI-based evaluation method provides better insight in the irradiation dose to the prostate compared to the MPD approach. The present method can be used to assess the correlation of local control of the prostatic cancer and target coverage and to evaluate different implant techniques and modifications of the techniques. Since the adequacy of the treatment depends on a sufficient number of seeds with a certain activity implanted, accurate volume determination is essential. Uncertainty in target volume determination was demonstrated by the discrepancy in prostate volumes determined by TRUS (ellipsoidal approximation) and by MRI (slice by slice contouring method). MRI seems to be valuable in prostate volume determination and it should be considered to base pre-implant dosimetry on magnetic resonance imaging of the prostate. It might even be considered to replace ultrasound by magnetic resonance imaging as the guiding imaging modality in the transperineal implantation technique. The availability of endorectal receiver coils for MRI and open MRI scanners, designed for interventional MRI, in principle allow a transrectal MRI guided transperineal implantation technique similar to the transrectal ultrasound guided technique.

In this thesis, it was shown that geometric distortions in MRI can not be ignored if mm accuracy is required. Whereas object-related distortions can be reduced by scanning at low field strength (0.5 T) and using moderate to large gradient strength (≈ 3 mT/m), image distortions due to gradient non-linearity should be checked on each MRI scanner and if necessary corrected to meet the geometric accuracy requirements for radiotherapy treatment planning.

In a study on patients with brain tumours, it was shown that accurate MRI-based radiotherapy treatment planning is achievable.

In a study on volunteers, the use of fast MRI scan techniques for organ motion studies was illustrated and in a study on patients with prostate cancer, the value of MRI for the evaluation of brachytherapy was demonstrated for permanent implants with I-125 seeds.

Samenvatting en conclusie

In de jaren '70 werd het principe van nuclear magnetic resonance (NMR) voor het eerst toegepast om het menselijk lichaam af te beelden. Sindsdien heeft magnetic resonance imaging (MRI) zich ontwikkeld tot een afbeeldingstechniek met vele toepassingen binnen verschillende gebieden van de geneeskunde, inclusief de radiotherapie. MRI maakt het mogelijk afbeeldingen te maken van willekeurig georiënteerde plakken in het lichaam en daarvoor is geen ioniserende straling nodig, waardoor MRI bijzonder geschikt is voor studies, waarbij patiënt of proefpersoon gedurende langere tijd vervolgd wordt. De ruimtelijke resolutie van MRI is goed en het hele lichaam kan afgebeeld worden. Het MR signaal hangt van verschillende parameters af, hetgeen resulteert in een goed contrast tussen de verschillende weke delen in het lichaam.

Binnen de radiotherapie is MRI toe te passen voor de identificatie van weefsels en afwijkingen (tumor, oedeem, necrose, fibrose, cystes), de bepaling van tumoruitbreiding in relatie tot de omringende weefsels en organen en de bepaling van het effect van de behandeling. Het doel van radiotherapie is om een hoge dosis straling toe te dienen aan de tumor, terwijl de omringende weefsels zo veel mogelijk gespaard blijven. Aangezien de marges rond het doelgebied zo klein mogelijk gekozen worden, is het voor de radiotherapie treatment planning (RTP) van groot belang om nauwkeurig geïnformeerd te zijn omtrent de uitbreiding van de tumor. Ook informatie met betrekking tot beweging van de tumor en omringende organen, ten gevolge van bijvoorbeeld ademhaling, is van belang voor de bepaling van de marges en kan verkregen worden met snelle MR afbeeldingstechnieken. Echter, de introductie van MRI in de radiotherapie wordt gehinderd door de geometrie- en intensiteitsverstoringen in MRI. Deze verstoringen worden veroorzaakt door de apparatuur (inhomogeniteit van het magneetveld en niet-lineariteit van de gradiëntmagneetvelden) en door de verstoring van het magneetveld door het object zelf, in dit geval de patiënt. Deze inhomogeniteiten en de niet-lineariteiten leiden tot beeldverstoringen, waarvan de ernst afhangt van het type pulssequentie en de parameters daarvan.

In dit proefschrift werd onderzoek verricht naar de mogelijkheden en beperkingen van MRI voor de radiotherapieplanning. Hierbij lag het accent op de MR beeldverstoringen en hoe deze gereduceerd of, indien nodig, gecorrigeerd kunnen worden, zodat MRI op een betrouwbare wijze in de radiotherapieplanning geïntegreerd kan worden. Beeldvervormingen en de doeltreffendheid van correctiemethoden werden geëvalueerd door middel van onderzoek aan fantomen, proefpersonen en patiënten. Verder werden de mogelijkheden van MRI met betrekking tot het onderzoek van beweging van organen onderzocht en werd onderzocht of de beeldartefacten, welke veroorzaakt worden door I-125 zaadjes, van nut kunnen zijn in de brachytherapie voor de evaluatie van permanente prostaatimplantaties.

Hoofdstuk 1 introduceert de mogelijkheden en problemen met betrekking tot het gebruik van MRI bij de radiotherapie treatment planning (RTP) en geeft een overzicht van de literatuur over MR beeldverstoringen, integratie van MRI in RTP, onderzoek naar orgaanbeweging met behulp van MRI en evaluatie van brachytherapie met behulp van MRI.

Hoofdstuk 2 geeft een korte inleiding tot de basisprincipes van nuclear magnetic resonance (NMR), ruimtelijke codering in MRI, en de oorzaken van geometrie- en intensiteitsverstoringen in MRI, namelijk de machine-afhankelijke inhomogeniteit van het magneetveld en niet-lineariteit van de gradiënten en de patiënt-afhankelijke inhomogeniteit van het magneetveld ten gevolge van chemical shift en susceptibiliteitseffecten.

Hoofdstuk 3 beschrijft de meting, analyse en correctie van machine-afhankelijke geometrische

verstoringen in MRI. Een speciaal ontworpen fantoom met buisjes, welke evenwijdig aan elkaar waren geplaatst in een regelmatig raster, werd toegepast om de inhomogeniteit van het magneetveld en de niet-lineariteit van de gradiënten te onderzoeken. Daarbij werd ook aandacht besteed aan de stabiliteit van de magneetveldfouten in de tijd en bij verschillende pulssequenties en parameters. Door de richtingen van de frequentiecoderings- en de fasecoderingsgradiënten te verwisselen, was het mogelijk om de oorzaken van de beeldvervalsingen te ontleden in bijdragen van veldinhomogeniteit en niet-lineariteit van de drie gradiënten. Een driedimensionale “map” van magneetveldinhomogeniteit en niet-lineariteit van de gradiënten werd verkregen uit sagittale, coronale en transversale multiple slice beelden, waarbij het fantoom bij iedere acquisitie zodanig werd geplaatst dat de buisjes loodrecht op het vlak van afbeelding stonden. Metingen gedurende anderhalf jaar op de Gyroscan S15 toonden aan dat de afwijkingen reproduceerbaar waren binnen de meetfout van ± 1 mm. Metingen op de Gyroscan ACS-NT, welke uitgerust is met extra gradiëntspoelen om wervelstromen te onderdrukken, toonden aan dat de veldfouten reproduceerbaar waren bij verschillende pulssequenties en de parameters daarvan. Uit deze waarnemingen konden we concluderen dat de “map” van de fouten van het statische magneetveld en de gradiëntmagneetvelden gebruikt kan worden voor correctie van MR beelden van patiënten, die niet noodzakelijkerwijs verkregen zijn met een pulssequentie die gelijk is aan de pulssequentie, waarmee de fantoombeelden verkregen zijn. De correctieprocedure reduceerde de beeldvervalsingen, die binnen een volume of interest (VOI) met afmetingen $336 \times 336 \times 210$ mm³ tot 13 mm groot waren, tot kleiner dan 2 mm. In een studie met een lokalisatieframe werden vervormingen van 6,4 mm gereduceerd tot kleiner dan 1,5 mm. We concluderen dat MR beeldcorrecties nodig zijn voor applicaties, waarbij een nauwkeurigheid in de orde van een mm is vereist en dat correctiemethodes, welke gebruik maken van een 3D “map” van de inhomogeniteit van het statische veld en de niet-lineariteit van de gradiënten, klinisch toepasbaar zijn.

Hoofdstuk 4 beschrijft de analyse van de perturbaties van het magneetveld door de patiënt en eventuele hulpstukken en de daarmee samenhangende vervormingen in beelden van het hoofd en het bekken. Het magneetveld werd berekend door de Maxwell vergelijkingen op te lossen met behulp van een numerieke methode. Uit berekeningen in het midsagittale vlak door hoofd en lokalisatieframe bleek dat het veld rondom het hoofd vergelijkbaar is met het veld van een dipool. De perturbaties langs de diagonalen waren minimaal. Het magneetveld in het lokalisatieframe was sterk afhankelijk van de richting van de platen ten opzichte van het aangelegde statische magneetveld. De grootste verplaatsing van de markeringsen in het frame bedroeg 12,8 mm in een 1,5 T MR beeld van het hoofd, welke was verkregen met een relatief zwakke frequentiecoderingsgradiënt van 0,68 mT/m. Beeldvervalsingen door susceptibiliteit waren in het bekkengebied kleiner dan 3 mm in 1,5 T beelden, welke verkregen waren met een frequentiecoderingsgradiënt van 0,54 mT/m. Aangezien vervormingen door susceptibiliteit evenredig zijn met de sterkte van het statische magneetveld en omgekeerd evenredig met de gradiëntsterkte, kunnen we concluderen dat de patiënt-afhankelijke vervormingen gereduceerd kunnen worden tot de orde van grootte van de pixel door een magneetveld van 0,5 T en gradiënten van 3 mT/m of sterker toe te passen.

Hoofdstuk 5 geeft een kwalitatieve beschouwing over de invloed van de pulssequentie en de parameters op de geometrie- en intensiteitsverstoringen. De amplitude van de frequentiecoderingsgradiënt, welke ingesteld werd met de water fat shift parameter, was van grote invloed op de ernst van de beeldvervalsingen door susceptibiliteit. Het bereik van de water

fat shift (in pixels) was afhankelijk van het field of view (FOV) en de acquisitiematrix. In echo planar imaging (EPI) werd de water fat shift in de fasecoderingsrichting sterk beïnvloed door de EPI factor (aantal gemeten profielen na één excitatie). In toepassingen van MRI, waarbij geometrische nauwkeurigheid vereist is, moet men bedenken dat deze parameters indirect van invloed zijn op de ernst van de beeldvervalsingen. Geometrische verstoringen treden op in de richting van de frequentiecoderingsgradiënt in spin echo (SE) en fast field echo (FFE) afbeeldingen, maar ook en zelfs sterker in de richting van de fasecoderingsgradiënt in echo planar imaging. De richting van de frequentiecoderingsgradiënt is loodrecht op de richting van de fasecoderingsgradiënt, welke werd ingesteld met de fold-over direction parameter. Signaalverlies was het sterkst in FFE beelden, die verkregen waren met relatief lange echotijden en/of in geval van onvolledige bemonstering van de k -ruimte (reduced scan matrix, half matrix of partial echo). In het algemeen wordt de grootste geometrische nauwkeurigheid en minste intensiteitsverstoring bereikt in spin echo afbeeldingen met minimale water fat shift en in fast field echo afbeeldingen met minimale water fat shift en korte echotijd.

Hoofdstuk 6 beschrijft het onderzoek naar geometrische verstoringen in 1,5 T MR beelden te gebruiken voor radiotherapie treatment planning van patiënten met hersentumoren. De patiënten ondergingen MRI in de positie, waarin ze ook radiotherapie ontvingen, dat wil zeggen met het hoofd gefixeerd in een cast in een lokalisatieframe. De geometrische nauwkeurigheid van de beelden werd vastgesteld aan de hand van uitwendige en inwendige markeringspunten. Slangtjes op de cast en in het lokalisatieframe dienden als uitwendige markeringen. De overgangen tussen hersenweefsel en de sinus sphenoidalis en tussen de hypofysis en de sinus sphenoidalis, het os sphenoidale en de cervicale wervellichamen dienden als inwendige markeringspunten. De verplaatsingen van de markeringen in de beelden met positieve en negatieve frequentiecoderingsgradiënt werden geanalyseerd met betrekking tot de bijdragen van machine-afhankelijke magneetveldinhomogeniteit en chemical shift en susceptibiliteitsartefacten. In deze studie bij 1,5 T met een frequentiecoderingsgradiënt van 3 mT/m waren de machine-afhankelijke en de door susceptibiliteit veroorzaakte magneetveldinhomogeniteit van de zelfde orde van grootte. Beide gaven ze aanleiding tot geometrische verstoringen tussen -2 en 2 mm. Inwendige structuren met geel beenmerg (het os sphenoidale) gaven een verplaatsing te zien van $1,6$ mm en structuren met rood beenmerg een verplaatsing van $0,8$ mm in de richting tegenovergesteld aan de richting van de frequentiecoderingsgradiënt. De patiënt én het lokalisatieframe gaven aanleiding tot magneetveldverstoringen, welke additief bleken te zijn. De magneetveldverstoringen leidden samen tot beeldvervalsingen tussen -2 en 4 mm in de richting van de frequentiecoderingsgradiënt. Niet-lineariteit van de gradiënten resulteerde in beeldvervalsingen tussen $-3,5$ en $0,5$ mm. Na correctie voor de machine-afhankelijke vervormingen en de susceptibiliteitsartefacten was de geometrische nauwkeurigheid van de uitwendige markeringen in het lokalisatieframe beter dan $1,3$ mm. Uit deze studie kunnen we concluderen dat nauwkeurige positionering van bestralingsbundels met behulp van een lokalisatieframe en MRI mogelijk is, mits de MR beeldvervalsingen gecorrigeerd worden.

Hoofdstuk 7 illustreert het gebruik van snelle MRI technieken voor de bestudering van orgaanbeweging. Er werd een studie uitgevoerd om de beweging van de nieren ten gevolge van de ademhaling te bepalen. Bij een rustige ademhaling varieerden de verplaatsingen van de linker en de rechter nier tussen respectievelijk 2 en 24 mm en 4 en 35 mm. Bij diepe ademhaling waren de verplaatsingen groter, namelijk tussen 10 en 66 mm voor de linker nier en tussen 10 en 86 mm voor de rechter nier. De gevolgen van de beweging van de nieren

voor de stralingsdosis werden gesimuleerd voor patiënten die op het gehele abdomen bestraald worden in verband met ovariumkanker, waarbij gedurende een gedeelte van de serie bestralingen de nieren worden afgeschermd. De beweging van de nieren had tot gevolg dat een groter gedeelte van de nieren een dosis tussen 20 en 22 Gy ontving. Op grond van studies van de orgaanbewegingen in individuele patiënten kunnen de marges per patiënt zo krap mogelijk gekozen worden, zodat een grotere stralingsdosis toegediend kan worden. Een nog meer verfijnde aanpak zou kunnen bestaan uit “motion gated” radiotherapie, dat wil zeggen dat pulsen straling worden gegeven tijdens perioden van betrekkelijke rust in de cyclus van de ademhaling.

Hoofdstuk 8 beschrijft een techniek voor de evaluatie van permanente prostaatimplantaties met I-125 zaadjes, waarbij gebruik wordt gemaakt van röntgenfoto's en MRI. Van 21 patiënten werden binnen 3 dagen na de implantatie röntgenfoto's en MRI scans gemaakt. Isocentrische röntgenfoto's werden gebruikt voor de reconstructie van de verdeling van de zaadjes, waarna matching met de zaadjes op MRI, zichtbaar als gebiedjes met signaalverlies, de verdeling van de zaadjes ten opzichte van de prostaat gaf. De prostaat werd ingetekend op de transversale MR beelden en dosis-volume histogrammen werden berekend voor de evaluatie van de implantaten. De geldigheid van de ellipsoïdale benadering van het prostaatvolume, die wordt toegepast bij de dosisberekening voorafgaand aan de implantatie, werd onderzocht door ellipsoïdale volumes te vergelijken met prostaatvolumes verkregen via de intekenmethode, beide op grond van MRI na de implantatie. Veranderingen in prostaatvolume ten gevolge van zwelling van de prostaat na de implantatie werden onderzocht aan de hand van röntgenfoto's, die 3 dagen en 1 maand na de implantatie gemaakt werden.

De I-125 zaadjes waren goed te detecteren op T_1 -gewogen spin echo afbeeldingen en konden gematched worden met de zaadjesverdeling die gereconstrueerd werd uit de isocentrische röntgenfoto's. De fout in het matchen, gemiddeld over 21 patiënten, bedroeg $1,8 \pm 0,4$ mm (gemiddelde \pm standaardafwijking). De fractie van de prostaat, welke de voorgeschreven matched peripheral dose (MPD) ontving, varieerde van 32 tot 71% (gemiddelde \pm standaardafwijking: $60 \pm 10\%$). Prostaatvolumes, bepaald met de intekenmethode op MRI na de implantatie, waren een factor $1,5 \pm 0,3$ groter dan de ellipsoïdale volumes op MRI na de implantatie. Prostaatvolumes waren 3 dagen na de implantatie een factor $1,3 \pm 0,2$ groter dan de prostaatvolumes 1 maand na de implantatie. Matching van de gereconstrueerde zaadjes en de MR beelden lieten onnauwkeurigheden in de plaatsing van de zaadjes zien, bijvoorbeeld twee of meer zaadjes dicht bij elkaar of zaadjes buiten de prostaat. Matching van de gereconstrueerde zaadjesverdeling en de MR beelden maakte evaluatie van de dosisverdeling in de prostaat mogelijk, waarbij bleek dat de dekking van de prostaat door de voorgeschreven dosis $60 \pm 10\%$ bedroeg. De discrepantie tussen de voorgeschreven dosis en de toegediende dosis werd veroorzaakt door onderschatting van het prostaatvolume ten gevolge van de ellipsoïdale benadering, zwelling van de prostaat na de implantatie en onnauwkeurigheden in plaatsing van de zaadjes.

De evaluatie met behulp van MRI geeft een beter inzicht in de stralingsdosis in de prostaat ten opzichte van de methode waarbij de MPD berekend wordt. De huidige methode kan gebruikt worden om de correlatie te onderzoeken tussen lokale controle van prostaatkanker en de stralingsdosis in de prostaat en om verschillende implantatietechnieken en modificaties te evalueren. Aangezien de toereikendheid van de behandeling afhangt van de implantatie van een voldoende aantal zaadjes met een bepaalde activiteit, is nauwkeurige bepaling van het prostaatvolume van groot belang. Onnauwkeurigheid in de bepaling van het prostaatvolume werd aangetoond door de discrepantie tussen de volumes, die bepaald werden met behulp

van transrectale ultrasound (ellipsoïdale benadering) en de volumes, die bepaald werden met MRI (intekenmethode). MRI lijkt waardevol te zijn voor de bepaling van het prostaatvolume en het zou overwogen moeten worden om de dosisberekening voorafgaand aan de implantatie te baseren op MRI van de prostaat. Het is zelfs niet uitgesloten om ultrasound te vervangen door MRI als de afbeeldingstechniek op geleide waarvan de transperineale implantatie wordt uitgevoerd. De beschikbaarheid van endorectale ontvangstspoelen voor MRI en open MRI scanners, ontworpen voor interventie-MRI, maken in principe een transrectale MRI geleide transperineale implantatietechniek mogelijk, die te vergelijken is met de transrectale ultrasound geleide transperineale implantatietechniek.

In dit proefschrift werd aangetoond dat geometrische verstoringen in MRI niet genegeerd kunnen worden, indien nauwkeurigheid in de orde van enkele millimeters vereist is. Objectafhankelijke vervormingen kunnen gereduceerd worden door bij lage veldsterkte (0,5 T) en relatief grote gradiëntsterkte (≈ 3 mT/m) te scannen, maar beeldvervormingen ten gevolge van niet-lineaire gradiënten moeten voor iedere scanner gemeten en indien nodig gecorrigeerd worden om te voldoen aan de vereiste nauwkeurigheid in radiotherapie treatment planning.

In een onderzoek aan patiënten met hersentumoren werd aangetoond dat nauwkeurige radiotherapieplanning op grond van MRI mogelijk is.

In een onderzoek met proefpersonen werd het gebruik van snelle MR afbeeldingstechnieken geïllustreerd en in een onderzoek aan patiënten met prostaatkanker werd de waarde van MRI voor de evaluatie van brachytherapie, in dit geval permanente implantaties met I-125 zaadjes, gedemonstreerd.

References

- Abragam, A. (1961). *The principles of nuclear magnetism*. London, Oxford University Press.
- Anderson, L.L. (1976). Spacing nomograph for interstitial implants of I-125 seeds. *Medical Physics* 3, 48–51.
- Arun, K.S., Huang, T.S., and Blostein, S.D. (1987). Least-squares fitting of two 3-D point sets. *IEEE Transactions on Pattern Analysis and Machine Intelligence PAMI-9*, 698–700.
- Aydin, H., Bachmann, G., Lieven, H. von, and Sens, M. (1993). MRI-guided brachytherapy for cancer of the oesophagus. *European Radiology* 3, 219–222.
- Bakker, C.J.G., Bhagwandien, R., and Moerland, M.A. (1994). Simulation of susceptibility artifacts in 2D and 3D Fourier Transform spin-echo and gradient-echo magnetic resonance imaging. *Magnetic Resonance Imaging* 12, 767–774.
- Bakker, C.J.G., Bhagwandien, R., Moerland, M.A., and Fuderer, M. (1993). Susceptibility artifacts in 2DFT spin-echo and gradient-echo imaging: The cylinder model revisited. *Magnetic Resonance Imaging* 11, 539–548.
- Bakker, C.J.G., Moerland, M.A., Bhagwandien, R., and Beersma, R. (1992). Analysis of machine-dependent and object-induced geometric distortions in 2DFT MR imaging. *Magnetic Resonance Imaging* 10, 597–608.
- Bhagwandien, R. (1994). *Object induced geometry and intensity distortions in magnetic resonance imaging*. Ph. D. thesis, University of Utrecht, The Netherlands.
- Bhagwandien, R., Moerland, M.A., Bakker, C.J.G., Beersma, R., and Lagendijk, J.J.W. (1992b). Analysis of patient induced marker shifts in MRI. In *Proceedings Eleventh Annual Meeting of the Society for Magnetic Resonance in Medicine (SMRM)*, pp. 4305.
- Bhagwandien, R., Moerland, M.A., Bakker, C.J.G., Beersma, R., and Lagendijk, J.J.W. (1994). Numerical analysis of the magnetic field for arbitrary magnetic susceptibility distributions in 3D. *Magnetic Resonance Imaging* 12, 101–107.
- Bhagwandien, R., Van Ee, R., Beersma, R., Bakker, C.J.G., Moerland, M.A., and Lagendijk, J.J.W. (1992a). Numerical analysis of the magnetic field for arbitrary magnetic susceptibility distributions in 2D. *Magnetic Resonance Imaging* 10, 299–313.
- Blasko, J.C., Radge, H., and Schumacher, D. (1987). Transperineal percutaneous iodine-125 implantation for prostatic carcinoma using transrectal ultrasound and template guidance. *Endocurietherapy Hyperthermia Oncology* 3, 131–139.
- Bloom, W. and Fawcett, D.W. (1968). *A textbook of histology*. Saunders, Philadelphia.

- Boesecke, R., Becker, G., Alandt, K., Pastyr, O., Doll, J., Schlegel, W., and Lorenz, W.J. (1991). Modification of a three-dimensional treatment planning system for the use of multi-leaf collimators in conformation radiotherapy. *Radiotherapy and Oncology* 21, 261–268.
- Boesecke, R., Bruckner, T., and Ende, G. (1990). Landmark based correlation of medical images. *Physics in Medicine and Biology* 35, 121–126.
- Brahme, A. (1984). Dosimetric precision requirements in radiation therapy. *Acta Radiologica Oncology* 23, 379–391.
- Brahme, A. (1988). Optimization of stationary and moving beam radiation therapy techniques. *Radiotherapy and Oncology* 12, 129–140.
- Chang, H. and Fitzpatrick, J.M. (1992). A technique for accurate magnetic resonance imaging in the presence of field inhomogeneities. *IEEE Transactions on Medical Imaging* 11, 319–329.
- Cho, Z.H., Kim, D.J., and Kim, Y.K. (1988). Total inhomogeneity correction including chemical shifts and susceptibility by view angle tilting. *Medical Physics* 15, 7–11.
- Cho, Z.H. and Ro, Y.M. (1992). Reduction of susceptibility artifact in gradient-echo imaging. *Magnetic Resonance in Medicine* 23, 193–200.
- Chu, S.C.K., Xu, Y., Balschi, J.A., and Springer Jr., C.S. (1990). Bulk magnetic susceptibility shifts in NMR studies of compartmentalized samples: Use of paramagnetic reagents. *Magnetic Resonance in Medicine* 13, 239–262.
- Collignon, A., Vandermeulen, D., Suetens, P., and Marchal, G. (1994). Registration of 3-D multimodality medical images using surfaces and point landmarks. *Pattern Recognition Letters* 15, 461–467.
- Cox, J.C., Bydder, G.M., Gadian, D.G., Young, I.R., Proctor, E., Williams, S.R., and Hart, I. (1986). The effect of magnetic susceptibility variations in NMR imaging and NMR spectroscopy in vivo. *Journal of Magnetic Resonance* 70, 163–168.
- Cristy, M. (1981). Active bone marrow distribution as a function of age in humans. *Physics in Medicine and Biology* 26, 389–400.
- Dawson, J.E., Wu, T., Roy, T., Gu, J.Y., and Kim, H. (1994). Dose effects of seeds placement deviations from pre-planned positions in ultrasound guided prostate implants. *Radiotherapy and Oncology* 32, 268–270.
- De Bree, J., Van der Koijk, J.F., and Legendijk, J.J.W. (1996). A 3D high resolution SAR model for current source interstitial hyperthermia. *IEEE Transactions on Biomedical Engineering*, (accepted).
- Dickinson, W.C. (1951). The time average magnetic field at the nucleus in nuclear magnetic resonance experiments. *Physical Review* 81, 717–731.
- Dixon, W.T. (1984). Simple proton spectroscopic imaging. *Radiology* 153, 189–194.
- Dutreix, A. (1984). When and how can we improve precision in radiotherapy. *Radiotherapy and Oncology* 2, 275–292.
- Edmonds, D.T. and Wormald, M.R. (1988). Theory of resonance in magnetically inhomogeneous specimens and some useful calculations. *Journal of Magnetic Resonance* 77, 223–232.

- Ehman, R.L., McNamara, M.T., Hricak, H., and Higgins, C.B. (1984). Magnetic resonance imaging with respiratory gating: Techniques and advantages. *American Journal of Roentgenology* 143, 1175–1182.
- Ehricke, H.H. and Schad, L.R. (1992). MRA-guided stereotactic radiation treatment planning for cerebral angiomas. *Computerized Medical Imaging and Graphics* 16, 65–71.
- Elster, A.D. (1994). *Questions and answers in Magnetic Resonance Imaging*. St. Louis, Mosby-Year Book Inc.
- Ende, G., Treuer, H., and Boesecke, R. (1992). Optimization and evaluation of landmark-based image correlation. *Physics in Medicine and Biology* 37, 261–271.
- Ericsson, A., Hemmingsson, A., Jung, B., and Sperber, G.O. (1988). Calculation of MRI artifacts caused by static field disturbances. *Physics in Medicine and Biology* 33, 1103–1112.
- Evans, A., Marret, S., Collins, L., and Peters, T. (1989). Anatomical-functional correlative analysis of the human brain using three dimensional imaging systems. In *Proceedings SPIE Vol 1092 Medical imaging III: Image processing*, pp. 264–274.
- Farrar, T.C. and Becker, E.D. (1971). *Pulse and Fourier Transform NMR*. New York, Academic press.
- Feygelman, V., Noriega, B.K., Sanders, R.M., and Friedland, J.L. (1995). A spreadsheet technique for dosimetry of transperineal prostate implants. *Medical Physics* 22, 97–100.
- Fraass, B.A., McShan, D.L., Diaz, R.F., TenHaken, R.K., Aisen, A., Gebarski, S., Glazer, G., and Lichter, A.S. (1987). Integration of magnetic resonance imaging into radiation therapy treatment planning: I. Technical considerations. *International Journal Radiation Oncology Biology Physics* 13, 1897–1908.
- Galvin, J.M., Sontag, M.R., Axel, L., and Bloch, P. (1984). Radiation therapy treatment planning using magnetic resonance images. *Medical Physics* 11, 376.
- Glatstein, E., Lichter, A.S., Fraass, B.A., Kelly, B.A., and Van de Geijn, J. (1985). The image revolution and radiation oncology: Use of CT, Ultrasound, and NMR for localization, treatment planning and treatment delivery. *International Journal Radiation Oncology Biology Physics* 11, 299–314.
- Goitein, M. (1985). Calculation of the uncertainty in the dose delivered during radiation therapy. *Medical Physics* 12, 608–612.
- Gore, J.C. (1988). *Reviews of Magnetic Resonance in Medicine*, Volume 3 (1), pp. 1–51. Pergamon Press.
- Grimm, P.D., Blasko, J.C., and Ragde, H. (1994). Ultrasound-guided transperineal implantation of iodine-125 and palladium-103 for the treatment of early-stage prostate cancer; technical concepts in planning, operative technique and evaluation. *Atlas of the urologic clinics of North America* 2, 113–125.
- Haacke, E.M., Tkach, J.A., and Parrish, T.B. (1989). Reduction of T2* dephasing in gradient field-echo imaging. *Radiology* 170, 457–462.
- Heesters, M.A.A.M., Wijrdeman, H.K., Struikmans, H., Witkamp, T.D., and Moerland, M.A. (1993). Brain tumour delineation based on CT and MR imaging; implications for radiotherapy treatment planning. *Strahlentherapie und Onkologie* 12, 729–733.

- Hemler, P.F., Van den Elsen, P.A., Sumanaweera, T.S., Napel, S., Drace, J., and Adler, J.R. (1995). A quantitative comparison of residual error for three different multimodality registration techniques. In *Proceedings XIVth International conference on information processing in medical imaging (IPMI)*, pp. 251–262.
- Henkelman, R.M., Poon, P.Y., and Bronskill, M.J. (1984). Is magnetic resonance imaging useful for radiation therapy planning? In *Proceedings Eight International conference on computers in radiation therapy*, pp. 181–185.
- Hill, D.L.G., Hawkes, D.J., Crossman, J.E., Gleeson, M.J., Cox, T.C.S., Bracey, E.E.C.M.L., Strong, A.J., and Graves, P. (1991). Registration of MR and CT images for skull base surgery using point like anatomical features. *British Journal of Radiology* 64, 1030–1035.
- Holm, H.H., Juul, N., Pedersen, J.F., Hansen, H., and Stroyer, I. (1983). Transperineal iodine-125 seed implantation in prostatic cancer guided by transrectal ultrasonography. *Journal of Urology* 130, 283–286.
- Holsinger, A.E., Wright, R.C., Riederer, S.J., Farzaneh, F., Grimm, R.C., and Maier, J.K. (1990). Real-time interactive magnetic resonance imaging. *Magnetic Resonance in Medicine* 14, 547–553.
- Huizenga, H., Levendag, P.C., de Porre, P.M.Z.R., and Visser, A.G. (1988). Accuracy in radiation field alignment in head and neck cancer: A prospective study. *Radiotherapy and Oncology* 11, 181–187.
- Jiang, H., Robb, R., and Holton, K.S. (1992). A new approach to 3-D registration of multimodality medical images by surface matching. In *Proceedings SPIE Vol 1808 Visualization in biomedical computing*, pp. 196–213.
- Just, M., Rösler, H.P., Kutzner, J., and Thelen, M. (1991). MRI-assisted radiation therapy planning of brain tumors- clinical experiences in 17 patients. *Magnetic Resonance Imaging* 9, 173–177.
- Kawanaka, A. and Takagi, M. (1986). Estimation of static magnetic field and gradient fields from NMR image. *Journal of Physics E: Scientific Instrumentation* 19, 871–875.
- Kessler, M.L., Pitluck, S., Petti, P., and Castro, J.R. (1991). Integration of multimodality imaging data for radiotherapy treatment planning. *International Journal Radiation Oncology Biology Physics* 21, 1653–1667.
- Kooy, H.M., Van Herk, M.B., Barnes, P.D., Alexander III, E., Dunbar, S.F., Tarbell, N.J., Mulkern, R.V., Holupka, E.J., and Loeffler, J.S. (1994). Image fusion for stereotactic radiotherapy and radiosurgery treatment planning. *International Journal Radiation Oncology Biology Physics* 28, 1229–1234.
- Korin, H.W., Ehman, R.L., Riederer, S.J., Felmlee, J.P., and Grimm, R.C. (1992). Respiratory kinematics of the upper abdominal organs: a quantitative study. *Magnetic Resonance in Medicine* 23, 172–178.
- Kotte, A.N.T.J., De Bree, J., Lagendijk, J.J.W., Bakker, C.J.G., Van der Koijk, J.F., Crezee, J., Van Leeuwen, G.M.J., Raaijmakers, B.J., Struikmans, H., Hulshof, M.C.C.M., Visser, A.G., and Battermann, J.J. (1996b). A 3D treatment planning system for interstitial hyperthermia. In *Proceedings 7th International Congress on Hyperthermic Oncology*, Volume II, pp. 537–539.

- Kotte, A.N.T.J., Van Leeuwen, G.M.J., De Bree, J., Van der Koijk, J.F., Crezee, J., and Lagendijk, J.J.W. (1996a). A description of discrete vessel segments in thermal modelling of tissues. *Physics in Medicine and Biology* 41, 865–884.
- Kubo, H.D. and Hill, B.C. (1996). Respiration gated radiotherapy treatment: a technical study. *Physics in Medicine and Biology* 41, 83–91.
- Lagendijk, J.J.W., Visser, A.G., Kaatee, R.S.J.P., Crezee, J., Van der Koijk, J.F., De Bree, J., Kotte, A.N.T.J., Kanis, A.P., Kroeze, H., Levendag, P.C., and Battermann, J.J. (1995). Interstitial hyperthermia & treatment planning: the 27 MHz multi-electrode current source method. *Activity International Nucletron-Oldelft Radiotherapy Journal* (Special Report, No.6), 83–90.
- Leksell, L. (1951). The stereotaxic method and radiosurgery of the brain. *Acta Chirurgica Scandinavica* 102, 316–319.
- Lerski, R.L., McRobbie, D.W., Straughan, K., Walker, P.M., de Certaines, J.D., and Bernard, A.M. (1988). Multi-center trial with protocols and prototype test objects for the assessment of mri equipment. *Magnetic Resonance Imaging* 6, 201–214.
- Ling, C.C., Yorke, E.D., Spiro, I.J., Kubiatowicz, D., and Bennett, D. (1983). Physical dosimetry of ^{125}I seeds of a new design for interstitial implant. *International Journal Radiation Oncology Biology Physics* 9, 1747–1752.
- Lüdeke, K.M., Röschmann, P., and Tischler, R. (1985). Susceptibility artifacts in NMR Imaging. *Magnetic Resonance Imaging* 3, 329–343.
- Lulu, B.A., Lutz, W., Stea, B., and Cetas, T.C. (1990). Treatment planning of template-guided stereotaxic brain implants. *International Journal Radiation Oncology Biology Physics* 18, 951–955.
- Mansfield, P. (1977). Multi-planar image formation using NMR spin echoes. *Journal of Physics C: Solid State Physics* 10, L55–L58.
- Maudsley, A.A., Simon, H.K., and Hilal, S.K. (1984). Magnetic field measurement by NMR imaging. *Journal of Physics E: Scientific Instrumentation* 17, 216–220.
- Maurer, C.R., Aboutanos, G.B., Dawant, B.M., Gadamsetty, S., Margolin, R.A., Maciunas, R.J., and Fitzpatrick, J.M. (1994). Effect of geometrical distortion correction in MR on image registration accuracy. In *Proceedings SPIE Vol 2167 Image processing*, pp. 200–213.
- Maurer, C.R. and Fitzpatrick, J.M. (1993). A review of medical image registration. In R.J. Maciunas (Ed.), *Interactive image-guided neurosurgery*, pp. 17–44. American Association of Neurological Surgeons, Park Ridge, IL.
- Mayr, N.A., Turgut Tali, E., Yuh, W.T.C., Brown, B.P., Chen Wen, B., Buller, R.E., Anderson, B., and Hussey, D.H. (1993). Cervical cancer: Application of MR imaging in radiation therapy. *Radiology* 189, 601–608.
- Meertens, H. (1989). *On line acquisition and analysis of portal images*. Ph. D. thesis, University of Amsterdam, The Netherlands.
- Michiels, J., Bosmans, H., Pelgrims, P., Vandermeulen, D., Gybels, J., Marchal, G., and Suetens, P. (1994). On the problem of geometric distortion in magnetic resonance images for stereotactic neurosurgery. *Magnetic Resonance Imaging* 12, 749–765.

- Mijnheer, B.J., Battermann, J.J., and Wambersie, A. (1987). What degree of accuracy is required and can be achieved in photon and neutron therapy? *Radiotherapy and Oncology* 8, 237–252.
- Mitchell, A.R. and Griffiths, D.F. (1980). *The finite difference method in partial differential equations*. New York, John Wiley & Sons Ltd.
- Moerland, M.A., Beersma, R., Bhagwandien, R., Wijrdeman, H.K., and Bakker, C.J.G. (1995). Analysis and correction of geometric distortions in 1.5 T magnetic resonance images for use in radiotherapy treatment planning. *Physics in Medicine and Biology* 40, 1651–1664.
- Mosher, T.J. and Smith, M.B. (1991). Magnetic susceptibility measurement using a double-dante tagging (DDT) sequence. *Magnetic Resonance in Medicine* 18, 251–255.
- Nath, R., Anderson, L.L., Luxton, G., Weaver, K.A., Williamson, J.F., and Meigooni, A.S. (1995). Dosimetry of interstitial brachytherapy sources: Recommendations of the AAPM radiation therapy committee task group no. 43. *Medical Physics* 22, 209–234.
- O'Donnell, M. and Edelstein, W.A. (1985). NMR imaging in the presence of magnetic field inhomogeneities and gradient field nonlinearities. *Medical Physics* 12, 20–26.
- Ogawa, S. and Lee, T.M. (1990). Magnetic resonance imaging of blood vessels at high fields: In vivo and in vitro measurements and image simulation. *Magnetic Resonance in Medicine* 16, 9–18.
- Ohara, K., Okumura, T., Akisada, M., Inada, T., Mori, T., Yokota, H., and Calaguas, M.J.B. (1989). Irradiation synchronized with respiration gate. *International Journal Radiation Oncology Biology Physics* 17, 853–857.
- Pelizzari, C.A., Chen, G.T.Y., Spelbring, D.R., Weichselbaum, R.R., and Chen, C.T. (1989). Accurate three-dimensional registration of CT, PET, and/or MR Images of the brain. *Journal of Computer Assisted Tomography* 13, 20–26.
- Podo, F. and Orr, J.S. (1992). *Tissue Characterization by Magnetic Resonance Spectroscopy and Imaging*. Istituto Superiore di Sanità, Rome.
- Posse, S. and Aue, W.P. (1990). Susceptibility artifacts in spin-echo and gradient-echo imaging. *Journal of Magnetic Resonance* 88, 473–492.
- Pötter, R., Heil, B., Schneider, L., Lenzen, H., Al-Dandashi, C., and Schnepfer, E. (1992). Sagittal and coronal planes from MRI for treatment planning in tumors of brain, head and neck: MRI assisted simulation. *Radiotherapy and Oncology* 23, 127–130.
- Rahmouni, A., Yang, A., Tempany, C.M.C., Frenkel, T., Epstein, J., Walsh, P., Leichner, P.K., Ricci, C., and Zerhouni, E. (1992). Accuracy of in-vivo assessment of prostatic volume by MRI and transrectal ultrasonography. *Journal of Computer Assisted Tomography* 16, 935–940.
- Riederer, S.J., Tasciyan, T., Farzaneh, F., Lee, J.N., Wright, R.C., and Herfkens, R.J. (1988). MR fluoroscopy: technical feasibility. *Magnetic Resonance in Medicine* 8, 1–15.
- Ritchie, C.J., Hsieh, J., Gard, M.F., Godwin, J.D., Kim, Y., and Crawford, C.R. (1994). Predictive respiratory gating: A new method to reduce motion artifacts on CT scans. *Radiology* 190, 847–852.

- Ross, C.S., Hussey, D.H., Pennington, E.C., Stanford, W., and Doornbos, J.F. (1990). Analysis of movement of intrathoracic neoplasms using ultrafast computerized tomography. *International Journal Radiation Oncology Biology Physics* 18, 671–677.
- Roy, J.N., Wallner, K.E., Harrington, P.J., Ling, C.C., and Anderson, L.L. (1993). A CT-based evaluation method for permanent implants: application to prostate. *International Journal Radiation Oncology Biology Physics* 26, 163–169.
- Runge, V.M., Clanton, J.A., Partain, C.L., and James, A.E. Jr. (1984). Respiratory gating in magnetic resonance imaging at 0.5 tesla. *Radiology* 151, 521–523.
- Schad, L.R., Blüml, S., Hawighorst, H., Wenz, F., and Lorenz, W.J. (1994). Radiosurgical treatment planning of brain metastases based on a fast, three-dimensional MR imaging technique. *Magnetic Resonance Imaging* 12, 811–819.
- Schad, L.R., Boesecke, R., Schlegel, W., Hartmann, G.H., Sturm, V., Strauss, L.G., and Lorenz, W.J. (1987b). Three dimensional image correlation of CT, MR, and PET studies in radiotherapy treatment planning of brain tumors. *Journal of Computer Assisted Tomography* 11, 948–954.
- Schad, L.R., Gademann, G., Knopp, M., Zabel, H.J., Schlegel, W., and Lorenz, W.J. (1992). Radiotherapy treatment planning of basal meningiomas: Improved tumor localization by correlation of CT and MR imaging data. *Radiotherapy and Oncology* 25, 56–62.
- Schad, L.R., Lott, S., Schmitt, F., Sturm, V., and Lorenz, W.J. (1987a). Correction of spatial distortion in MR Imaging: A prerequisite for accurate stereotaxy. *Journal of Computer Assisted Tomography* 11, 499–505.
- Schea, R.A., Schoepel, S.L., Lelancy, J.O., LaVigne, M.L., Ellis, J.H., and Roberts, J.A. (1990). Anatomic relationships during gynecologic intracavitary brachytherapy: CT, MRI and anatomic cross-sectional analysis. In *Proceedings 32nd Annual Meeting of the American Society for Therapeutic Radiology and Oncology (ASTRO)*, pp. 154.
- Schoepel, S.L., LaVigne, M.L., McShan, D.L., Fraass, B.A., and Roberts, J.A. (1990). Three-dimensional (3-D) treatment planning of intracavitary gynecologic implants: Analysis of ten cases and implications for dose specification. In *Proceedings 32nd annual meeting of the American Society for Therapeutic Radiology and Oncology*, pp. 129.
- Schupak, K., Malkin, M., Anderson, L., Arbit, E., Lindsley, K., and Leibel, S. (1995). The relationship between the technical accuracy of stereotactic interstitial implantation for high grade gliomas and the pattern of tumor recurrence. *International Journal Radiation Oncology Biology Physics* 32, 1167–1176.
- Sekihara, K., Kuroda, M., and Kohno, H. (1984). Image restoration from non-uniform magnetic field influence for direct Fourier NMR imaging. *Physics in Medicine and Biology* 29, 15–24.
- Shuman, W.P., Griffin, B.R., Haynor, D.R., Johnson, J.S., Jones, D.C., Cromwell, L.D., and Moss, A.A. (1985). MR Imaging in radiation therapy planning. *Radiology* 156, 143–147.
- Song, H.B., Cho, Z.H., and Hilal, S.K. (1982). Direct Fourier Transform NMR Tomography with Modified Kumar-Welti-Ernst (MKWE) Method. *IEEE Transactions on Nuclear Science NS-29*, 493–499.

- Stark, D.D. and Bradley, W.G. (1992). *Magnetic Resonance Imaging*. Mosby Year Book, Chicago.
- Suit, H.D. and Du Bois, W. (1991). The importance of optimal treatment planning in radiation therapy. *International Journal Radiation Oncology Biology Physics* 21, 1471–1478.
- Suit, H.D. and Miralbell, R. (1989). Potential impact of improvements in radiation therapy on quality of life and survival. *International Journal Radiation Oncology Biology Physics* 16, 891–895.
- Sumanaweera, T.S., Glover, G.H., Binford, T.O., and Adler, J.R. (1993). MR susceptibility misregistration correction. *IEEE Transactions on Medical Imaging* 12, 251–259.
- Sumanaweera, T.S., Glover, G.H., Song, S., Adler, J.R., and Napel, S. (1994). Quantifying MRI geometric distortion in tissue. *Magnetic Resonance in Medicine* 31, 40–47.
- Summers, R.M., Axel, L., and Israel, S. (1986). A computer simulation of nuclear magnetic resonance imaging. *Magnetic Resonance in Medicine* 3, 363–376.
- Suramo, I, Päävänsalo, M., and Myllylä, V. (1984). Cranio-caudal movements of the liver, pancreas and kidneys in respiration. *Acta Radiologica* 25, 129–131.
- TenHaken, R.K., Balter, J.M., Lam, K.L., and Robertson, J.M. (1994). Effects of patient breathing on CT-based 3D planning for lung irradiation. *Medical Physics* 21, 914.
- TenHaken, R.K., Thornton, A.F., Sandler, H.M., LaVigne, M.L., Quint, D.J., Fraass, B.A., Kessler, M.L., and McShan, D.L. (1992). A quantitative assessment of the addition of MRI to CT-based, 3-D treatment planning of brain tumors. *Radiotherapy and Oncology* 25, 121–133.
- Thornton, A.F., Sandler, H.M., TenHaken, R.K., McShan, D.L., Fraass, B.A., LaVigne, M.L., and Yanke, B.R. (1992). The clinical utility of magnetic resonance imaging in 3-dimensional treatment planning of brain neoplasms. *International Journal Radiation Oncology Biology Physics* 24, 767–775.
- Toonkel, L.M., Soila, K., Gilbert, D., and Sheldon, J. (1988). MRI assisted treatment planning for radiation therapy of the head and neck. *Magnetic Resonance Imaging* 6, 315–319.
- Van den Elsen, P.A. (1993). *Multimodality matching of brain images*. Ph. D. thesis, University of Utrecht, The Netherlands.
- Van den Elsen, P.A., Maintz, J.B.A., Pol, E.J.D., and Viergever, M.A. (1992). Image fusion using geometrical features. In *Proceedings SPIE Vol 1808 Visualization in biomedical computing*, pp. 172–186.
- Van den Elsen, P.A., Pol, E.J.D., and Viergever, M.A. (1993). Medical image matching - A review with classification. *IEEE Engineering in Medicine and Biology* 12, 26–39.
- Van den Elsen, P.A. and Viergever, M.A. (1994). Marker-guided multimodality matching of the brain. *European Radiology* 4, 45–51.
- Van der Koijk, J.F., Crezee, J., Van Leeuwen, G.M.J., Battermann, J.J., and Lagendijk, J.J.W. (1996). Dose uniformity in MECS interstitial hyperthermia: the impact of longitudinal control in model anatomies. *Physics in Medicine and Biology* 41 (3), 429–444.

- Van der Meulen, P., Groen, J.P., Tinus, A.M.C., and Bruntink, G. (1988). Fast Field Echo imaging: an overview and contrast calculations. *Magnetic Resonance Imaging* 6, 355–368.
- Van Ee, R. (1992). Analysis of susceptibility artifacts in magnetic resonance spin-echo imaging of simple objects. Master's thesis, University of Utrecht.
- Van Herk, M.B. and Kooy, H.M. (1994). Automatic three-dimensional correlation of CT-CT, CT-MRI, and CT-SPECT using chamfer matching. *Medical Physics* 21, 1163–1178.
- Van 't Riet, A., Te Loo, H.J., Ypma, A.F.G.V.M., Mak, A.C.A., Van Slooten, F.H.S., Hoekstra, C.J.M., and Stenfert Kroese, M.C. (1992). Ultrasonically guided transperineal seed implantation of the prostate: modification of the technique and qualitative assessment of implants. *International Journal Radiation Oncology Biology Physics* 24, 555–558.
- Van Tienhoven, G., Lanson, J.H., Crabeels, D., Heukelom, S., and Mijnheer, B. (1991). Accuracy in tangential breast treatment setup: A portal imaging study. *Radiotherapy and Oncology* 22, 317–322.
- Vijayakumar, S. and Chen, G.T.Y. (1995). Implementation of three dimensional conformal radiation therapy: prospects, opportunities, and challenges. *International Journal Radiation Oncology Biology Physics* 33, 979–983.
- Vijverberg, P.L.M., Blank, L.E.C.M., Dabhoiwala, N.F., Reijke, Th.M. de, Koedooder, C., Hart, A.A.M., Kurth, K.H., and Gonzalez Gonzalez, D. (1993). Analysis of biopsy findings and implant quality following ultrasonically-guided ^{125}I implantation for localised prostatic carcinoma. *British Journal of Urology* 72, 470–477.
- Warszawski, N., Pfreunder, L., Bohndorf, W., Bratengeier, K., and Krone, A. (1992). Interstitial brachytherapy with flexible catheters in brain tumours. *Activity International Selectron Brachytherapy Journal* 6, 28–31.
- Weast, R.C. and Astle, M.J. (1980). *CRC Handbook of Chemistry and Physics*. CRC Press, Florida.
- Weaver, K., Smith, V., Lewis, J.D., Lulu, B., Barnett, C.M., Leibel, S.A., Gutin, P., Larson, D., and Phillips, T. (1990). A CT-based computerized treatment planning system for I-125 stereotactic brain implants. *International Journal Radiation Oncology Biology Physics* 18, 445–454.
- Weisskoff, R.M. and Kiihne, S. (1992). MRI Susceptometry: Image-based measurement of absolute susceptibility of MR contrast agents and human blood. *Magnetic Resonance in Medicine* 24, 375–383.
- Whitmore Jr., W.F., Hilaris, B., and Grabstald, H. (1972). Retropubic implantation of Iodine-125 in the treatment of prostatic cancer. *Journal of Urology* 108, 918–920.
- Willcott III, M.R., Mee, G.L., and Chesick, J.P. (1987). Magnetic field mapping in NMR Imaging. *Magnetic Resonance Imaging* 5, 301–306.
- Willett, C.W., Linggood, R.M., Stracher, M.A., Goitein, M., Doppke, K., Kushner, D.C., Morris, T., Pardy, J., and Carroll, R. (1987). The effect of respiratory cycle on mediastinal and lung dimensions in Hodgkin's disease. *Cancer* 60, 1232–1237.
- Wisner, G.L., Rosen, B.R., Buxton, R., Stark, D.D., and Brady, T.J. (1985). Chemical shift imaging of bone marrow. *American Journal of Roentgenology* 145, 1031–1037.

- Yamada, N., Imakita, S., Nishimura, T., Takamiya, M., and Naito, H. (1992). Evaluation of susceptibility effects on gradient echo phase images in vivo: A sequential study of intracerebral hematoma. *Magnetic Resonance Imaging* 10, 559–571.
- Yamada, N., Imakita, S., Sakuma, T., Nishimura, Y., Yamada, Y., Naito, H., Nishimura, T., and Takamiya, M. (1990). Evaluation of susceptibility effects on the phase images of a simple gradient echo. *Radiology* 175, 561–565.
- Yanke, B.R., TenHaken, R.K., Aisen, A., Fraass, B.A., and Thornton Jr., A.F. (1991). Design of MRI scan protocols for use in 3-D, CT-based treatment planning. *Medical Dosimetry* 16, 205–211.
- Young, I.R., Bydder, G.M., Khenia, S., and Collins, A.G. (1989). Assessment of phase and amplitude effects due to susceptibility variations in MR Imaging of the brain. *Journal of Computer Assisted Tomography* 13, 490–494.
- Young, I.R., Cox, I.J., Bryant, D.J., and Bydder, G.M. (1988). The benefits of increasing spatial resolution as a means of reducing artifacts due to field inhomogeneities. *Magnetic Resonance Imaging* 6, 585–590.
- Young, I.R., Khenia, S., Thomas, D.G.T., Davis, C.H., Gadian, D.G., Cox, I.J., Ross, B.D., and Bydder, G.M. (1987). Clinical magnetic susceptibility mapping of the brain. *Journal of Computer Assisted Tomography* 11, 2–6.

List of publications

C.J.G. Bakker and M.A. Moerland. Simple formulae for the calculation of ρ , T_1 and T_2 from a properly designed diagnostic NMR experiment. *Magnetic Resonance Imaging*, 7:305–307, 1989.

C.J.G. Bakker, R. Beersma, M.A. Moerland, and R. Bhagwandien. Analysis and correction of object-induced and system-dependent geometrical distortion in MR imaging. In *Proceedings Eleventh annual meeting of the society for Magnetic Resonance in Medicine (SMRM)*, page 4244, 1992.

C.J.G. Bakker, M.A. Moerland, R. Bhagwandien, and R. Beersma. Analysis of machine-dependent and object-induced geometric distortions in 2DFT MR imaging. *Magnetic Resonance Imaging*, 10:597–608, 1992.

C.J.G. Bakker, R. Bhagwandien, and M.A. Moerland. 3D Analysis of susceptibility artifacts in SE and GE magnetic resonance imaging. In *Proceedings Twelfth annual meeting of the society for Magnetic Resonance in Medicine (SMRM)*, page 746, 1993.

C.J.G. Bakker, R. Bhagwandien, M.A. Moerland, and M. Fuderer. Susceptibility artifacts in 2DFT spin-echo and gradient-echo imaging: The cylinder model revisited. *Magnetic Resonance Imaging*, 11:539–548, 1993.

C.J.G. Bakker, R. Bhagwandien, M.A. Moerland, and L. Ramos. 3D Analysis of the susceptibility artifacts in MRI. In *Proceedings Tenth annual meeting of the European Society for Magnetic Resonance in Medicine and Biology (ESMRMB)*, page 426, 1993.

C.J.G. Bakker, R. Bhagwandien, M.A. Moerland, and L. Ramos. Theoretical analysis of susceptibility artifacts in MRI. In *Proceedings Eight European Congress of Radiology (ECR)*, page 274, 1993.

C.J.G. Bakker, R. Bhagwandien, and M.A. Moerland. Simulation of susceptibility artifacts in 2D and 3D Fourier Transform spin-echo and gradient-echo magnetic resonance imaging. *Magnetic Resonance Imaging*, 12:767-774, 1994.

C.J.G. Bakker, R. Bhagwandien, M.A. Moerland, and L.M.P. Ramos. Parameters affecting the appearance of susceptibility artifacts in MR imaging. In *Proceedings Tenth European Congress of Radiology (ECR)*, page S399, 1995.

R. Bhagwandien, H.K. Wijrdeman, M.A. Moerland, M.A.A.M. Heesters, J.J.W. Lagendijk, and C.J.G. Bakker. Relaxation times T_1 and T_2 in cervical and rectal carcinoma before and after RT treatment. In *Proceedings Eight annual meeting of the society for Magnetic Resonance in Medicine (SMRM)*, page 697, 1989.

R. Bhagwandien, C.J.G. Bakker, R. Beersma, M.A. Moerland, and J.J.W. Lagendijk. Numerical analysis of the magnetic field for arbitrary magnetic susceptibility distributions. In *Klinische Fysica N4*, pages 189–190, 1991.

R. Bhagwandien, C.J.G. Bakker, M.A. Moerland, and J.J.W. Lagendijk. Numerical analysis of the magnetic field for arbitrary magnetic permeability distributions. In *Proceedings Ninth Annual meeting of the Society for Magnetic Resonance Imaging (SMRI)*, page 307, 1991.

R. Bhagwandien, C.J.G. Bakker, R. van Ee, M.A. Moerland, and J.J.W. Lagendijk. Numerical analysis of

the magnetic field for arbitrary magnetic susceptibility distributions. In *Proceedings Eight annual meeting of the European Society for Magnetic Resonance in Medicine and Biology (ESMRMB)*, page 250, 1991.

R. Bhagwandien, R. van Ee, R. Beersma, C.J.G. Bakker, M.A. Moerland, and J.J.W. Lagendijk. Numerical analysis of the magnetic field for arbitrary magnetic susceptibility distributions in 2D. *Magnetic Resonance Imaging*, 10:299–313, 1992.

R. Bhagwandien, M.A. Moerland, C.J.G. Bakker, R. Beersma, and J.J.W. Lagendijk. Analysis and correction of geometric distortions in MRI. In *Klinische Fysica N4*, page 197, 1992.

R. Bhagwandien, M.A. Moerland, C.J.G. Bakker, R. Beersma, and J.J.W. Lagendijk. Analysis of patient induced marker shifts in MRI. In *Proceedings Eleventh annual meeting of the society for Magnetic Resonance in Medicine (SMRM)*, page 4305, 1992.

R. Bhagwandien, M.A. Moerland, C.J.G. Bakker, R. Beersma, and J.J.W. Lagendijk. 3D Analysis of the magnetic field for arbitrary magnetic susceptibility distributions. In *Proceedings Twelfth annual meeting of the society for Magnetic Resonance in Medicine (SMRM)*, page 349, 1993.

R. Bhagwandien, M.A. Moerland, C.J.G. Bakker, R. Beersma, and J.J.W. Lagendijk. Numerical analysis of the magnetic field for arbitrary magnetic susceptibility distributions in 3D. In *Proceedings Tenth annual meeting of the European Society for Magnetic Resonance in Medicine and Biology (ESMRMB)*, page 89, 1993.

R. Bhagwandien, M.A. Moerland, L. Ramos, and C.J.G. Bakker. 3D Analysis of the susceptibility artifacts in MRI. In *Proceedings International conference on Volume Image Processing (VIP)*, pages 93–94, 1993.

R. Bhagwandien, M.A. Moerland, C.J.G. Bakker, R. Beersma, and J.J.W. Lagendijk. Numerical analysis of the magnetic field for arbitrary magnetic susceptibility distributions in 3D. *Magnetic Resonance Imaging*, 12:101–107, 1994.

R.A.F.M. Chamuleau, J.H.N. Creyghton, I. de Nie, M.A. Moerland, O.R. van der Lende, and J. Smidt. Is the magnetic resonance imaging proton spin-lattice relaxation time a reliable noninvasive parameter of developing liver fibrosis? *Hepatology*, 8:217–221, 1988.

M.A.A.M. Heesters, H.K. Wijrdeman, H. Struikmans, T. Witkamp, and M.A. Moerland. Brain tumor delineation based on CT and MR imaging. Implications for radiotherapy treatment planning. *Strahlentherapie und Onkologie*, 12:729–733, 1993.

M.A. Moerland, C.J.G. Bakker, C.N. de Graaf. Concerning the derivation and representation of parameter images in NMR imaging. In *C.N. de Graaf, M.A. Viergever (eds), Information Processing in Medical Imaging, New York*, pages 483–497, 1988.

M.A. Moerland, H.K. Wijrdeman, M.A.A.M. Heesters, C.J.G. Bakker. Applications of NMR in radiotherapy: a view from the University Hospital Utrecht. *Magnetic Resonance in Medicine and Biology*, 1:203–213, 1988.

M.A. Moerland and C.J.G. Bakker. Non-linear display of NMR T_1 and T_2 images taking into account precision and visual perception. *Magnetic Resonance Imaging*, 7:405–410, 1989.

M.A. Moerland, H.K. Wijrdeman, R. Bhagwandien, M.A.A.M. Heesters, J.J.W. Lagendijk, and C.J.G. Bakker. Radiation induced changes of tumor volume, T_1 and T_2 in cervical and rectal carcinoma. In *Proceedings International Symposium Tissue characterization in MR-images, Wiesbaden*, page 97, 1989.

M.A. Moerland, R. Bhagwandien, H.K. Wijrdeman, and C.J.G. Bakker. Variability of ^1H NMR Relaxation times in cervix and rectal carcinoma. In *Proceedings Seventh annual meeting of the European Society for Magnetic Resonance in Medicine and Biology (ESMRMB)*, page 392, 1990.

M.A. Moerland, R. Bhagwandien, R. Beersma, and C.J.G. Bakker. Determination of geometric distortion

in MR imaging; Implications for Radiotherapy Treatment Planning. In *Proceedings of European Society for Therapeutic Radiology and Oncology (ESTRO)*, page 25, 1991.

M.A. Moerland, R. Bhagwandien, and C.J.G. Bakker. Recognition of susceptibility induced geometric distortions in MR imaging; implications for the use of markers in radiotherapy treatment planning. In *Proceedings Tenth Annual Meeting of the Society for Magnetic Resonance Imaging (SMRI)*, page 407, 1992.

M.A. Moerland, R. Bhagwandien, R. Beersma, and C.J.G. Bakker. Geometrische betrouwbaarheid van Magnetic Resonance Imaging; implicaties voor MRI-geïntegreerde radiotherapie planning. *Klinische Fysica N1*, pages 44–48, 1992.

M.A. Moerland, J.H.A.G. de Koning, and J.J. Battermann. The anisotropic dose distribution of a HDR Iridium-192 source. In *Proceedings Seventh International Brachytherapy Working Conference*, pages 286–289, 1992.

M.A. Moerland, R. Beersma, R. Bhagwandien, and C.J.G. Bakker. Matching of magnetic resonance images and simulator films for localization of lateral boost fields in patients with high grade astrocytomas. In *Proceedings International conference on Volume Image Processing (VIP)*, pages 133–136, 1993.

M.A. Moerland, R. Beersma, R. Bhagwandien, H.K. Wijrdeman, and C.J.G. Bakker. Geometric accuracy of MRI based radiotherapy treatment of brain tumors. In *Proceedings Eight European Congress of Radiology (ECR)*, page 387, 1993.

M.A. Moerland, R. Beersma, R. Bhagwandien, H.K. Wijrdeman, and C.J.G. Bakker. Matching of magnetic resonance images and simulator films for radiotherapy treatment planning of high grade astrocytomas. In *Proceedings Tenth annual meeting of the European Society for Magnetic Resonance in Medicine and Biology (ESMRMB)*, page 37, 1993.

M.A. Moerland, R. Bhagwandien, R. Beersma, and C.J.G. Bakker. Long term stability of the static and gradient fields of a commercial MR scanner. In *Proceedings Tenth annual meeting of the European Society for Magnetic Resonance in Medicine and Biology (ESMRMB)*, page 431, 1993.

M.A. Moerland, A.C.M. van den Bergh, R. Bhagwandien, W.M. Janssen, C.J.G. Bakker, J.J.W. Lagendijk, and J.J. Battermann. The influence of respiration induced motion of the kidneys on the accuracy of radiotherapy treatment planning, a magnetic resonance imaging study. *Radiotherapy and Oncology*, 30:150–154, 1994.

M.A. Moerland, R. Beersma, R. Bhagwandien, H.K. Wijrdeman, and C.J.G. Bakker. Analysis and correction of geometric distortions in 1.5 T magnetic resonance images for use in radiotherapy treatment planning. *Physics in Medicine and Biology*, 40:1651–1664, 1995.

M.A. Moerland, R. Beersma, R. Bhagwandien, H.K. Wijrdeman, and C.J.G. Bakker. Analysis of object-related spatial distortions in 1.5 T magnetic resonance head images. *British Journal of Radiology*, in press.

M.A. Moerland, R. Beersma, R. Bhagwandien, H.K. Wijrdeman, and C.J.G. Bakker. Analysis and correction of geometric distortions in 1.5 T magnetic resonance head images. In *Proceedings 19th Gray Conference*, page 24, 1995.

M.A. Moerland, R. Beersma, R. Bhagwandien, H.K. Wijrdeman, and J.J. Battermann. Evaluation of permanent I-125 implants using radiographs and MRI. In *Proceedings Third Biennial ESTRO meeting on Physics in Clinical Radiotherapy*, page S12, 1995.

M.A. Moerland, H.K. Wijrdeman, R. Beersma, C.J.G. Bakker, and J.J. Battermann. MRI-based evaluation of permanent I-125 prostate implants. In *Proceedings International Brachytherapy Meeting GEC/ESTRO-ABS-GLAC*, page S1, 1996.

P.E. Syens, H.K. Wijrdeman, M.A. Moerland, C.J.G. Bakker, J.W.A.H. Vermeulen, and P.R. Luyten. Human breast cancer in vivo: H-1 and P-31 MR Spectroscopy at 1.5 T. *Radiology*, 169:615–620, 1988.

Dankwoord

Bij wetenschappelijk onderzoek, en zeker bij klinisch-wetenschappelijk onderzoek zijn vele mensen betrokken. Langs deze weg wil ik allen, die een bijdrage hebben geleverd aan het tot stand komen van dit proefschrift, hartelijk danken.

Prof. Battermann wil ik bedanken voor de geboden gelegenheid om wetenschappelijk onderzoek te verrichten op de afdeling Radiotherapie. Vooral de prostaatimplantaties hebben ons beider interesse en zullen ook in de naaste toekomst nog onderwerp van onderzoek zijn.

Jan Lagendijk en Chris Bakker wil ik bedanken voor de inspirerende begeleiding, waarbij de combinatie van wetenschappelijk enthousiasme en relativerend vermogen mij op de been hebben gehouden bij het doen van dit onderzoek.

Ramesh Bhagwandien wil ik bedanken voor de bijdrage met betrekking tot de magneetveldberekeningen en voor de hulp bij de lay-out van dit proefschrift, maar bovenal voor de prettige samenwerking.

Zo ook wil ik graag Rob Beersma bedanken, die als projectmedewerker veel computerprogramma's voor dit onderzoek heeft geschreven en bovendien ook zijn steentje heeft bijgedragen aan de evaluatie van de prostaatimplantaties.

Ook alle andere projectmedewerkers bedankt, bijvoorbeeld voor het wegwijs maken in de meest efficiënte tekstverwerkers en andere applicaties op de SiliconGraphics workstations. Mede dankzij Ric Exterkate vormen we een hecht netwerk.

Ook Herman van Kleffens en Hans Welleweerd en de fysisch assistenten en versnellertechnici ben ik veel dank verschuldigd. Dankzij jullie inzet kon ik tijd vinden voor de afronding van dit proefschrift.

Zonder de inbreng van de klinische collega's was dit onderzoek niet mogelijk geweest. Naast Mart Heesters en Fons van den Bergh wil ik vooral Harm Wijrdeman bedanken. Harm, vele uren hebben we op het NMR instituut doorgebracht om onderzoek te doen bij patiënten, waarna je ook nog eens gevraagd werd cervix-, rectum- of prostaattumoren in te tekenen, daarbij steeds wakend over de "clinical relevance".

Met betrekking tot het onderzoek bij de patiënten wil ik ook graag de afdeling Radiodiagnostiek (Prof. Mali, Theo Witkamp, en collega's) en de radiodiagnostisch laboranten van het NMR instituut bedanken. Vooral de sessies met Gerrit waren onvergetelijk. Ook de hulp van Wim Jansen bij technische moeilijkheden werd zeer gewaardeerd.

De radiotherapeutisch laboranten wil ik graag bedanken voor het maken van de röntgenfoto's op de lokalisator (Agnes en collega's), voor hun bijdrage aan de evaluatie van de prostaatimplantaties (Marijke, André, Wilfred en collega's) en voor de hulp op het gebied van de dosisberekening, bijvoorbeeld bij het onderzoek naar de invloed van de beweging van de nieren op de dosisverdeling (Frans en collega's).

Dank ben ik ook verschuldigd aan Bert Cramer, die ondanks zijn altijd lange activiteitenlijst, binnen de kortste keren zeer bruikbare prototype fantomen en hulpstukken wist te fabriceren. Ook dank aan de Instrumentele Dienst voor het vervaardigen van de buisjesfantomen.

Iris Gademan en Derk Rutgers wil ik bedanken voor de hulp bij het bereiden van diverse

oplossingen en substanties in hun lab en voor de discussies op het gebied van NMR en radiobiologie.

Liesbeth van Doodewaard en Joke van Randwijk, bedankt voor de secretariële ondersteuning.

Mijn dank gaat ook uit naar Jan de Groot en collega's voor het vele fotografische werk voor congressen en publicaties.

En natuurlijk ben ik ook de vele patiënten en proefpersonen dankbaar die mee wilden doen aan de verschillende onderzoeken.

Verder wil ik iedereen op de afdeling Radiotherapie bedanken voor de tien jaren die ik er nu al weer met veel plezier werk.

Tot slot wil ik graag Rianne bedanken voor de steun op velerlei gebied, voor zover het mijn werk betreft vooral sinds de aanvang van mijn studie aan de TH Delft. Het zou overdreven zijn om de kinderen Maaïke, Joline en Merijn bijdragen aan dit proefschrift toe te schrijven, maar ik heb wel heel veel plezier met ze.

Curriculum Vitae

Rien Moerland is geboren op 17 juli 1957 te Stavenisse. In 1975 werd het Atheneum-B diploma behaald aan de Rijksscholengemeenschap te Bergen op Zoom. Daarna volgde hij achtereenvolgens de opleidingen tot radiodiagnostisch en radiotherapeutisch laborant in het Academisch Ziekenhuis Rotterdam-Dijkzigt en in de Daniël den Hoed Kliniek. In 1980 begon hij met de studie Technische Natuurkunde aan de toenmalige Technische Hogeschool Delft en behaalde het kandidaatsexamen in november 1983 en het doctoraalexamen in mei 1986. Het vierde- en vijfdejaarslaboratoriumwerk bij de vakgroep Magnetische Resonantie/Lage Temperaturen o.l.v. Prof. dr ir J. Smidt betrof “Enige aspecten van T_1 - en T_2 -metingen aan proefdieren met behulp van magnetic resonance imaging” en “Onderzoek aan fasefouten bij MRI en behandeling van verschillende MRI stromingsmeetmethoden” en werd begeleid door ir J.H.N. Creighton.

Vanaf september 1986 werkt hij op de afdeling Radiotherapie van het Academisch Ziekenhuis Utrecht o.l.v. Prof. dr J.J. Battermann, eerst als toegevoegd onderzoeker op het project “NMR imaging as an aid in radiotherapy and hyperthermic treatment” (UUKC 86-24), vanaf mei 1988 als klinisch fysicus in opleiding en vanaf november 1990 als klinisch fysicus radiotherapie. Vanaf januari 1990 was hij tevens begeleider van het project “MRI in radiotherapy planning” (IKMN 90-04), gefinancierd door de Nederlandse Kankerbestrijding. Het laatstgenoemde project vormde de basis voor dit proefschrift.